High Gain Broadband mm-wave Antennas and Beamforming for Wireless Communication Systems

Essa Mujammami

A Thesis

In the Department

of

Electrical and Computer Engineering

Presented in Partial Fulfillment of the Requirements

for the Degree of

Doctor of Philosophy in (Electrical and Computer Engineering) at

Concordia University

Montreal, Quebec, Canada

September 2019

© Essa Mujammami, 2019

CONCORDIA UNIVERSITY

SCHOOL OF GRADUATE STUDIES

This is to certify that the thesis prepared

By: Essa Mujammami

Entitled: High Gain Broadband mm-wave Antennas and Beamforming for Wireless Communication Systems

and submitted in partial fulfillment of the requirements for the degree of

Doctor of Philosophy (Electrical and Computer Engineering)

complies with the regulations of the University and meets the accepted standards with respect to originality and quality.

Signed by the final examining committee:

_____Chair
Dr. Mehdi Hojjati

_____ External Examiner
Dr. Mustapha C.E. Yagoub

_____ External to Program
Dr. Amr Youssef

_____ Examiner
Dr. Tayeb Denidni

_____ Examiner
Dr. Robert Paknys

_____Thesis Supervisor
Dr. Abdel R. Sebak

Approved by _____
Dr. Rastko Selmic, Graduate Program Director

November 12, 2019

_____
Dr. Amir Asif, Dean
Gina Cody School of Engineering & Computer Science

Abstract

High Gain Broadband mm-wave Antennas and Beamforming for Wireless Communication Systems

Essa Mujammami, Ph.D.
Concordia University, 2019

Generating multi-beams along with having broadband and beam steering capability in the mm-waves band are of crucial importance for diverse applications such as remote piloted vehicles, satellites, collision-avoidance radars, and ultra-wideband communications systems. Besides, the propagation environment at millimeter wave (mm-wave) frequencies—suggested for the next generation of wireless networks (5G)—lends itself to a beamforming structure wherein antenna arrays are required in order to obtain the necessary link budget and to overcome the associated strong attenuation. Therefore, the design of high gain antennas (to focus the directive beam to a user) and beamforming networks (to reduce interference) are essential and are needed to address many challenges associated with 5G wireless communications.

This work addresses the design and development of high-performance Quasi-Yagi antenna and Rotman lens-based beamforming networks. Accordingly, several issues are addressed in this thesis.

A Quasi-Yagi antenna with a perturbed dielectric lens that is broadband and has high gain is designed, optimized, fabricated and tested at 30 GHz. The antenna provides 95% aperture efficiency with a measured gain of 15 dBi as well as a radiation efficiency of ~90% at 30 GHz and a broadband (24-40 GHz) for $|S_{11}| < -10\ dB$. The designed end-fire antenna, with its low-profile and compact size, is a good candidate for many applications in the mm-wave band.

An optimum and accurate methodology for designing Rotman lens-based mm-wave analog beamforming network (BFN) is presented. The simulation and measurement results showed good beamforming capabilities as well as a scanning range of 80° in the azimuth plane, and, also, good matching at the array ports. The maximum phase error is ±6.6°, and the main beam of the proposed BFN points at seven different angular directions that cover the range of ±40°. The maximum achieved realized gain is 14 dBi at 28 GHz for the center beam.

An analog Rotman lens-based BFN using RWG technology, integrated with the excitation ports and the antenna array elements, was designed, simulated, manufactured, and measured. The proposed integrated system is realized using the metallized 3D-printing technology, in order to reduce the implementation cost of the full metal RGW Rotman lens. The measured results demonstrate that the system scan range equals ±39.5º over a wideband 27.5-37 GHz decreases to 30º in the band 37-40 GHz. The BFN bandwidth for VSWR < 2 is larger than 38% and is limited by its single antenna element.

Acknowledgements

All my thanks to ALLAH, for the successful completion of this work.

I would like to express my deepest gratitude and thanks to Prof. A.R. Sebak for his continuous supervision and generous support. Prof. Sebak is behind all analytical, technical and even spiritual actions throughout this work. Without his encouragement, the thesis could not reach this level.

Besides my advisor, I would like to thank Dr. Tayeb Denidni, Dr. Robert Paknys, Dr. Amr Youssef and Dr. Mustapha C.E. Yagoub for their priceless comments and serving in my examining committee.

I would like to express the deepest appreciation to all of my colleagues in the microwave group for their help, support, emotions and encouragement, especially, Islam Afifi and Shraman Gupta.

I would like also, to offer my special thanks for my father, brothers, and my sisters, for their great hearts which looked after me all these years.

Last but not least many thanks to my Great family, who always encourage me for further progress. May ALLAH the Almighty bless you all and guides you to the happiness in this life and Hereafter.

Table of Contents

List of Abbreviations

3DP-RGW	Three dimensions Printed Ridge gap waveguide
3G	Third generation
3GPP	The 3rd Generation Partnership Project
4G	Fourth generation
5G	Fifth Generation
BFN	Beamforming network
BiCMOS	Bipolar complementary metal oxide semiconductor
BW	Beam width
CMOS	Complementary metal oxide semiconductor
CPW	Co-Planar Waveguide
CST-MWS	Computer Simulation Technology Microwave Studio
DLA	Dielectric lens antenna
DRA	Dielectric resonator antennas
DSW	Dielectric slab waveguide
FBW	Fractional bandwidth
FCC	The Federal Communications Commission
HFSS	High Frequency Structure Simulator
HOM	Higher order mode
IEEE	Institute of Electrical and Electronics Engineers
ITU-R	Radio sector of International telecommunication union
LOS	Line-of-sight
NLOS	Non-line-of-sight
LPDA	Log Periodic Antenna
LTCC	Low-temperature co-fired ceramics
LTE	Long Term Evolution
MEMS	Microelectromechanical systems
MIMO	multiple-input multiple-output
MMIC	Millimeter-wave monolithic integrated circuit

mmwave	Millimeter wave
MS	Microstrip
PCB	Printed circuit board
PLDC	Parallel lines dielectric corrugation
PRGW	Printed Ridge gap waveguide
RCDL	Ray combiner dielectric lens
RF	Radio Frequency
RFIC	Radio Frequency Integrated Circuit
RGW	Ridge gap waveguide
RTSS	Real-time spectrum-sniffer
Rx	Receiver
SIDRA	Substrate integrated DRA
SIW	Substrate integrated waveguide
TTD	True-time-delay
Tx	Transmitter

List of Tables

List of Figures

CHAPTER 1: Introduction

1.1 Historical Overview

With end users ranging from enterprise-level data centers to single consumers with smartphones demanding higher data rate, newer technologies are needed more than ever before. In essence, the traffic from wireless and mobile devices is expected to increase as global monthly exabytes reach an estimated 77.5 by 2022 [1]. Currently, the allocated spectrum for service providers is fragmented into disjoint frequency bands, which have different radio networks and different propagation characteristics for each network. This situation has led to base station designs to serve many different bands with different cell sites, and each site has multiple base stations for each frequency or technology usage (e.g., 3G, 4G, and Long-Term Evolution-Advanced [LTE-A]). Consequently, this further limits the ability to deliver upon the demanded high quality, low latency video and multimedia applications such as virtual reality and augmented reality applications, which need real-time response with this disjoint frequency bands wireless networks [2].

This demand has thus motivated the exploration of the underutilized millimeter wave (mmwave) frequency spectrum for future broadband wireless networks. Essentially, mmwave frequency spectrum was explored by Jagadish Chandra Bose, who, 100 years ago, developed the oldest milestone achievement as well as the first mm-wave communication system. Over a 23-meter distance, Bose demonstrated transmission and reception through two intervening walls in Presidency College, Calcutta, India. This was achieved by using 60 GHz electromagnetic waves, remotely ringing a bell, and detonating some gunpowder. The entirety of the mm-wave components—such as a spark transmitter, coherer, dielectric lens, polarizer, horn antenna, and cylindrical diffraction grating—have been all developed by Bose [3]. The frequency band of mmwave covers the frequency spectrum from 30 GHz to 300 GHz. Conventionally, the mm-wave band has been largely ignored for wireless networks due to some concerns about mm-wave propagation characteristics, which is related to higher atmospheric and attenuation losses, penetration losses, and increased absorption and scattering in rainy conditions. Nonetheless, only a specific part of the spectrum is suitable for wireless transmission. This is attributed to the atmospheric absorption being small in the so-called atmospheric windows. The mm-wave atmospheric windows are centered at 35, 90, 140, and 220 GHz [4].

Recent measurements revealed a good outdoor short-range coverage when using directive antenna beams—that is, even when radio LOS is not met particularly at 28 GHz and 38 GHz. *Figure 1.1* shows the rain attenuation and atmospheric absorption characteristics of mm-wave propagation. For heavy rainfall rates of one inch/hr for cellular propagation at 28 GHz, only 7 dB/km of attenuation is expected. Therefore, within cell sizes on the order of 200 m, only 1.4 dB. Similarly, the atmospheric absorption does not create significant additional path loss for mmwave, particularly at 28 GHz and 38 GHz. This relates to mm-wave signals experiencing low diffraction as a result of their small wavelength, where line of sight (LOS) signals propagate in conditions similar to free space (a path loss exponent of two, on average). On the other hand, non-line of sight (NLOS) signals experience more significant losses and, hence, a path loss exponent of 5.76, on average. However, the NLOS path loss exponent is significantly reduced when directing the transmitter (Tx) and the receiver (Rx) antenna beams toward each other in order to overcome the increased path loss at mmwave [2].

1.2 Fifth Generation of Wireless Networks

Fifth generation (5G) of wireless networks is the future wireless network technology. It delivers more reliable services via ultra-dense radio networking with self-backhauling, mesh-like connectivity, lower outage probability, much higher bit rates in a large portion of the coverage area, lower infrastructure cost, and more efficient spectrum reuse. Recently, research has been conducted to examine the feasibility of utilizing mm-waves band for 5G wireless network technology as a solution for disjoint frequency bands in the current wireless networks. The conducted studies provide vital information for design and operation. Moreover, some telecommunication standardization organizations have entirely specified the overall 5G system. The Federal Communications Commission (FCC) in the USA has allocated spectrum in the 24–47 GHz mm-wave ranges for high-band terrestrial use [5].

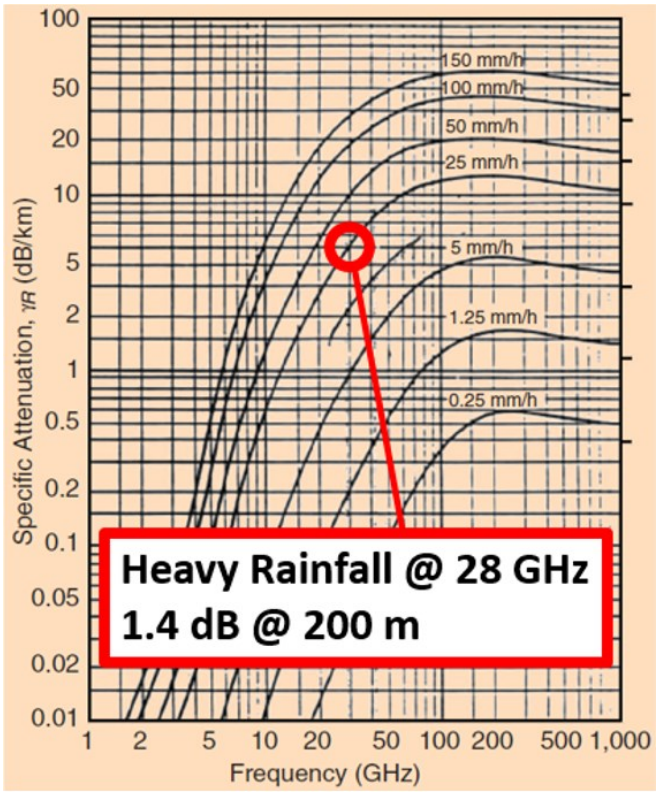

(a)

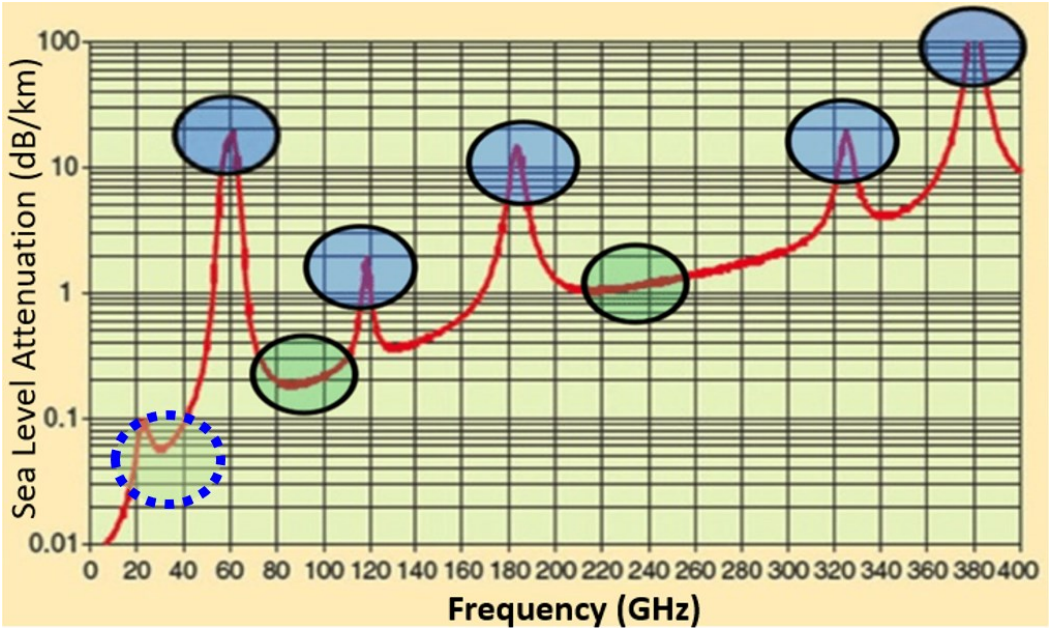

(b)

Figure 1.1: mm-wave propagation characteristics: (a) The rain attenuation. (b) Atmospheric absorption [2].

Similarly, the 3rd Generation Partnership Project (3GPP) has now specified the overall 5G system architecture—that is, specifying features, functionality, and services. Essentially, 3GPP has studied and recommended two frequency ranges: frequency range 1 (FR1), which covers 0.41–7.125 GHz, and frequency range 2 (FR2), which covers 24.25–52.6 GHz for 5G [6]. These movements toward the new generation of wireless networks make deployment of the first 5G wireless network feasible in early 2020.

1.3 Motivations

Millimeter waves open up more spectrum allocations for the 5G wireless networks, which could integrate and enable the full potential of mobile technology, big data, IoT, and cloud computing as well as supporting digital transformation across various sectors, including healthcare, smart vehicles, smart home, and industrial automation. These new devices have multi antennas in a small area, so a compact size antenna is required. Therefore, moving to mm-wave frequency band results in a small antenna size that allows fitting multi-antennas in a compact device. Moreover, advanced antenna and beamforming networks can greatly improve the performance of mm-wave wireless networks by providing a good link quality and high signal-to-noise ratio. Besides, generating multi-beams along with having broadband and beam steering capability in mm-waves band are of crucial importance for diverse applications such as remote piloted vehicles, satellites, collision-avoidance radars, and ultra-wideband communications systems.

Rotman lens has been widely used in many microwave beamforming applications, and recently in mmwave with focus mainly on the phase error performance, while a few number of publications focus on the amplitude performance. Moreover, there is a lack of publications on Rotman lens-based beamforming network implemented with the RGW in its original metal form, printed (PRGW), or metallized 3D-Printing (3DP-RGW). Only a few number of publications are found in the open literature, even with simulation results only without experimental verification.

For these reasons, this thesis deals with developing high gain, wideband antennas and beamforming networks. The proposed work addresses both the amplitude and the phase error while, at the same time, determining the design parameters of the proposed Rotman lens-based beamforming network implemented with MS and with RGW technologies.

1.4 Problem Statement

mm-wave band is a promising frequency band that provides more spectrum for the future wireless communication networks. However, its propagation nature suffers from atmospheric absorption and attenuation losses. Furthermore, mmwaves cannot penetrate concrete and other obstacles. Therefore, high gain antennas are required in order to compensate for path losses. Additionally, sophisticated beamforming networks are needed to direct the beam in a certain angular direction to have point-to-point communication. Thus, leading to a high improvement in the link quality and the immunity to interference.

Antennas in general are designed and fabricated with different technologies, geometries, and performance; Quasi-Yagi antenna is thus considered for its advantages of low profile, light-weight, ease of fabrication and installation, and high radiation efficiency. This has led to a marked attraction in its use in microwave and mm-wave applications. The bandwidth of conventional Quasi-Yagi antenna is narrow and cannot provide the high gain owned by Yagi-Uda antenna. Thus, in order to overcome this limitation, various methods are proposed in literature and, now, very good bandwidth and gain are achieved. Nevertheless, the gain improvement comes at the expense of a relatively large size or instability over frequency. Therefore, for the purpose of gain enhancement, dielectric lenses are widely used. Even though the dielectric lens antenna (DLA) gains are high, they are mostly designed with thick substrates or bulky structures [7,C1].

There are many well-known examples of analog beamforming networks such as the Rotman lens, the Butler matrix, the Blass matrix, and the Nolen matrix. The Butler matrix is simple and easy to realize. However, it has limitations due to phase shifter and crossover designs, that leads to a low achievable gain, and a low scanning plane. All these issues make it hard to be utilized for actual 5G applications. Similarly, the Blass matrix design and the Nolen matrix design involve many couplers and phase shifters which make them narrowband beamforming networks [8–13]. On the other hand, the Rotman lens-based BFN is a true time delay (TTD) device, as it does not suffer those limitations. It provides beam steering independent of the frequency. Thus, it exhibits wideband properties. However, in the open literature, the vast majority of the Rotman lens-based BFN designs concentrate on the phase error performance, while a few works consider the amplitude performance, which is an important factor. The proposed work manages both the amplitude and the phase error at the same time in order to determine the design parameters of the proposed Rotman lens.

1.5 Objectives

This work focuses, mainly, on the designing of a high-performance Quasi-Yagi antenna and Rotman lens-based analog beamforming networks for 5G and mm-wave applications. The objectives of this thesis can be classified into four parts. Firstly, the designing of a thin dielectric lens antenna (DLA). This is to achieve a high gain for wireless communication by improving the propagation characteristics of a dielectric slab waveguide (DSW) in front of a planar Quasi-Yagi antenna. The improvement involved modulating the DSW surface by means of perturbation based on subwavelength gratings and effective medium theories. Furthermore, a mathematical model for the design of DLA was provided in order to predict the antenna gain and bandwidth performance. Secondly, the construction of a beamforming network based on the Rotman lens being capable of steering the beam within a reasonable scanning angle in the azimuth plane for a linear array of the designed DLA. Thirdly, the implementation of the same beamforming network by using the 3D printing ridge gap waveguide (3DP-RGW) technology [14,15] as well as improve the performance of the beamforming network by eliminating the dielectric and radiation losses associated with the PCB technology. Lastly, the implementation of the beamforming network by using the printed version of the RGW (PRGW) as a compromise solution. PRGW possesses the ease of fabrication with the PCB technology, in addition to the advantage of the wave propagation in the air only as of the metallic RGW.

1.6 Contributions

This work can be considered as a step toward designing high gain, wideband, low profile, and low-cost antennas for potential mm-wave applications and beamforming networks. The work contributions can be summarized as follows:

1. Two variants of high gain broadband mm-wave antennas are presented. In essence, the propagation characteristics of a DSW that works as a dielectric lens in front of a Quasi-Yagi antenna is improved based on subwavelength gratings and effective medium theories. Accordingly, an accurate design methodology for obtaining a certain gain and bandwidth performance for a planar Quasi-Yagi antenna with extended DSW is provided. The suggested design methodology results in the designing of a single element Quasi-Yagi

antenna with a high gain of 15 dBi as well as a wideband (24–40) GHz for $|S_{11}|$<-10 dB. The antenna provides quite a good performance of 95% aperture efficiency with a high measured gain at 30 GHz [J1,C2].

2. A Quasi-Yagi antenna array—that is, fed by a Rotman lens capable of scanning the beam within 80º (± 40º)—was designed and fabricated using standard planar low-cost processing PCB technology for MMIC covering the whole Ka-band. The proposed system was designed according to an accurate design methodology for optimum wideband high gain Rotman lens-based analog BFN, which is provided. The design methodology takes care of both the amplitude and the phase error of the BFN. Consequently, the proposed BFN—with its compact size of 70 mm×50 mm, high measured gain of 14 dBi, and very low phase error ±6.6°—is qualified for a wide range of potential mm-wave applications such as the advanced multiple-input multiple-output (MIMO) and hybrid beamforming networks [J2,C3].

3. Two wideband high gain analog BFNs based on 3DP-RGW and PRGW are introduced in order to eliminate the dielectric and radiation losses associated with the PCB processing technique. The PRGW is introduced as a means to avoid the exceptional cost of the metallic RGW. Both of the BFNs show good performance. The S-parameters are better than -10 dB impedance in the band (27.5-40) GHz for the 3DP-RGW and (26.5-40) GHz for PRGW. Moreover, about 1 dB insertion loss improvement is achieved using RGW—that is, compared to MS technology. The 3DP-RGW BFN is capable of steering the beam within ±39.5° with maximum measured gain of 14.95 dBi at 37 GHz and maximum phase error of ±6° while the PRGW Rotman lens was designed to steer the beam within ±30° [J3].

1.7 Thesis Organization

The thesis is divided into six chapters. The first chapter covers a general overview regarding 5G, the thesis motivations, and objectives. After that, the next chapter presents a literature review for different mm-wave fabrication technologies—that is, along with different mm-wave antennas as well as a brief comparison between them. What is more, this chapter addresses the 5G basic

requirements as high gain antennas and beamforming networks, and it also provides the methodology for designing such systems as well as the related theoretical background. Based on a comprehensive study of different mm-wave antenna designs, the Quasi-Yagi and DLA were selected to be the core of the thesis. Chapter three describes the designing of two variants of high gain broadband mm-wave antennas by improving the propagation characteristics of a DSW—that is, one that works as a dielectric lens in front of a Quasi-Yagi antenna, which is based on subwavelength gratings gratings and effective medium theories. The first antenna was designed using parallel lines dielectric corrugation, and the second one was designed using two-dimensional circular air holes in a DSW. Chapter four is an analysis of the analog beamforming network, which is based on the MS-Rotman lens with 80° scanning angle capability in the azimuth plane that is presented. Chapter five discusses the implementation of the Rotman lens by RGW technology as well as its printed version (PRGW), which was aimed at reducing the dielectric losses associated with the MS one. And finally, the last chapter summarizes the results obtained in this thesis and suggests further developments.

CHAPTER 2: Scope of Work and Literature Review

2.1 Introduction

For many mm-wave short range wireless communications network applications—such as 5G cellular communication systems, imaging systems, mm-wave high-speed indoor or outdoor wireless communication systems, as well as other applications—it is desired to have high gain antennas in order to compensate significant losses, especially rain attenuation and atmospheric absorption losses. At the same time, many challenges that researchers are facing involve developing antenna systems to counter such losses. Similarly, beamforming networks are essential 5G requirement because, in some cases, the signal blockage cannot be avoided by using a direct route between two mm-wave transceivers. Therefore, BFN is used to re-route the signal in the desired direction. One of the challenges is the proper design of a low cost, reduced size, and efficient antenna system. 5G requirements were determined based on users' expectations for the new applications and services. These requirements were quantified, related, and detailed by different standardization organizations such as the radio sector of international telecommunication union (ITU-R), the 3rd Generation Partnership Project (3GPP), Institute of Electrical and Electronics Engineers (IEEE), The Federal Communications Commission (FCC) in the USA, and other bodies. Robust statistical spatial channel modeling, streamlined beamforming algorithms, new power-efficient and air-interface standards, more advanced high gain antennas systems, and beamforming networks are the main requirements among many other design challenges [2]. What really matters with antenna designers from these requirements are those related to antenna, and beamforming networks. Antenna and beamforming network design—with a high and stable gain in the recommended mm-waves band—is a crucial issue. Recently, several antennas and beamforming networks of different fabrication technologies, geometries, and performance have been investigated for mm-wave applications [15-32]. The following sections will define the scope of work of this dissertation and provide further elaboration regarding various proposed modern mm-wave fabrication technologies, antenna structures, and beamforming networks to obtain reasonable gain and bandwidth performance at mm-waves band.

2.2 Fabrication Technologies

Conventional mm-wave antennas are made as planar and nonplanar structures. Planar structures consist of thin film metallic patterns in a single layer or multi-layer medium. They are low profile and can be easily integrated with MMIC technology as well as low profile applications. Multi-layered PCB and low-temperature co-fired ceramics (LTCC) circuits are the two low-cost conventional fabrication technologies [16]. However, the main disadvantage of traditional planar, PCB-based mm-wave antenna is the higher dielectric loss—with loss tangents values of the order of 10^{-2}—which degrades radiation efficiency, radiated power capabilities, and fabrication difficulties when reduced to the sizes necessary to operate within this band. Combining high performance in the low mm-waves band with low fabrication costs—which offer the capability for high volume production—is one of the significant current trends in planar mm-wave circuit technology. LTCC has low dielectric loss, precise and stable line dimensions, precise dielectric relative permittivity, high-quality surface finish, and low processing costs. Moreover, LTCC has the potential to incorporate multi-layer structures and buried passive components—with minimal processing steps—leading to very compact mm-wave subsystems [16,17]. That said, nonplanar structures—such as horn antennas—and some antenna structures that involve rectangular waveguides are relatively bulky, expensive, and not compatible with MMIC. Alternatively, substrate integrated waveguide (SIW) is an approach for low-cost mm-wave RF circuits. Essentially, it provides a compact, high-Q, high power capacity, and the possibility of integration with low profile feeding structures. Accordingly, it can also minimize radiation loss and parasitic radiation [18]. Although SIW takes advantage of both waveguide and microstrip structures, the use of dielectric materials still introduces unwanted losses that would not be acceptable for high-frequency applications. One of the promising guiding structures is the RGW. This guiding structure is fabricated in different forms, such as metal, printed RGW (PRGW), and metalized 3D-Printed RGW (3DPRGW). The metallic RGW and the 3DRGW are bulky structures connected to the mm-wave devices, whereas the PRGW is implemented using a traditional PCB technology. RGW provides low signal distortion and low losses compared to microstrip line and SIW [19,J2].

Integrating multifunctional modules (digital, RF, optical, etc.) into a single platform provides a wide range of features such as intelligence, high performance, low cost, and low power-consumption wireless communication systems. Microelectromechanical systems (MEMS) enable

the production of antennas and RF components with features of reconfigurability in the polarization, frequency, and radiation pattern. Moreover, the monolithic fabrication of the antenna—together with these tunable RF components— significantly reduces the power losses as well as the parasitic effects compared to ordinary discrete components [20]. One limitation of MEMS technology is that analog control generally does not provide sufficient reliability or temperature stability, so, instead, digital elements are used in a manner similar to the use of PIN diodes in semiconductor technology. This implies increased network complexity in terms of a unit cell and biasing. Another issue, although MEMS is becoming a mature technology and can provide excellent properties up to V or W band, new technologies are still needed to address the growing interest in the mmwave [21]. Recently, a number of MEMS-based mm-wave antennas has been reported upon [21–27].

Latest revolutions in the development of silicon semiconductor technologies—such as complementary metal oxide semiconductor (CMOS) and BiCMOS—allow the development of single-chip integrated mm-wave radars with On-chip embedded antennas [28-30]. The On-chip fabrication technology is also called Radio Frequency Integrated Circuit (RFIC) technology. 3D printing technology is also one of the mm-wave fabrication technologies that integrate antenna with a small mm-wave platform [15, 31, 32].

2.3 Millimeter Wave Antennas

Generally, antennas are classified in terms of different factors that include gain, matched impedance bandwidth, radiation type, and size of the structure. Based on specific requirements for a mm-wave communication system, the antenna type is selected and designed to meet those requirements. Microstrip antenna is the most common type of antenna, with a wide range of applications due to its apparent advantages of lightweight, low-profile, low cost, planar configuration, ease of conformal, superior portability, suitable for an array of purposes with the ease of fabrication, and integration with MMICs. Similarly, Leaky-wave antennas have been extensively studied in the last few decades, and their main attraction is their high directivity, wide bandwidth, and ability to scan with frequency. The leaky wave antenna consists of a guiding structure that is designed to leak at least 90% of traveling wave energy before it reaches the end of the antenna—that is, provided the antenna length is 5–20 wavelengths long. Based on the

geometry, principle of operation, and structural perturbations, leaky-wave antennas can be divided into several categories. However, the most basic distinction is between one and two-dimensional leaky-wave antennas. These can be identified as periodic, uniform, or quasi-uniform structures [33, ch. 2; 34, ch. 11]. A fractal antenna is another type of antenna that uses space filling or self-similar design in order to increase the effective length—or increase the boundary of material—that it can receive or transmit via electromagnetic radiation within a given total surface area or volume whilst preserving the electrical length of the antenna. Fractal structures act as natural inductive loading into an antenna. In space filling, the geometry of a fractal antenna is generated through several iterations of a generator shape. For some fractals, the overall geometry is duplicated on a reduced scale within a small region [34, ch. 6; 35]. A slot antenna is a type of very low-profile aperture antenna. It can be conformed to any configuration. A slot antenna has the advantage of resolving the bandwidth limitation of Co-Planar Waveguide (CPW) antennas (CPW fed microstrip antenna), which are widely used in many applications in microwave and mm-wave frequency bands. The bandwidth of a standard CPW antenna is about 1–2%, but such bandwidth is inefficient for future 5G communications systems at mm-wave band [36]. Therefore, CPW fed slot antennas are used to provide wider bandwidth. A tapered slot antenna (TSA) is a traveling wave planar antenna that attracts antenna designers for its wide bandwidth and high gain. The energy in the traveling wave is strongly bound to the very small separated conductors—that is, compared to the free space wavelength—and it becomes increasingly weaker as the separation is increased and more coupled to the radiation field. The TSA is well-suited for integration with uniplanar circuits due to its slot line geometry [37–39]. Another form of travelling wave structures is Dielectric rod antenna, which has been researched for many years. Dielectric rods are easy to design and low-cost antennas. They are, also, easy to machine and have a light weight, but, more importantly, they are easily integrated with miniature waveguide systems [40]. Likewise, Dielectric resonator antennas (DRAs) offer many attractive advantages over other low-gain antennas such as microstrip antennas or dipoles. These advantages include the design flexibility as well as a high radiation efficiency, even at mm-wave frequencies, which due to the absence of surface wave losses and minimal conductor losses. DRAs can be designed from various shapes of dielectric material. DRAs are suitable for an array of potential designs where no mutual coupling between elements makes designing easier [41,42]. However, DRAs are moderate gain antennas. Another form of antennas is the Lens antenna. it can change spherical waves into flat plane waves

in order to achieve a higher gain and a narrower beamwidth. It is similar to the ability of an optical lens to straighten the spherical wavefronts. When incident waves face the discontinuity between the dielectric medium of lens and air, part of incident rays are transmitted and, partially, get refracted. Many lens techniques, shapes, and materials had been investigated in the literature for mm-wave antennas [43]. Although these lens systems exhibit a high gain of 23 dB, the use of lens makes the system bulky and non-planar. DLAs can also be made as planar structures—that is, usually with some additional treatment for bandwidth and gain enhancement, which is presented in [J1]. Log Periodic Antenna (LPDA) is an antenna that has its impedance and radiation characteristics periodically repeat. LPDAs are usually frequency independent to ensure that their pattern, gain, and impedance remain acceptable and relatively stable over a wide frequency range [34]. An LPDA planar version (PLPDA) is realized using PCB fabrication technology. It can also be implemented using SIW technology [44]. Planar Yagi-Uda or Quasi-Yagi antenna is a new antenna structure formed by combining the microstrip radiator technique and the traditional Yagi-Uda array concept. However, the electromagnetic coupling between the driven element and the parasitic elements is not only through space—such as the traditional Yagi-Uda antenna—but also by the surface waves in the substrate [45,46]. The printed quasi-Yagi antenna has attracted much attention for it use in microwave and millimeter wave applications, which is because of the advantages such as low profile, lightweight, high gain, broadband, high radiation efficiency, and ease of fabrication. For these advantages, Quasi-Yagi antenna is selected to be the main part of the proposed single antenna element in this work with some modifications and additions.

2.4 Beamforming Networks

Beamforming is a key enabling technology for 5G. It is, essentially, used to overcome two main problems: mm-wave blockage by objects and signal attenuation over long distances. In addition, beamforming helps by focusing a signal with a concentrated beam that points only in the specific direction—that is, rather than omnidirectional broadcasting. This approach can strengthen the signal in the desired direction and, also, reduce interference with the surrounding environment. There are three main types for beamforming. Analog, digital, and hybrid beamforming. Our focus in this research is on the analog beamforming which has two major classes. Matrix-based analog beamforming and lens-based analog beamforming. The Butler matrix, the Blass matrix, and the

Nolen matrix are well-known examples of matrix-based analog beamforming networks. The Butler matrix is simple and easy to realize and has been widely used in microwave band. However, it has limitations due to phase shifter and crossover designs, that leads to a low achievable gain, and a low scanning plane. All these issues make it hard to be utilized for mm-wave short range wireless communication networks. Similarly, the Blass matrix design and the Nolen matrix design involve many couplers and phase shifters which make them narrowband beamforming networks [8-13]. On the other hand, the Rotman lens-based BFN is a true time delay (TTD) device, as it does not suffer those limitations. It provides beam steering independent of the frequency. Thus, it exhibits wideband properties. *Figure 2.1* shows two well-known analog beamforming techniques: Butler Matrix and Rotman lens.

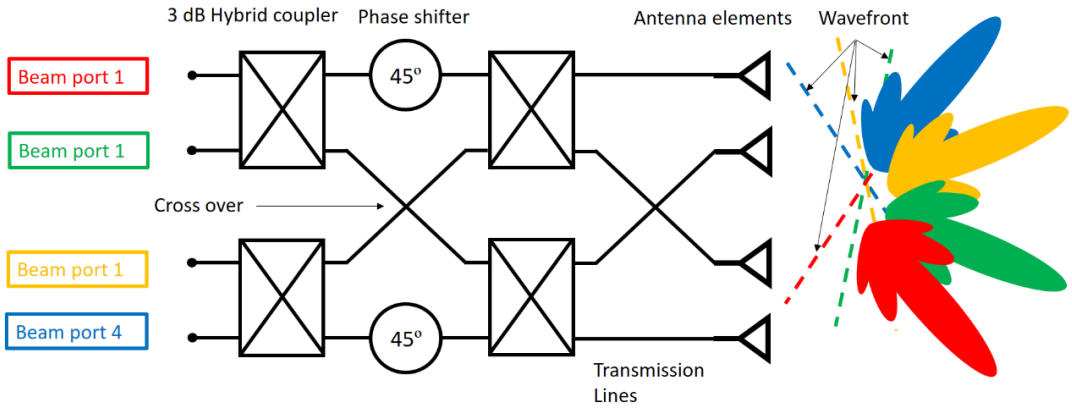

(a)

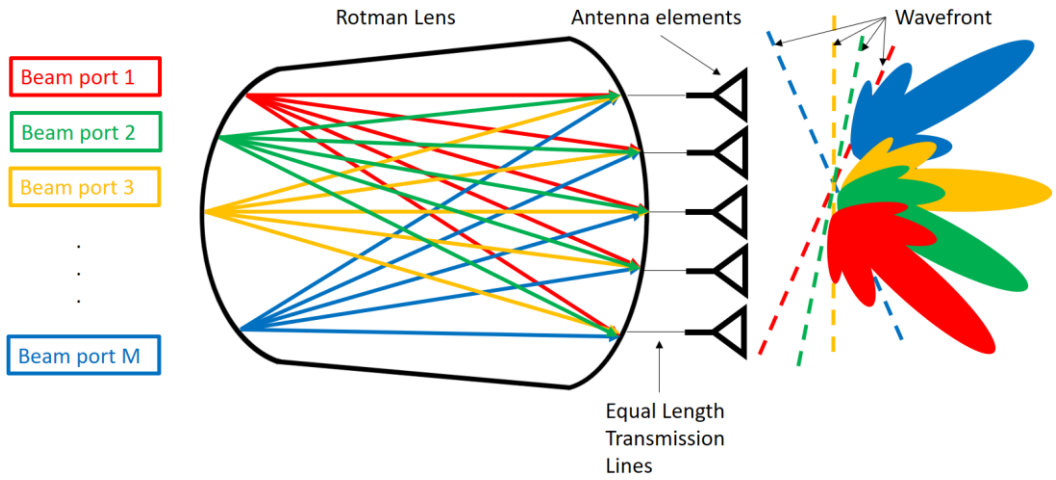

(b)

Figure 2.1: Beamforming Networks: (a) Butler matrix and (b) Rotman lens

2.5 Literature Survey

Quasi-Yagi antenna and planar dielectric lens antenna (DLA) are selected from different types of mm-wave antennas for advantages of low profile, lightweight, ease of fabrication and installation, high directivity, and high radiation efficiency to develop a new type of mm-wave antennas. Section 2.3.1 covers a survey of different Quasi-Yagi antennas available in the open literature, while section 2.3.2 presents different Rotman lens-based analog BFNs.

2.5.1 Qausi-Yagi Antenna

The Qausi-Yagi antenna's bandwidth performance is highly reliant on its feeding network. Consequently, different excitation and transition methods have been proposed in the literature to achieve broadband.

A microstrip line-to-coplanar strip line (MS-to-CPS) transition is proposed in [47]. This excitation method results in about 30.3% fractional bandwidth (FBW). Using coplanar waveguide-to-coplanar-strip (CPW-to-CPS) transition, 11.6%-44% FBW can be achieved as reported in [48], and [49]. Coplanar stripline-to-slotline (CPS-to-SL) is used in [50], and [51] providing FBW of 52.6%, and 97%, respectively. A Quasi-Yagi antenna with 83.7% FBW is reported in [52] using a microstrip-to-slot line transition (MS-to-SL) structure. CPS-to-SL and MS-to-SL have the maximum FBW between these techniques. MS-fed [53], and CPW-fed [54] are also used for exciting the Quasi-Yagi antenna with a broadband. The printed Quasi-Yagi antenna has been used as an endfire antenna in different frequency bands for diverse applications. In [55] a Quasi-Yagi antenna is proposed for WiMAX and WLAN applications. The antenna achieves two wide bandwidths, 2.3–3.7 GHz (46.7%) and 5–6.25 GHz (22.2%), and high stable gain (8.5 ± 0.9 and 9 ± 1 dB) within these two operation bands. However, the antenna structure is bulky and difficult to be integrated with planar structures. A printed Yagi-antenna with bandwidth of (1.84-4.59) GHz and gain (4.5-9.3) dBi for WLAN, WCDMA, LTE applications is presented in [56]. Nevertheless, there is a large variation in the antenna gain over the reported bandwidth. The author suggests decreasing the number of the directors to retain gain stability. However, this will reduce the total gain. Another Quasi-Yagi antenna that is demonstrated in [57]. The design, simply, integrates an arc-shaped strip, which serves as a near-field resonant parasitic (NFRP) element, and a coplanar-waveguide (CPW)-fed semiloop antenna. The antenna has a very compact electrical size of $0.17\lambda_0$

× $0.43\lambda_0$ and 5.6 dBi directivity. However, this Quasi-Yagi antenna has a narrow bandwidth of (5.06%) FBW and does not meet the requirements of 5G antenna system. A microstrip-fed millimeter-wave Yagi-Uda antenna with applications as a single element radiator or for switched-beam systems with gain of 10 dBi is presented in [46]. The antenna has a wideband operation (22–25 GHz). Although 1×2 antenna array of this Yagi-Uda has (9-13) dBi gain, still insufficient for 5G communication link [2,58]. In addition, the antenna electrical size of $2.3\ \lambda_0 \times 3.3\ \lambda_0$ is relatively large. In [59], a 60-GHz 1×4 antenna array with ladder-like multi-directors is presented. The single-stage multi-directors are introduced for gain improvement, side lobes reduction, and bandwidth extension. The antenna exhibits a medium gain of 11 dBi. Such gain does not meet the minimum 5G system gain requirement [2,58].

Similarly, DLAs are widely used for gain enhancement purpose, but the DLAs of high gain are, mostly, designed with thick substrates or bulky structures. A patch fed planar dielectric slab waveguide extended hemi elliptical lens antenna is described in [60]. The lens weighs only 90 g. The maximum lens dimensions are $11\ \lambda_0 \times 13\ \lambda_0$ in the lens plane and it is $0.6\ \lambda_0$ thick. The operational bandwidth is 18 to 30 GHz with 18.5 dB measured gain at 28.5 GHz. In [61], a 120mm diameter and 6.4mm thick planar Luneburg lens antenna is presented. The lens is composed of a shape contoured fixed dielectric constant disc, with a total weight of 45 g with 16.8 dB gain, 10% fractional bandwidth (FBW) and cross-polarization better than -20 dB. The size of both antenna systems reported in [60,61] is electrically large.

In this work, we present a new type of planar antenna as a potential candidate for 5G applications. The proposed antenna is a combination between a Quasi-Yagi antenna, that is excited by MS-to-SL to have a broadband, and a planar dielectric lens. The single element of the proposed antenna has four major advantages over the previously mentioned antennas. A gain improvement of 3.5–5.5 dB compared to the two elements array reported in [46], more efficient in terms of wide bandwidth with more than 17 GHz (42 % FBW), smaller compact size, the same gain of [46] can be obtained with only $0.5\lambda_0 \times 4.8\lambda_0$ including the planar dielectric lens. The basic idea of the new antenna relies on modifying the geometry of the Quasi-yagi antenna elements and controlling the wave propagation characteristics of a thin dielectric slab waveguide (DSW) by introducing a perturbation in the DSW. Although this method has been used previously to improve the performance of different antenna systems and microwave components [62-65], however, the provided effective permittivity calculation was reported with via diameter dependency only, while

there is another factor that should be accounted in designing this type of planar dielectric lenses, which is the spacing between air-vias. The provided effective permittivity calculation here includes the radius and the spacing between the air holes in two dimensions based on the subwavelength gratings and the effective medium theories. Consequently, a design methodology for high gain planar Quasi-Yagi with dielectric lens antenna is presented. The proposed methodology provides more flexibility to the design and fabrication processes.

2.5.2 Beamforming Network

Recently, Rotman has attracted much attention for use in 5G wireless networks. In [66], Rotman lens fed a wideband (25-30) GHz microstrip antenna array for use in 5G wireless communication applications is presented. The BFN is realized using a simple and low cost printed circuit board (PCB) technology to operate at 28 GHz with (-40º to +40º) scanning range. However, the reported measured reflection coefficients indicates a poor matching performance (S_{11}< -8.5 dB). Another BFN with similar fabrication technology is presented in [67]. The basic idea is realizing a folded Rotman lens with the use of aperture coupling by multi-branch slots for the transition between the lens layers. In addition, rectangular slots are used to feed an array of patch antenna elements on the top layer. The BFN exhibits a scanning capability of ±30º and good impedance matching between 26 GHz to 29 GHz with a maximum gain of 14 dBi. Although 50% size reduction is achieved, compared to the conventional Rotman lens, the multi-layer structure increases the overall thickness to 6 mm making it relatively bulky. Also, the use of patch antenna limits the bandwidth of the BFN. Substrate integrated waveguide (SIW) Rotman lens is presented in [68-71]. Seven beam ports and nine array ports Rotman lens for beam switching application is presented in [68]. The system has a scanning capability over ±24º in X-band. Nevertheless, in SIW Rotman lens the distance between adjacent beam ports and adjacent array ports must be large to avoid interference between neighbor waveguides. Consequently, the lens size increases compared to PCB-based Rotman lens. More importantly, metallic vias deteriorate S-parameters and amplitude distribution on array elements [69]. A dual-layer Rotman lens with 50% size reduction, compared to a conventional one, is introduced in [70,71] using SIW technology in the 24-GHz band. However, the multilayer structure and the size of 7.2 λ0 ×12 λ0 is electrically large. Furthermore, SIW Rotman lens-based beamforming or multibeam systems of [68-71] show a very

narrowband performance (~4%-7%), which reduces the spectrum utilization of a TTD component such as Rotman lens. Alternatively, ridge gap waveguide (RGW) technology is proposed to realize Rotman lens for the advantage of only metal and air are used; therefore, the dielectric losses associated with PCB or SIW technologies are eliminated [15,72]. A RGW Rotman lens is proposed in [73] for beam scanning in millimeter wave applications. The design shows a good performance in terms of S-parameters, especially the transition between RGW and WR28 in the input and output ports. However, 56 mm is needed just for transition section between RGW and WR28 for each input, or output port, in addition to 50 mm for the parallel plate region of Rotman lens results in a massive structure. Besides, to the authors' best knowledge, the physical implementation and measurement results of mm-wave RGW Rotman lens are not reported yet in the open literature. Also, machining of such device in the mm-wave band is exceptionally costly. Subsequently, there are some trials to reduce the implementation cost using metalized three-dimensional printing technology (3D-Printed) as reported in [15]. This might explain why only a few solutions have been reported so far to implement mm-wave Rotman lens using RGW or 3D-Printed. Another possible technique is the printed version of RGW (PRGW), which is, by far, lower cost than RGW. In [74] PRGW Rotman lens operating at 60 GHz is proposed. The lens scanning range is ±40º. This solution reduces the dielectric losses, where the wave, in this case, propagates mainly in the air. However, the size of the BFN will increase, especially, when it is scaled for 28, or 38 GHz suggested for 5G [2,5,6] and also the use of air instead of a dielectric material increases, generally, the physical size. The inkjet processing technique is also possible for realizing Rotman lens with a low profile and low cost such as proposed in [75].

In this work, Rotman lens feeding eight Quasi-Yagi antenna array is implemented in two different fabrication technologies, the PCB and RGW. The proposed lens was designed to operate in the frequency band 26-40 GHz, where it is reported as one of the candidates for 5G wireless communications system for both indoor and outdoor devices [76]. The lens was designed according to Hansen's design procedure for optimum Rotman lens parameters with maximum gain and minimum phase error [77]. The proposed work takes care of both the amplitude and the phase error at the same time to determine the design parameters of the proposed Rotman lens. The performance of the proposed BFN is compared to related beamforming systems with different fabrication technologies and exhibits a relatively high gain, broadband, and reasonable scanning

performance in addition to the presented PCB–based BFN is low-cost, low profile MMIC compatible.

2.6 Theoretical Background and Methodology

In this section, the theoretical background and the design methodology for the proposed single antenna element and the Rotman lens-based beamforming network are presented.

Subsection 2.6.1 explains the analysis of the expected losses in the antenna structure and the propagating modes in the DSW. After that, a brief design methodology is summarized in subsection 2.6.2.

Similarly, the proposed Rotman lens-based BFN was designed with the PCB technology to satisfy the performance optimality in terms of two important factors: phase error and amplitude performance. Subsection 2.6.3 provides the analysis of the proposed Rotman lens-based BFN, while subsection 2.6.4 summarizes a brief design methodology.

Compared to the PCB, RGW provides low signal distortion and low losses. It depends, mainly, on the soft and hard surface principle explained in subsection 2.6.5. The starting point for designing RGW is determining its operational frequency band, which is ideally, the stop band of a unit cell of a certain electromagnetic band gap (EBG). Because the surrounding surfaces are periodic structures that form parallel plate gap waveguides with one textured metal pin surface, they should be designed based on numerical analysis for a unit cell of specific EBG as in subsection 2.6.6 [78].

2.6.1 Analysis of the Expected Losses and the Propagating Modes

As described in the above, the first part of the proposed antenna is fed by a microstrip line. Thus, there will be an attenuation due to the conductor loss. Nevertheless, this type of loss is considered low compared to the attenuation in a lossy dielectric material. However, the length of the microstrip line is very short compared to the dielectric lens of the proposed antenna. The dielectric loss is the dominant effect of wave propagation in the DSW [79]. Even though the dielectric attenuation level for all frequencies in the band ranges below (0.93 to 1.27) dB throughout the entire DSW length, the gain sharply drops when the frequency exceeds 32 GHz. Therefore, the investigation is extended to the propagating modes that could be supported by the DSW.

It is commonly desired to operate an antenna system with a single mode of propagation, and this can be achieved by respecting the cutoff frequency for a certain mode in a DSW. Because the geometry of the proposed antenna has a rectangular DSW, it supports TM_{mn} modes. For a thin DSW with a high dielectric constant, the boundary between the surrounding free space (air) and the DSW can be approximated by a perfect magnetic conductor (PMC), as depicted in *Figure 2.2a*. The wave inside an ordinary DSW is a combination of fundamental mode and undesired modes. Therefore, the DSW surface should be modified to block HOM propagation. Subwavelength grating provides a solution for such a situation. This is, simply, achieved by introducing grooves to the DSW surface shown in *Figure 2.2b*, provided that the groove period is much smaller than the wavelength ($d \ll \lambda_{eff}$) to preserve the homogeneity of the propagation medium.

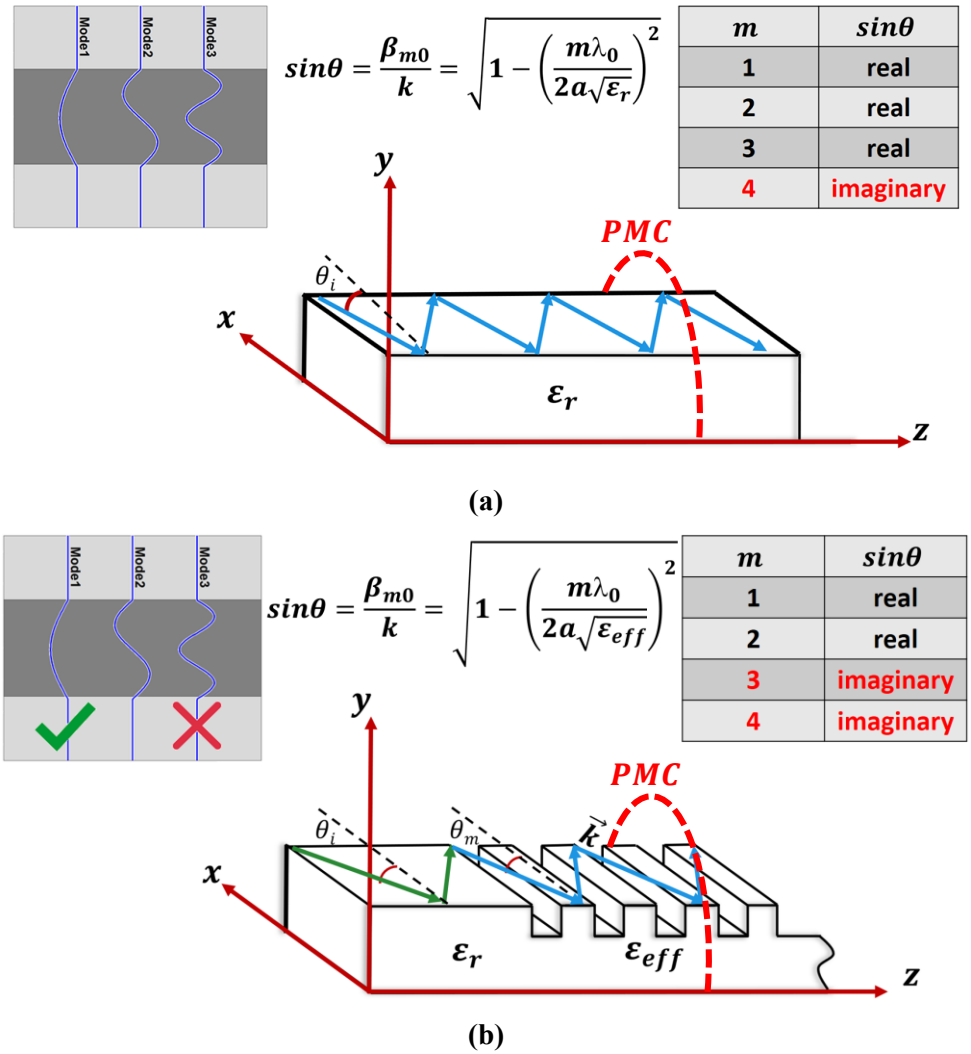

Figure 2.2: Schematic diagram for the modes propagation: (a) Plain DSW. (b) Corrugated DSW.

The effective dielectric constant of the corrugated DSW depends on the corrugation duty cycles (f_w) and (f_h), shown in *Figure 2.3*, which determine the corrugation width and depth, respectively:

$$\varepsilon_{eff} = \varepsilon_r + f(1 - \varepsilon_r) \qquad (2.6.1)$$

$$f = (1 - f_w)(1 - f_h)$$

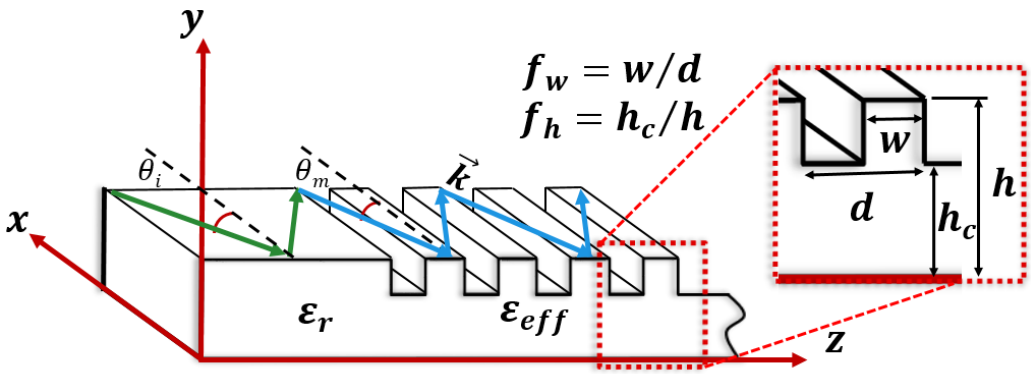

Figure 2.3: Corrugation duty cycles.

However, if the subwavelength grating condition is not held ($d\ is\ not \ll \lambda_0$), then the corrugated DSW is no longer homogenous medium and the wave will experience two different media. The first medium is the wide groove region, which has an effective dielectric constant given by (2.6.1) and $f_w = 0$ in this region. The second medium is the corrugation tooth, which has a dielectric constant value of the original material of the DSW (ε_r). Hence, the wave is reflected towards the boundary of the DSW and the surrounded medium, that will cause another reflection as illustrated in *Figure 2.4*.

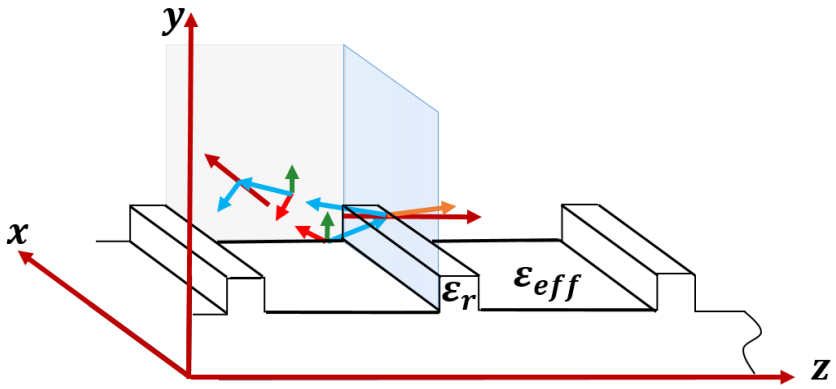

Figure 2.4: Inhomogeneous DSW due to improper corrugation period.

For a single mode of propagation, the effective dielectric constant of the grating surface should be designed in order to allow the fundamental mode to propagate with a real phase constant (β_{10}) while all possible propagating HOMs would have imaginary phase constants ($\beta_{20}, \beta_{30}, \dots$) —that is, according to the following equation:

$$\frac{\beta_{m0}}{k} = \sqrt{1 - (\frac{m\lambda_0}{2a\sqrt{\varepsilon_{eff}}})^2} \quad , m = 1,2,3, \dots \tag{2.6.2}$$

a is the DSW width.

If the rectangular corrugations in the DSW are replaced by perforating, two-dimension circular holes' lattice, as depicted in *Figure 2.5*, the effective permittivity is given by

$$\varepsilon_{eff} = \varepsilon_r + \frac{\pi {r_h}^2}{d_x d_z}(1 - \varepsilon_r) \tag{2.6.3}$$

$$N_h = \lfloor (a - 2c + s_x)/(2r_h + s_x) \rfloor \tag{2.6.4}$$

Where r_h is the radius of the circular hole, N_h is the number of holes along x-axis and depends on some fabrication constraints such as clearance margin (c) from substrate's edges and edge-to-edge spacing between adjacent holes (s_x), a is the substrate's width, and s_z is the edge-to-edge spacing between two adjacent holes along z-axis. Period $d_x = (2r_h + s_x)$ and $d_z = (2r_h + s_z)$.

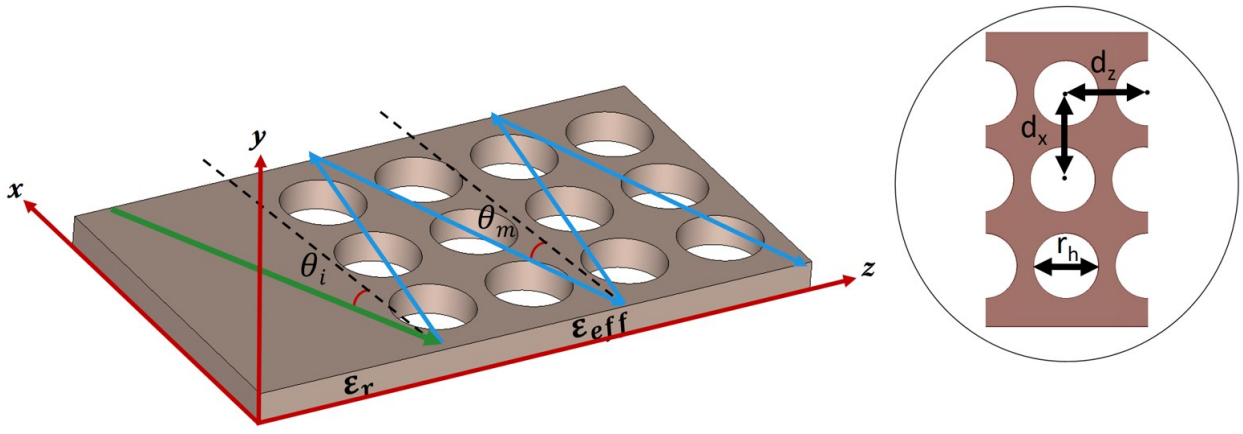

Figure 2.5: Perforated DSW in two dimensions.

2.6.2 Designing Methodology of the Proposed Single Antenna Element

The proposed Quasi-Yagi antenna with perturbed DSW based on gratings and effective medium theories can be designed according to the following brief and simple designing steps:

1. Determine the frequency bandwidth (f_{min} - f_{max}) assuming about 40% as an initial guess FBW.
2. Select a substrate with a high dielectric constant to minimize the antenna size. The substrate thickness should allow good corrugation depth from the mechanical prospective (avoid ceramic material), and the thickness should be as minimal as possible to avoid cross-polarization, especially for higher mm-wave frequencies.
3. On the top layer of the selected substrate, set the length of the following antenna parts to be:
    a. Ground plane width of $1.34\ \lambda_{eff}$ of the center frequency in the band.
    b. One λ_{eff} driver for high directivity.
    c. Use one (or more) multi-director of about $(0.25 \text{ to } 0.3)\ \lambda_{eff}$ width with about $(0.1 - 0.15)\ \lambda_{eff}$ spacing.
    d. Keep around $0.25\ \lambda_{eff}$ distance between driver and antenna ground plane.
    e. Taper the driver to improve the antenna bandwidth performance.
    f. Make a reasonable slot between the two sides of the driver to allow MS-to-SL transition. The slot's width is about $(0.1\ \lambda_{eff})$ and, generally, should be optimized to achieve a good antenna impedance matching.
4. On the bottom layer of the substrate, use a U-shape microstrip line of width corresponding to an impedance R_{in} , where R_{in} is the Quasi-Yagi array's input impedance measured at the center of the driver element. The dimensions of the balun should be optimized to counter the imaginary part of the input impedance $(R_{in} + jX_{in})$ and, also, provide a good matching. This line is followed by section(s) of microstrip line to match the antenna to 50 Ω port.
5. Calculate the maximum effective dielectric constant that ensures single mode of operation using (2.6.2).
6. Select proper air-hole radius and period using (2.6.3).
7. Determine the number of holes along x-axis using (2.6.4).
8. Set the total length of the antenna according to the required gain assuming an average aperture efficiency is 85%.

2.6.3 Performance Analysis of the Proposed Rotman Lens-based BFN

A typical Rotman lens has *M*-beam ports, *N*-array ports, and *D*-Dummy ports. The lens can form *M*-discrete beams in different angular directions. According to Hansen's procedure for designing Rotman lens, the designer should specify the number of radiating elements (*N*) to obtain specific gain performance [77]. Also, the spacing (*d*) between array elements on the array axis, is determined based on the wavelength of a designated frequency, and the desired maximum beam steering angle ($\pm\theta_0$). The radiating element should have a 3dB beam width (BW) greater than or equal ($2\theta_0$). Those are the general requirements of the BFN. Then, the minimum number of Rotman lens beam ports (*M*) for continuous beamforming is calculated according to the 3dB BW of the resultant *N*-elements array's pattern for the maximum frequency in the designated band as follows:

$$M = \left\lceil \frac{2\theta_0}{BW_{array}} \right\rceil \tag{2.6.5}$$

After determining the number of beam ports and array-ports, the parallel-plate waveguide region that connects beam ports and array-ports is designed based on four significant parameters ($f_1, \alpha, \beta, and\ \gamma$). *Figure 2.6* illustrates some of these parameters, where f_1 is the (on-axis) focal length, f_2 is the off-axis focal length, and both are taken from the three points F_0, F_1, and F_2 ("foci") of the beam port contour, which is the reference for the input waves and therefore, has no phase errors. If Rotman lens was fabricated on a dielectric substrate, the substrate permittivity (ε_r) is specified, and the dimensions of the lens are reduced by a factor of $\sqrt{\varepsilon_r}$ [80]. For a designated maximum scanning angle θ_0 and a specific array length of *(N-1)d*, a primary geometrical constraint on the lens on-axis focal length is set to maintain a good amplitude performance as well as keep angles and distances between different input and output ports that are relatively closed to each other [80]:

$$f_1 \gtrsim 2(N-1)d\sin\theta_0 \tag{2.6.6}$$

The focal angle α is the angle between the on-axis and off-axis focal lengths and the ratio between them is β [77].

$$\beta = f_2/f_1 \tag{2.6.7}$$

γ is an expansion factor, which is the ratio between the sin of beam steering angle (θ), corresponding to the off-center focal point, and the sin of the focal angle (α) as follows [77]:

$$\gamma = \sin\theta/\sin\alpha \tag{2.6.8}$$

y_3 is the position of a typical antenna element on the array axis as shown in *Figure 2.4.* Another critical parameter is the indirect factor of utility ζ, which has a crucial effect on the amplitude and the phase error performance of the lens [77]. ζ is given by

$$\zeta = y_3\gamma/f_1 \tag{2.6.9}$$

α and β must be conjunctionally selected with other parameters to obtain an acceptable amplitude performance and minimize the phase aberrations. These aberrations are resulted by the difference in path lengths between a central ray of length (h = H/f_1) through the center of the array-ports contour and any other ray of length (l= L/f_1), both of which are traced from an arbitrary point on the beam ports contour through the lens and normally terminate to the generated wavefront as shown in *Figure 2.6.* The normalized path difference is a function of both the scan angle θ and the position along the array contour ζ , and can be derived geometrically [81].

$$\delta P = \sqrt{\varepsilon_r}\,(l-h) + \sqrt{\varepsilon_e}\,W + y_3\sin\theta \tag{2.6.10}$$

Where ε_e is the effective dielectric constant in the transmission lines region. Furthermore, various optimization methods can be used to solve the following objective function for α and β which minimize the total absolute path difference for all ports.

$$|\delta P|_{\boldsymbol{Total}} = \sum_{1}^{M}\sum_{1}^{N}\left|\sqrt{\varepsilon_r}\,(l-h) + \sqrt{\varepsilon_e}\,W + y_3\sin\theta\right| \tag{2.6.11}$$

Moreover, ζ is bounded by an upper limit which varies with the focal ratio for a given focal angle as shown in *Figure 2.7.* This limit sets a constraint on α and β values during the optimization process. For specific acceptable path difference calculated using (2.6.11) and a given ζ_{max}, an appropriate range of α and β can be chosen from *Figure 2.7* [77]. However, the lens performance optimality is not obtained only from the phase error point of view. Amplitude performance, on the other hand, is also an important design factor that must be considered. Without providing both of phase error and amplitude performance together, the picture of BFN performance optimality is

somewhat incomplete. The performance of the Rotman lens in terms of the amplitude and the phase error is addressed shortly here and articulated in Chapter 4.

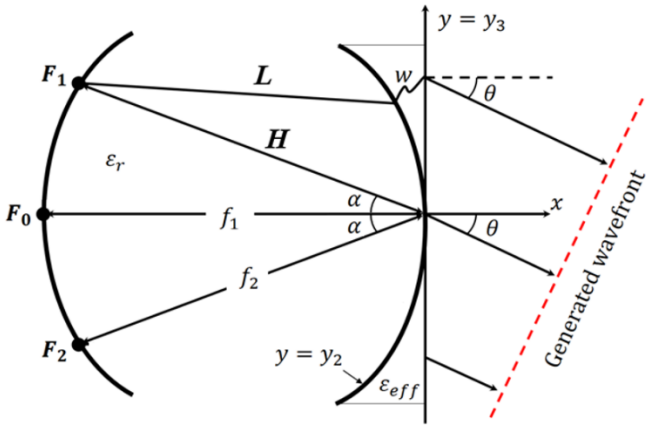

Figure 2.6: Hansen's Modified Rotman Lens.

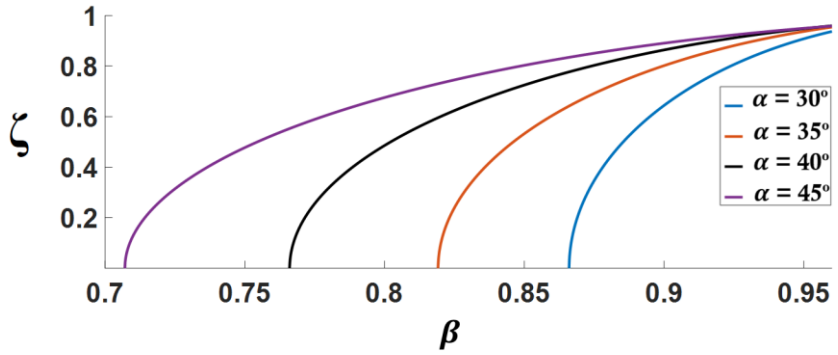

Figure 2.7: Variation of the upper limit on parameter ζ with the focal length for different focal angles.

The last essential parameters for designing Rotman lens are the normalized lengths ($W = w/f_1$) of the transmission lines connecting each array-port to the body of the lens. They are obtained by solving the following quadratic equation [77]:

$$aW^2 + bW + c = 0 \tag{2.6.12}$$

Where a, b, and c are functions in α, β, and ζ.

$$a = 1 - \frac{(1-\beta)^2}{(1-\beta\cos\alpha)^2} - \frac{\zeta^2}{\beta^2} \tag{2.6.13}$$

$$b = -2 + \frac{2\zeta^2}{\beta} + \frac{2(1-\beta)}{(1-\beta\cos\alpha)} - \frac{\zeta^2\sin^2\alpha(1-\beta)}{(1-\beta\cos\alpha)^2} \tag{2.6.14}$$

$$c = -\zeta^2 + \frac{\zeta^2\sin^2\alpha}{(1-\beta\cos\alpha)} - \frac{\zeta^4\sin^4\alpha}{4(1-\beta\cos\alpha)^2} \tag{2.6.15}$$

The phase centers of the corresponding array ports are obtained using Peter Simon formulation as follows [82]:

$$\frac{x_2}{f_1} = 1 - \frac{0.5\zeta^2 \sin^2\alpha + (1-\beta)\, w/f_1}{(1-\beta\cos\alpha)} \tag{2.6.16}$$

$$\frac{y_2}{f_1} = \zeta\,(1 - \frac{w}{\beta f_1}) \tag{2.6.17}$$

Similarly, for the phase centers of the beam ports:

$$\frac{x_1}{f_1} = \rho_0[1 - \cos(\acute{\alpha} + \phi)] \tag{2.6.18}$$

$$\frac{y_1}{f_1} = \rho_0 \sin(\acute{\alpha} + \phi) \tag{2.6.19}$$

$$\rho_0 = 1 - \frac{(1-\beta)^2}{2(1-\beta\cos\alpha)} \tag{2.6.20}$$

$$\acute{\alpha} = \sin^{-1}(\sin\theta/\gamma) \tag{2.6.21}$$

$$\phi = \sin^{-1}(\frac{1-\rho_0}{\rho_0}\sin\acute{\alpha}) \tag{2.6.22}$$

Once the phase center coordinates of all beam ports and array-ports are obtained, a horn of width about (λ/2) is created around each phase center [77]. The axis of the horn is normal to the port curve. These horns are tapered out of the lens parallel plate region, with a reasonable length, to provide a better impedance match between the feed and lens body. Otherwise, received wave will be transferred into higher order modes in the tapered region and cannot propagate through the feed, but will be reflected [83].

Finally, the side walls of Rotman lens are attached to *D* number of matched dummy ports to absorb the incoming wave on it and provide a reflection-less termination of the parallel-plate region. There is no specific number of dummy ports that should be selected for Rotman lens design, even in the original proposal of [81]. The vast majority of Rotman lens designs have multiple dummy ports, such as [66-70] and [73-75]. On the other hand, some Rotman lens designs adopt only a single dummy port in each side as reported in [71]. According to [84], the side walls curvature, and the dummy ports number and size have some impact on the side lobe level but no visible effect on the main beam. Therefore, dummy ports number, size, and position should be optimized to obtain an acceptable phase and amplitude performance, where they still contribute to the magnitude and phase variation at the array ports due to the multipath reflection. It should be

noted that some Rotman lens designs do not employ dummy ports and are replaced by absorbing material [15,85]. Also, because there is some energy lost to the dummy ports, [15] suggests a bed of nails technology to guide the waves instead of dummy ports for effective energy reuse.

The amplitude performance is approximated to estimate the amount of electromagnetic (EM) coupling between any two ports by applying aperture theory and uniform distribution to each port [82,86].

$$S_{ij} = j_o\left(kw_i \sin\phi_i\right) \times j_o\left(kw_j \sin\phi_j\right) \times \sqrt{\frac{w_i w_j}{\lambda d_{ij}}}\, e^{-j\left(k_r d_{ij} + k_e W + \frac{\pi}{4}\right)} \tag{2.6.23}$$

$$j_o(x) \equiv \sin(x)/x \tag{2.6.24}$$

where k_r and k_e are the phase constants in the parallel plate region and the transmission lines, to the array ports side, region respectively, d_{ij} is the distance between the port *i* and port *j* phase centers, w_i, w_j, are the port widths, and ϕ_i, ϕ_j are the angles between the normal to the port aperture and the line connecting the port phase centers.

2.6.4 Rotman Lens Design Methodology

The proposed optimum mm-wave analog beamforming network can be designed according to the following brief and simple designing steps:

1. Select *N* number of a typical antenna element that has broadband, a wide 3dB BW ($BW_{element}$), and gain performance satisfies the required total array gain.
2. Determine the maximum scanning range ($\pm\theta_0$), provided that $2\theta_0 \leq BW_{element}$ (of the maximum required frequency).
3. Calculate the minimum required number of Rotman lens beam ports (*M*) using (2.6.5) based on the required application. Note that increasing *M* increases the scanning accuracy. On the other hand, it increases the mutual coupling between ports.
4. Calculate the minimum required on-axis focal length (f_1).
5. Calculate the indirect factor of utility ζ using (2.6.9) by setting $y_3 = y_{max}$ and $\zeta = \zeta_{max}$.
6. Choose appropriate values of α and β that satisfy ζ_{max} from *Figure 2.7* as initial guess. Further optimization can be done using (2.6.11) and (2.6.23) to ensure optimum performance for both of phase and amplitude.

7. Calculate and plot the path difference for the range of $[-\zeta_{max}, \zeta_{max}]$ using (2.6.10) and (2.6.11). repeat 6 if the path difference exceeds specified maximum permissible limit or amplitude performance declines below a minimum specified level using (2.6.23).
8. Solve the quadratic equation (2.6.12) to obtain W.
9. Calculate the phase center coordinates for both beam and array ports as in [82].
10. Create a horn of width about ($\lambda/2$) around each phase center coordinate with an axis normal to the port curve.
11. Taper the horn, with a reasonable length, toward the feed.
12. Create D number of matched dummy ports at the two side walls of the lens. Otherwise, use absorbing material or guiding structure.

2.6.5 Soft and Hard Surfaces

Soft and hard surface boundaries are well known from acoustics. They are artificially made by corrugating a conducting surface with transverse corrugations (Soft or Stop surface), dielectric-filled longitudinal corrugations (Hard or Go surface), or loading a dielectric substrate with transverse (Soft or Stop surface) or longitudinal (Hard or Go surface) metallic strips [87,88]. The concept of the soft surface can be explained by the example of the corrugated circular horn antenna, which is where the corrugations make the field transverse components that are almost zero at the wall and equal to the value of the transversely tangential field component. This implies that the corrugated surface—referred to as *soft*—stops the electromagnetic wave propagation. One of the essential applications of a soft surface is providing side lobe reduction of antennas in any plan for any sort of polarization [88]. However, a hard boundary prevents the propagation of only the longitudinal field component and supports the propagation of the transverse fields, which is, of course, provided that the grooves are filled with dielectric material with permittivity larger than one [89]—thus, only TEM mode will propagate. RGW employs both soft and hard surfaces in which said surfaces act as periodic strips of PEC-PMC surface. What determines the wave propagation or suppression is the direction of the propagation with respect to the direction of the PEC-PMC surface, which is shown in *Figure 2.8* [88].

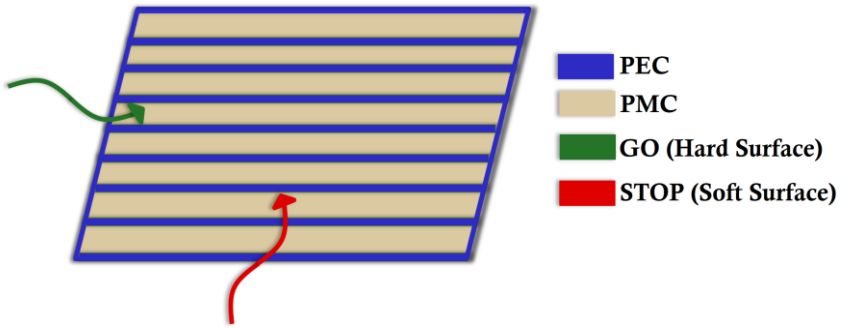

Figure 2.8: Soft and hard surfaces based on the direction of wave propagation.

2.6.6 Electromagnetic Band Gap

When electromagnetic waves interact with a periodic structure—referred to as Artificial impedance surface or *engineered electromagnetic surface*—it results in some interesting characteristics, which have several applications. The engineering of these surfaces involves altering the impedance boundary conditions of the surface of a structure and, thus, controlling the wave propagation characteristics. Initially, these descriptions began as Photonic Band-Gap (PBG) structures, which principally deal with types of structures and frequencies pertaining to optics. PBG structures are 1D, 2D, and 3D periodic structures—both dielectric and conducting—which manipulate the electromagnetic wave propagation as a means to not allow it to propagate within certain frequency ranges or band-gaps. The PBG designation was extended to include other types of structures and frequencies, such as Electromagnetic Band-Gap (EBG) structures. EBG structures control the frequency band (stop band, passband, band gaps) [90]. This is accomplished by altering the surface of a structure, by modifying its geometry, and/or adding other layers exactly as the soft and hard surface principle—but in 2D or 3D as opposed to 1D.

2.7 Summary

Millimeter wave fabrication technologies could place millimeter wave technology at the forefront of the new applications and services demanded by a wide range of users. Some of these technologies are characterized by ease, low-cost, and monolithic while others provide better performance with a higher cost or additional restrictions. PCB, LTCC, and SIW are well-known planar fabrication technologies. Recently, modern guiding structures such as RGW and its printed

version PRGW have been introduced to replace the traditional ones of high losses or low power handling. Besides, the advanced development of semiconductors allows RFIC and MEMSs mm-wave devices and antennas to reach a significant level of realization.

Generally, antennas are selected based on specific requirements for a mm-wave communication system include gain, matched impedance bandwidth, radiation type, and size of the structure. Quasi-Yagi antenna and planar dielectric lens antenna (DLA) are selected from these types of mm-wave antennas for advantages of low profile, lightweight, ease of fabrication and installation, high directivity, and high radiation efficiency to develop a new type of mm-wave antennas.

The beamforming network is an essential 5G requirement, where the signal blockage, for some cases, cannot be avoided using a direct route between two mm-wave transceivers. Therefore, BFN is used to re-route the signal in the desired direction. The selected BFN for this work is based on Hansen's procedure for designing Rotman lens.

CHAPTER 3: Quasi-Yagi Dielectric Lens Antenna

3.1 Introduction

In this chapter, a new type of planar antenna as a potential candidate for mm-wave wireless networks and 5G applications is presented. The proposed antenna is a combination between a Quasi-Yagi antenna and a planar dielectric lens. The proposed antenna design configuration is discussed in section 3.2, subsection 3.2.1, while subsection 3.2.2 explains the propagating modes in the DSW. Section 3.3. presents two variants of dielectric lenses along with the simulation results, parallel lines dielectric corrugation (PLDC) in subsection 3.3.1 and Ray combiner dielectric lens (RCDL) in subsection 3.3.2. The experimental results are provided in section 3.4 and finally the chapter summary is in 3.5.

3.2 Antenna Design Configuration and Analysis

3.2.1 Antenna Design Configuration

The proposed Quasi-Yagi antenna, basically, consists of two major parts as shown in *Figure 3.1*. The first part includes driver dipole, reflector, two-stage directors and, microstrip to slot line (MS-to-SL) transition structure and is located on the top layer of the substrate. On the bottom layer, a U-shaped MS-to-SL balun is placed to feed the driver dipole. This part works as an excitation source for the DSW, which is the second part of the antenna. The conventional rectangular driver of the printed Quasi-Yagi antenna has a narrower bandwidth compared to the tapered one, while the tapered driver has tilted edges with respect to the reflector. Therefore, the driver is tapered to improve the antenna bandwidth performance. The initial length of the driver dipole is selected to be around one effective wavelength (λ_{eff}) of the center of frequency in the desired frequency band, to increase the dipole directivity compared to half-wavelength dipole used in the ordinary Yagi-Uda antenna [91]. Furthermore, the antenna directivity is boosted by two stages of passive multi-directors closely spaced by 0.1 λ_{eff} between the first director and the driver and 0.142 λ_{eff} between the second stage of directors and the first stage. Another function of multi-directors is providing a good impedance matching for the antenna [59]. The closer spacing between the driver and the first director as well as between the two directors ensures maximum electromagnetic coupling due to

space wave and the substrate's surface wave [45]. About 0.25 λ_{eff} from the driving dipole, the microstrip ground plane is located and acts as a reflector with 1.34 λ_{eff} width. The antenna was designed to have an input impedance of 50 Ω and is connected to a microstrip line with w_f = 0.365mm (Z_0 = 50 Ω) followed by another microstrip line of w_p = 0.178mm width (Z_1 = 67 Ω). This impedance is selected initially to match the input impedance of the Quasi-Yagi array at the center of the driven element and is usually small. It is strongly influenced by the spacing between the reflector and the driver [91]. The last microstrip line is curved in U-shape to feed the driving dipole through an MS-to-SL transition, providing a single-ended-to-differential conversion with a wide bandwidth. The U-shaped MS-to-SL balun is optimized to achieve a good impedance matching. The directivity of the proposed Quasi-Yagi antenna is enhanced by extending the plain dielectric substrate as a dielectric lens. *Table 3.1* contains the design parameters of the proposed antenna.

Since the desired frequency band is 28-38 GHz, as candidate frequencies for 5G applications, the center frequency is selected around 34 GHz. Consequently, the antenna's gain stability is expected to vary ± 1 dB around the center frequency. However, simulation results show that the performance of the Quasi-Yagi antenna with a plain DSW lens is, dramatically, degraded as the DSW length increases as shown in *Figure 3.2*. The antenna gain is not achieved as expected and converges to the original gain of the planar Quasi-Yagi antenna without extended DSW lens.

3.2.2 Propagating Modes Analysis

The wave propagation characteristics in the extended DSW are investigated, as explained previously in chapter 2 (subsection 2.6.2) to understand the reason behind the dramatic gain decline. *Figure 3.3* shows that the dielectric attenuation level for all frequencies in the band is minor compared to the gain sharp drop when the frequency exceeds 32 GHz. Therefore, the propagating modes which could be supported by a thin DSW are analyzed. Then, 10.44 GHz, 20.87 GHz, and 31.31 GHz are the cutoff frequencies of the three first modes in the plain DSW, consequently, higher order modes (HOM) are expected to propagate with the fundamental TM_{10} mode. *Figure 3.4* confirms the above hypothesis where the magnetic field distribution of these modes indicates that TM_{10} , TM_{20} and TM_{30} are supported by the plain DSW. Nevertheless, the symmetry of the antenna structure prevents TM_{20} mode from propagation while TM_{30} mode is

expected to exist. It is well known that if there is no source of excitation for a certain mode in a waveguide, this mode won't propagate. However, the length of the printed dipole might be a design concern, where it might be a source of undesired propagating modes. When the dipole length exceeds one full wavelength, the current distribution on the two sides of the dipole starts to change its polarity [91]. The negative polarity current could excite undesired HOM (TM_{30}) which can be supported by the DSW. As the frequency increases, the dipole electrical length increases, therefore, the negative current polarity portion increases accordingly as shown in *Figure 3.5*. Some large canceling effects in the radiation pattern would be expected [34]. This could explain the dramatic gain declining in the upper operational band frequencies of the Quasi-Yagi antenna (32-38) GHz. The effect of HOM becomes worst as the length of the extended ordinary DSW increases, where it destructively interferes with the fundamental mode due to the total internal reflection (TIR), as well as, the increase of attenuation with length. It also justifies the shift in the maximum gain to the lower band frequencies which have low attenuation, and mainly, are below the cutoff frequency of TM_{30} HOM.

Table 3. 1: Dimensions of the Proposed Antenna

Parameter	(mm)	Parameter	(mm)	Parameter	(mm)
a	4.5	w_{d2}	1.05	G_{d2}	0.940
b	58.5	w_{rs}	0.15	r_h	0.500
w_f	0.235	L_{rs}	2.40	d_r	0.254
w_s	0.330	L_d	3.35	s_x	0.254
w_p	0.178	L_{d1}	2.05	s_z	0.254
w_d	0.924	L_{d2}	1.05		
w_{d1}	0.924	G_{d1}	0.26		

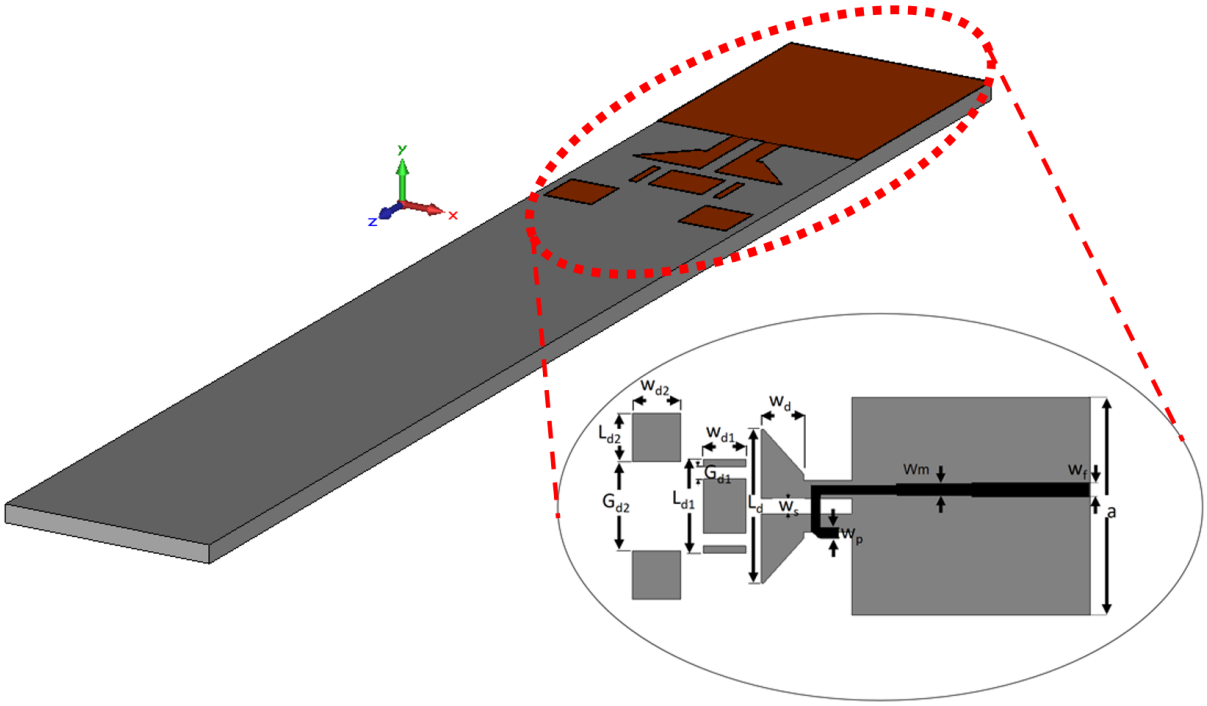

Figure 3.1: Planar Quasi-Yagi antenna with a plain DSW.

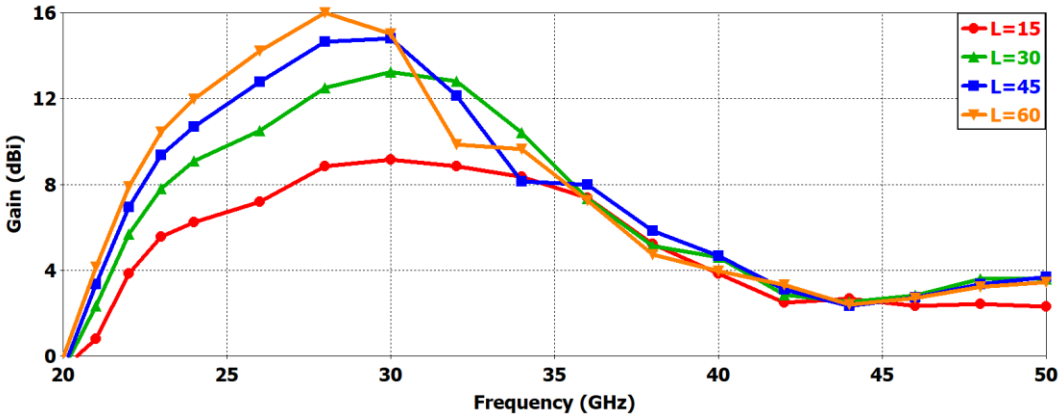

Figure 3.2: Quasi-Yagi antenna gain over frequency for different plain DSW lengths.

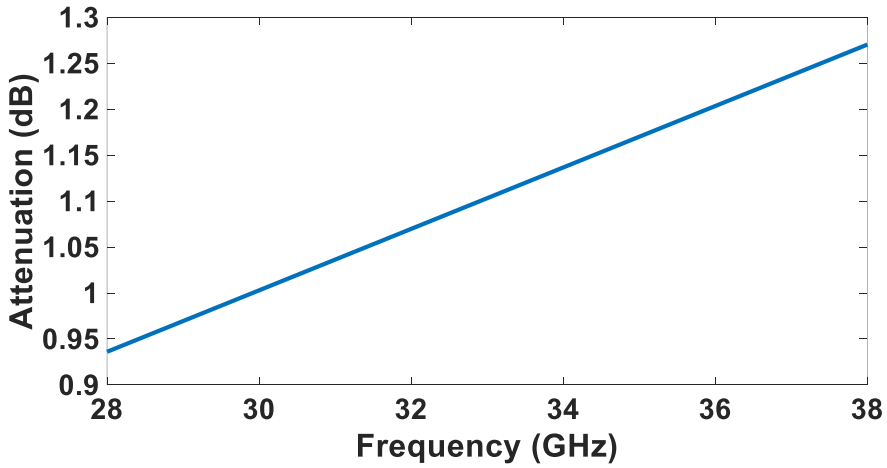

Figure 3.3: Attenuation over frequency for a plain DSW of 50 mm length.

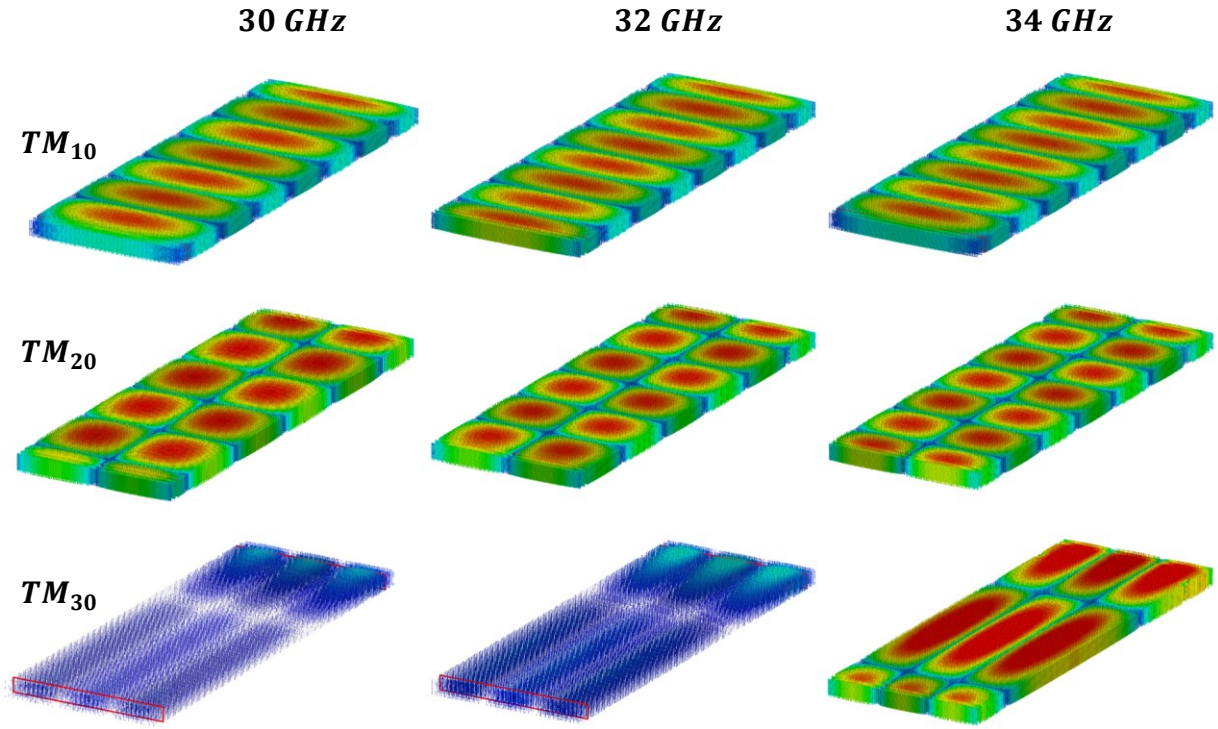

Figure 3.4: Magnetic field distribution in a plain DSW for different frequencies. TM_{20} can be supported but it won't be excited due to the antenna structure high symmetry.

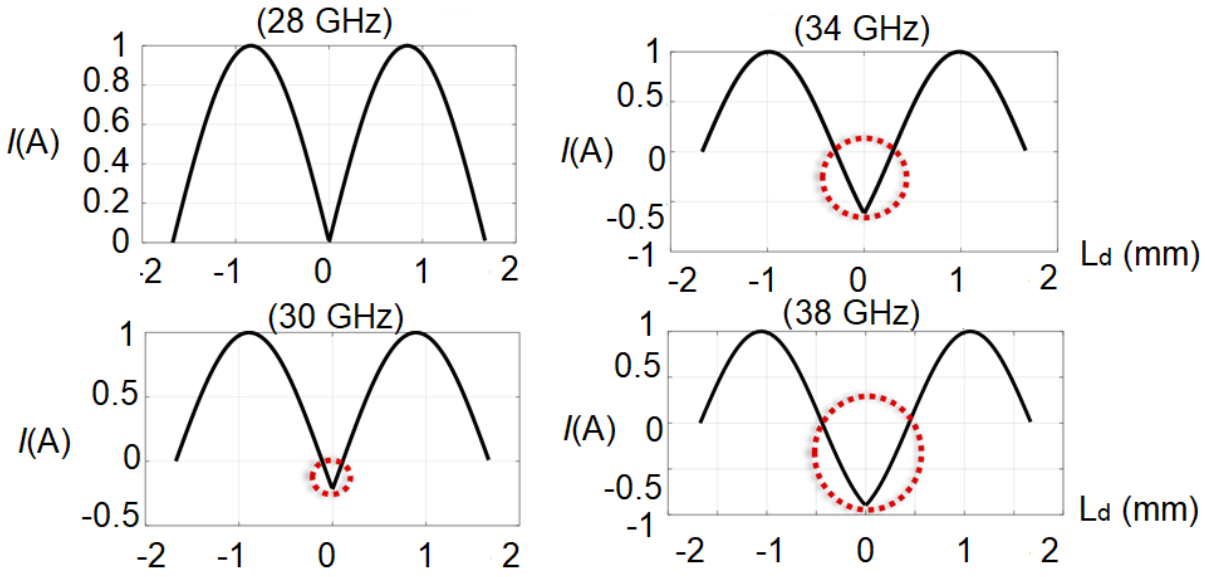

Figure 3.5: Current distribution on a finite length dipole with an opposite current polarity for different frequencies.

Since HOMs are undesired for their influence on the antenna performance, they should be suppressed. There are different techniques to avoid their propagation. One way is to limit the operational bandwidth to lower than lowest HOM cutoff frequency to avoid its propagation. In practice, 5% of the HOM cutoff frequency safety margin is usually recommended [79]. Though, this way results in a narrow bandwidth system. Another way is to limit the length of the dipole to one effective wavelength so that HOM excitation through opposite polarity current is prevented. However, this technique reduces the directivity of the finite length dipole and makes the antenna matching so difficult, where the input impedance, in this case, goes to infinity. Alternativly, perturbing the antenna structure by introducing, for example, rectangular corrugations or holes in the waveguide perpendicular to the propagation direction [92]. In other words, DSW's surface should be shaped to act as subwavelength gratings. This implies varying the surface homogeneity and hence reducing the effective dielectric constant of DSW. This technique implies, also, controlling DSW surface phase condition in a way allows the fundamental mode to propagate and suppress the undesired HOM as shown in *Figure 3.6* [93-95].

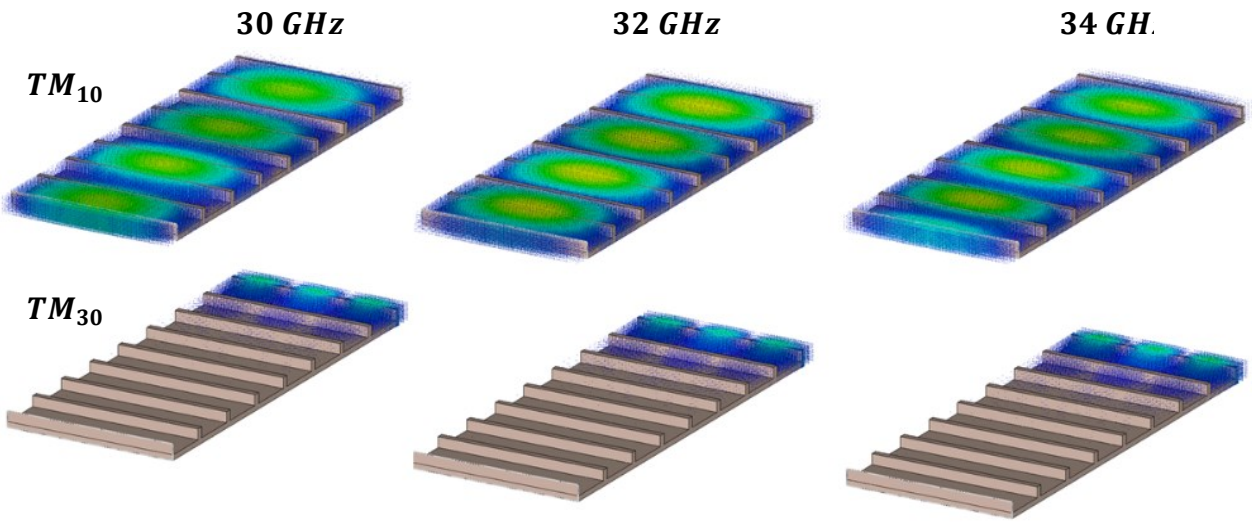

Figure 3.6: Magnetic field distribution in a corrugated DSW for different frequencies. TM_{10} is supported, while TM_{30} is suppressed in the corrugated DSW.

3.3 Simulation Results

3.3.1 Parallel Lines Dielectric Corrugation

Parallel lines Dielectric Corrugation (PLDC) is a corrugation in a dielectric substrate with a corrugation period, width and depth of d, w_c and L_c, respectively. *Figure 3.7* shows the PLDC geometry, which is, basically a ruled subwavelength grating but is used in the endfire direction.

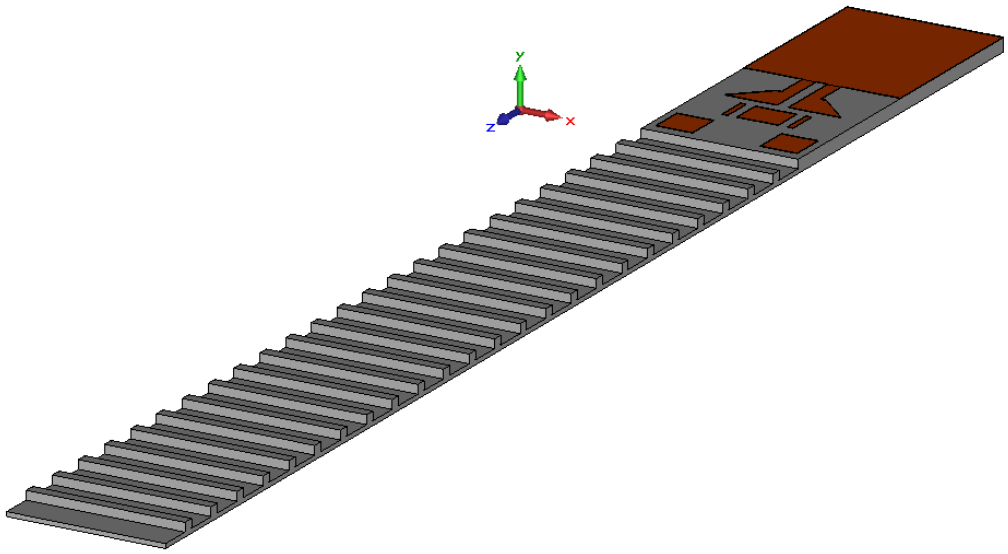

Figure 3.7: PLDC geometry as a ruled subwavelength grating.

For a high and stable gain with a broadband Quasi-Yagi dielectric lens antenna, free of HOMs, PLDC should be designed according to (2.6.1) and (2.6.2). The dielectric constant of the corrugated part of DSW is reduced from ε_r to ε_{eff}. Therefore, the cutoff frequencies of TM_{30} become out of the 30-38 GHz band. Moreover, the propagation characteristics are highly improved compared to the case of Quasi-Yagi antenna with a plain DSW as shown in *Figure 3.8a*. When the corrugation period is much less than the effective wavelength $(d \ll \lambda_0/\sqrt{\varepsilon_{eff}})$ of the maximum frequency in the band (i.e. 38 GHz), the gain is stable, where only the fundamental mode is propagating along the guiding structure to the end of corrugated DSW, providing the expected gain. It can be seen, also, in *Figure 3.8b* that the antenna has a good impedance matching (below -15dB) for all periods satisfy $(d \ll \lambda_0/\sqrt{\varepsilon_{eff}})$, but if the corrugation period becomes a significant fraction of the effective wavelength, then the DSW is no longer a homogeneous medium and the wave will be reflected and transmitted to the surrounding medium with a large portion is reflected to the antenna and the gain will sharply decline.

The corrugation width and depth control the gain and bandwidth of PLDC lens antenna. Considering the corrugating in DSW is a sort of spatial modulation, it is well known that a rectangular corrugation in the spatial domain is transformed into a sinc function in the frequency domain. When the corrugation cross-section area ($w_c.L_c$) increases, the gain increases consequently. On the other hand, the frequency bandwidth is inversely proportional to corrugation width w_c, analogous to a wide or narrow duration time domain pulse. So w_c should be optimized for maximum gain and frequency bandwidth. *Figure 3.9* depicts the gain and bandwidth variation with corrugation width. $w_c = 0$ means zero width corrugation ($f_w = 0$), the thickness of the entire corrugated DSW is reduced to (h-L_c), hence, the corrugation duty cycle ($f \approx (1 - f_h)$). An important notice regarding the gain controlling of PLDC, that the gain is not affected by the corrugation period by itself, provided that it is much smaller than the wavelength. In fact, the corrugation duty cycle controls the gain and the bandwidth of PLDC. The corrugation duty cycle controls, basically, the phase constant of the modes. *Figure 3.10* shows two cases for two different corrugation periods with the same duty cycle have identical gain. In other words, the corrugation duty cycle controls the propagation, the gain and the bandwidth of Quasi-Yagi antenna with PLDC lens. Radiation patterns of PLDC are compared to radiation patterns of an identical antenna with a plain substrate as shown in *Figure 3.11*.

PLDC has a better performance over the plain one in terms of suppressing the HOMs, especially, for high frequencies.

3.3.2 Ray Combiner Dielectric Lens

Ray Combiner Dielectric Lens (RCDL) is a dielectric lens with hybrid subwavelength gratings that works as a spatial modulator for a propagating wave in DSW. It can be designed using the same methodology as the PLDC, except that, it contains two types of subwavelength gratings, one and two-dimensional gratings as shown in *Figure 3.12*. A sequence of (L_{rs}×w_{rs}), d_r spaced rectangular slots is introduced perpendicular to the direction of the propagation to provide a smooth transition between the plain part of the DSW and the two-dimension circular holes' lattice of r_h radius with d_x and d_z sampling periods in *x* and *z* direction, respectively. For designing RCDL, d_x and d_z periods should satisfy $d \ll \lambda_0/\sqrt{\varepsilon_{eff}}$. An extraction model of the effective constant is illustrated in *Figure 3.13*. To validate the equivalent effective dielectric constant model, the Quasi-Yagi antenna with RCDL was simulated for three different combinations of hole radius and periodicity in z-direction selected from *Figure 3.13*, to have the same effective dielectric constant calculated by (2.6.3) and are compared to a Quasi-Yagi antenna with a holed part replaced by a plain dielectric slab of the same thickness and equivalent dielectric constant.

The simulation results depicted in *Figure 3.14* show that the performance of the proposed Quasi-Yagi antenna with RCDL, for the selected combinations, agree well with the performance of the equivalent model. As the hole radius increases, the effective dielectric constant decreases and consequently, HOMs are forced to be evanescent according to (2.6.2). By increasing the hole radius, the antenna impedance matching is improved as shown in *Figure 3.15a*, where only the fundamental mode is propagating. Though, *Figure 3.15b* shows that the hole radius is inversely proportion to the antenna gain. The hole radius should be optimized for a certain gain performance. In contrast, the increase of holing period leads to an effective dielectric constant increase. Therefore, HOMs would have real phase constant and start to interact distractively with the fundamental mode. This interaction deteriorates the antenna impedance matching as shown in *Figure 3.16a*, while the antenna has a good impedance matching for small holing periods where only the fundamental mode is propagating.

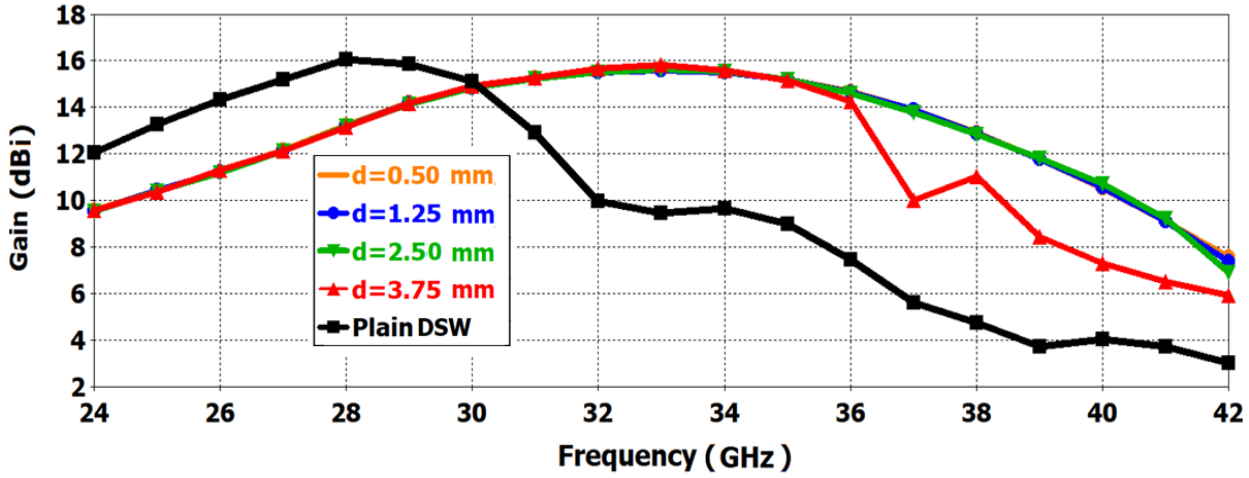

(a)

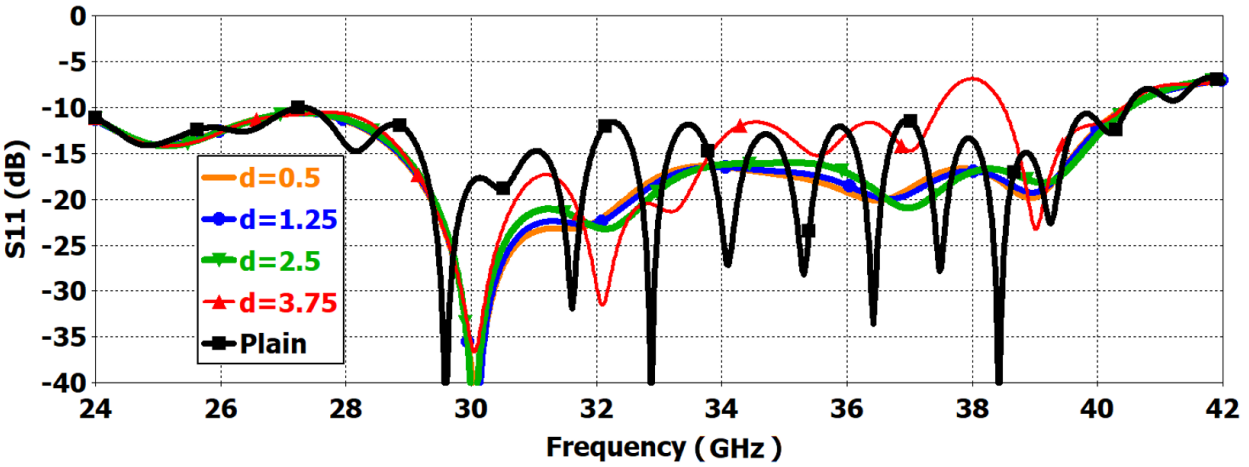

(b)

Figure 3.8: PLDC Performance variation with corrugation period: (a) Gain, (b) Reflection coefficient.

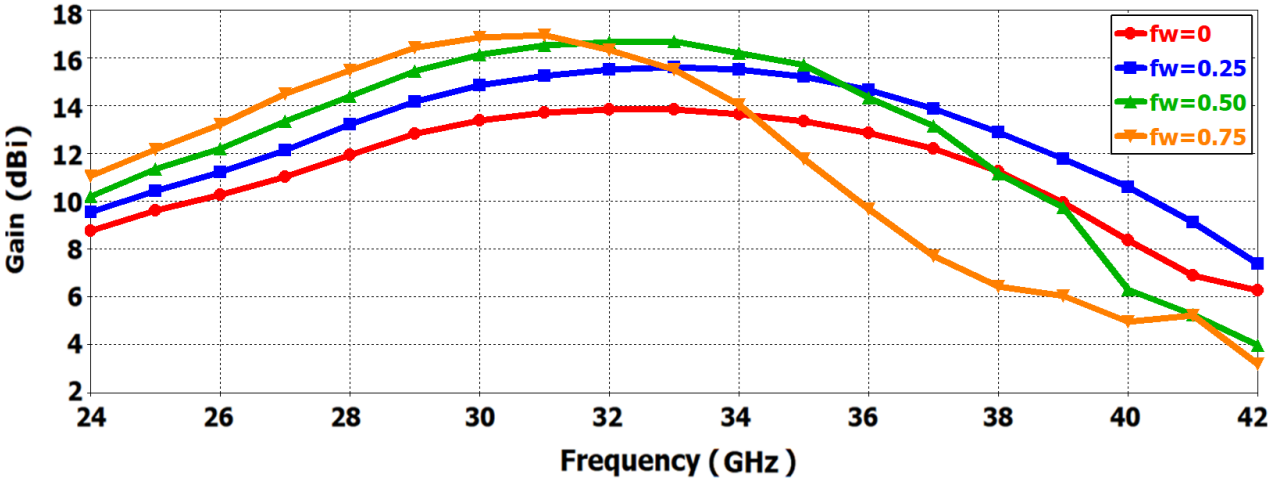

Figure 3.9: PLDC Gain and bandwidth variation with corrugation width.

As the period becomes a significant fraction of effective wavelength, RCDL becomes an inhomogeneous medium. In this case, the wave is transmitted to the surrounding medium with a large portion is reflected to the antenna (in the same manner explained in subsection 2.6.1 in the previous chapter) as shown in *Figure 3.16a*. Subsequently, the gain sharply declines as shown in *Figure 3.16b*. It can be seen from *Figure 3.17* that the total efficiency of the proposed RCDL Quasi-Yagi antenna is about 90 % within 30-34 GHz and decreases almost linearly along with increasing of the attenuation due to the loss tangent of the dielectric. Besides, the total efficiency of the RCDL Quasi-Yagi antenna is improved compared to that of the Quasi-Yagi with a plain DSW. Similarly, the simulation results show an aperture efficiency ranges from 95.6 % at 30 GHz to 54.7 % at 38 GHz. The simulated E-plane (E), H-plane (H), and cross-polarization (XPol) radiation patterns of the RCDL Quasi-Yagi antenna are illustrated in *Figure 3.18*, at 30 GHz, 34 GHz, and 38 GHz, respectively. The corresponding 3 dB beamwidth in E-plane and H-plane are around 32.6°, 28°, and 28°, respectively. Both E and H plane fields are symmetric with centered beam and almost have a similar 3 dB beamwidth. The simulation results show that RCDL highly improves the gain performance of the Quasi-Yagi antenna compared to the plain DSW lens and ranges between 14.7 to 15.8 dB. The side lobe level (SLL) is better than -15 dB for the band 30-34 GHz and better than -12 dB in the entire desired band. Moreover, the simulated cross-polarization level is about -29 dB within 3dB beamwidth in the entire 30-38 GHz band.

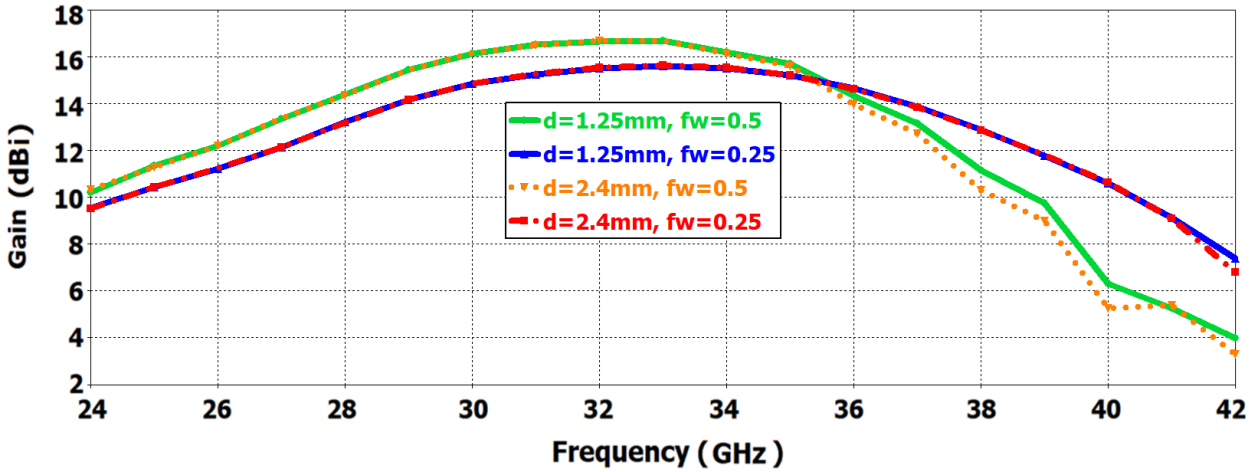

Figure 3.10: PLDC performance dependency on the corrugation Duty Cycle.

3.4 Prototyping and Experimental Results

To validate the proposed design methodology, one Quasi-Yagi antenna with perturbed substrate was fabricated and tested as shown in *Figure 3.19*. The antenna is 4.5mm by 58.5 mm size. The simulated and measured reflection coefficient of the antenna are shown in *Figure 3.20a*, while the gain is depicted in *Figure 3.20b*. The antenna impedance matching is below −15 dB over a wide frequency band with some peaks around -10 dB at higher frequencies due to fabrication oversizing as shown in *Figure 3.21*. The matching impedance bandwidth covers the band (24 – 40) GHz which is equivalent to 42% fractional bandwidth. The measured gain is about 14 to 15.2 dB over the band from 28 GHz to 38 GHz as shown in *Figure 3.20b*. The radiation pattern at frequencies from 30 to 38 GHz are shown in *Figure 3.22*. A Cross-polarization level is better than -22 dB within the 3dB beamwidth for the entire frequency band. It can be seen from *Figure 3.16, Figure 3.18*, *Figure 3.20* and *Figure 3.22* that the simulation results agree well with the measured results. Furthermore, the loss tangent, according to the substrate's datasheet, is 0.0023 at 10 GHz, but this value might be changed when the dielectric substrate is operated at 30-38 GHz and might result in additional losses. Besides, dielectric loss is inevitable decreases at higher frequencies. However, the measured results are quite encouraging taking into account the connector, cabling, and misalignment losses. The two-dimension circular holes' lattice in DSW lens improves the gain and the bandwidth performance of the proposed antenna system compared to plain DSW lens. Furthermore, the proposed antenna is compared to some relevant planar mm-wave antennas, such as Dielectric Lens antenna at 28.5 GHz, as well as, other Quasi-Yagi antennas at 3.3 GHz, 24 GHz, and 60 GHz. The performance of the proposed antenna is fairly better according to the reported results as summarized in Table 3.2.

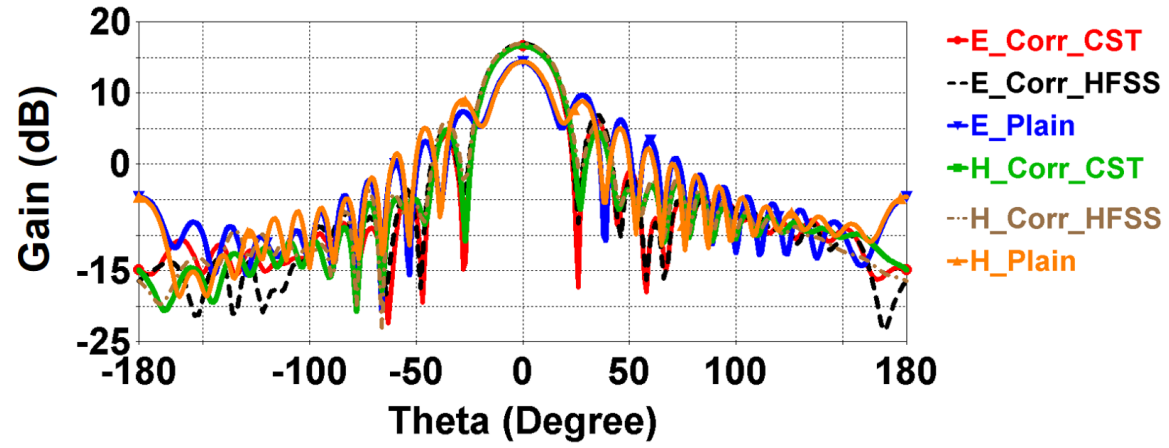

(a)

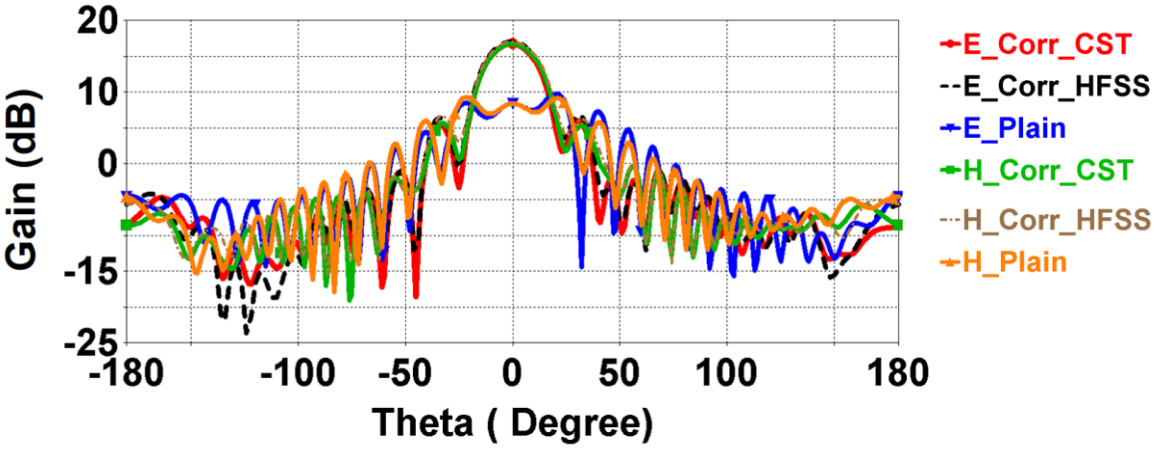

(b)

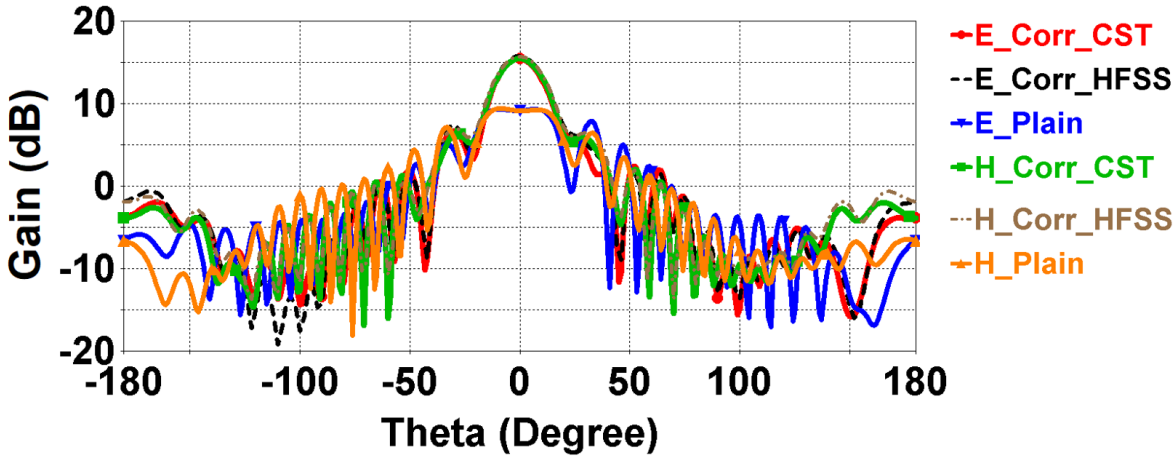

(c)

Figure 3.11: PLDC radiation patterns: (a) 30 GHz. (b) 32 GHz. (c) 34 GHz.

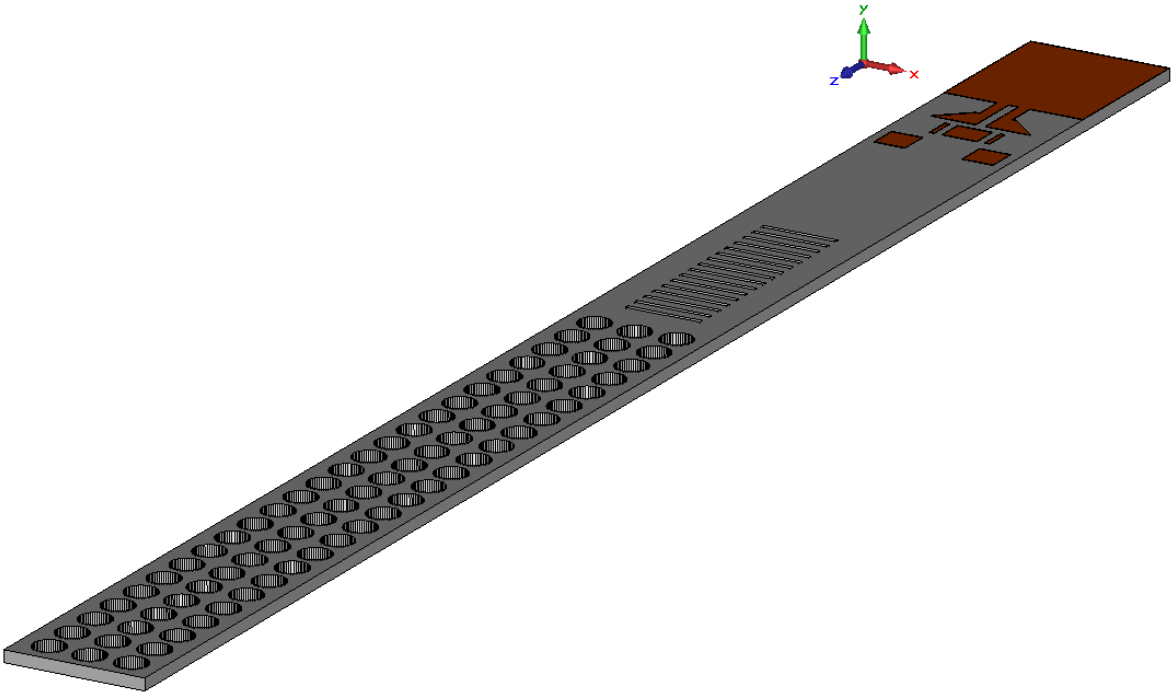

Figure 3.12: RCDL geometry as hybrid subwavelength gratings.

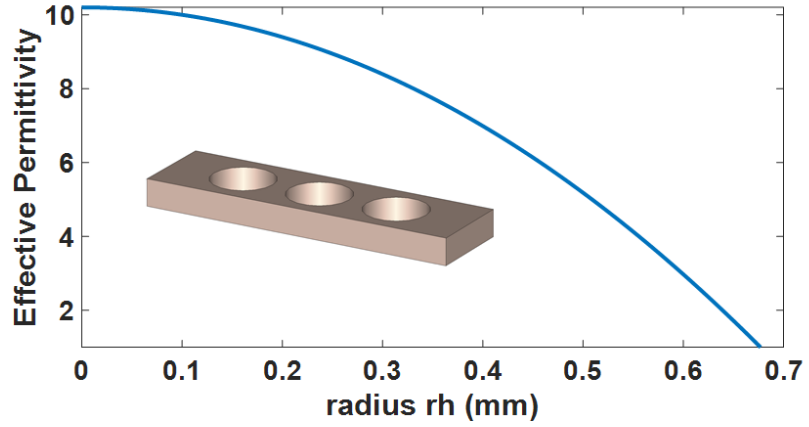

(a)

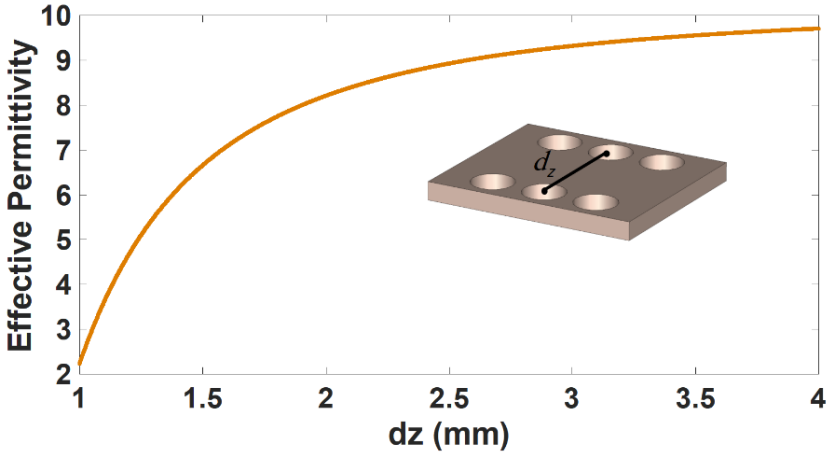

(b)

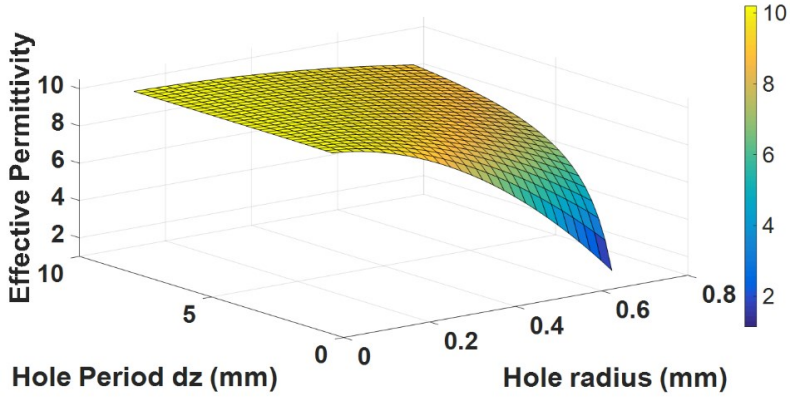

(c)

Figure 3.13: Effective dielectric constant of the holed substrate: (a) hole radius with fixed period of 1.25mm. (b) hole period with fixed radius of 0.5mm. (c) both of hole radius and period vary simultaneously.

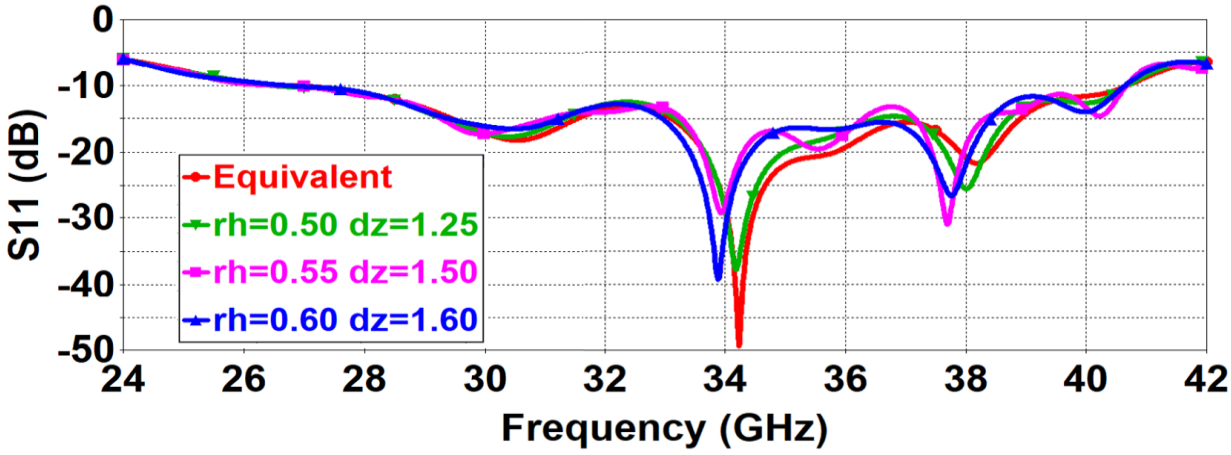

(a)

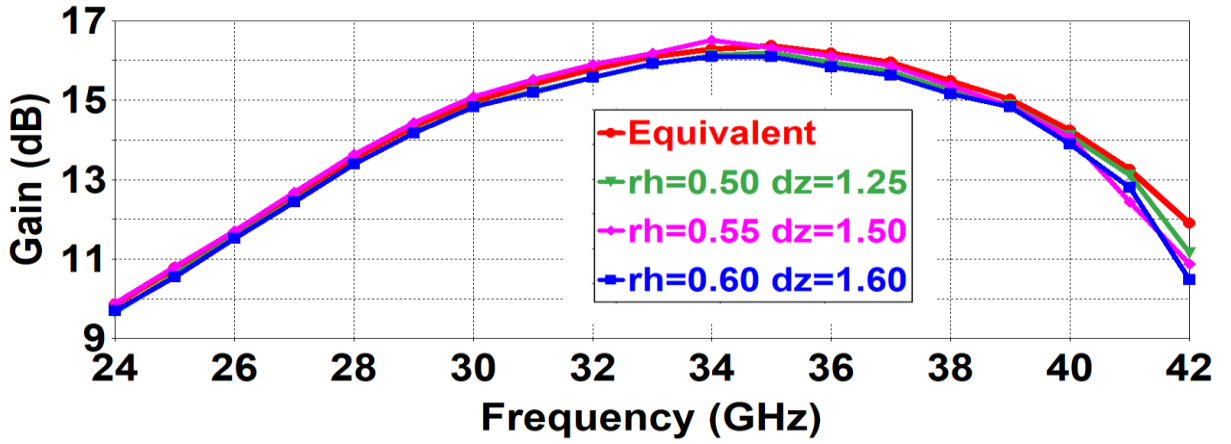

(b)

Figure 3.14: Simulated Quasi Yagi antenna with RCDL and equivalent models:
(a) Reflection coefficient. (b) Gain.

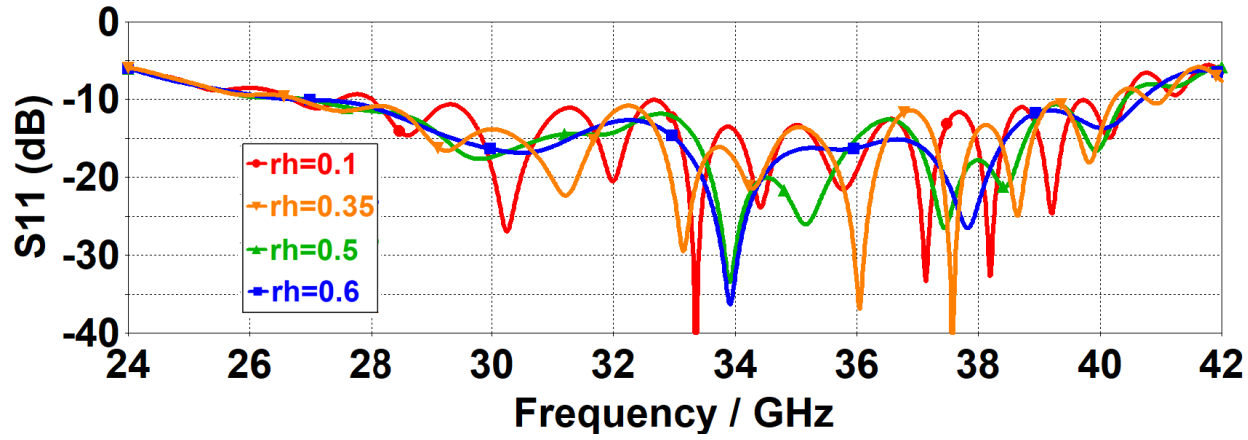

(a)

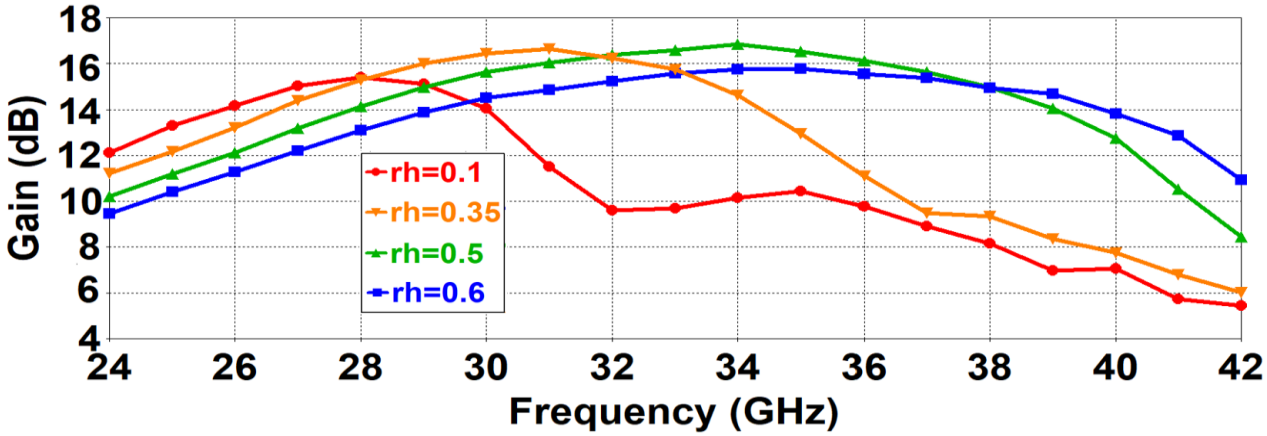

(b)

Figure 3.15: RCDL Performance variation with circular hole's radius: (a) Reflection coefficient, (b) Gain.

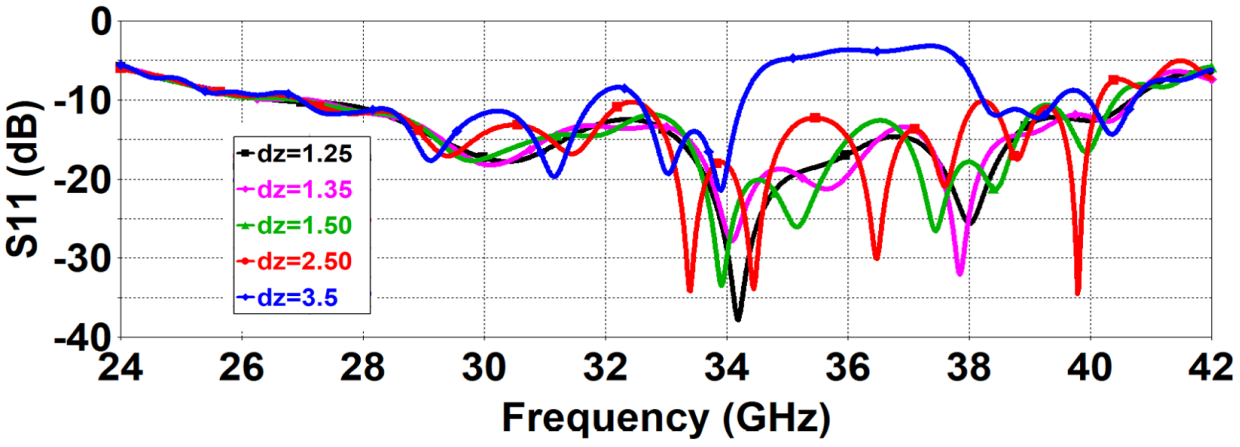

(a)

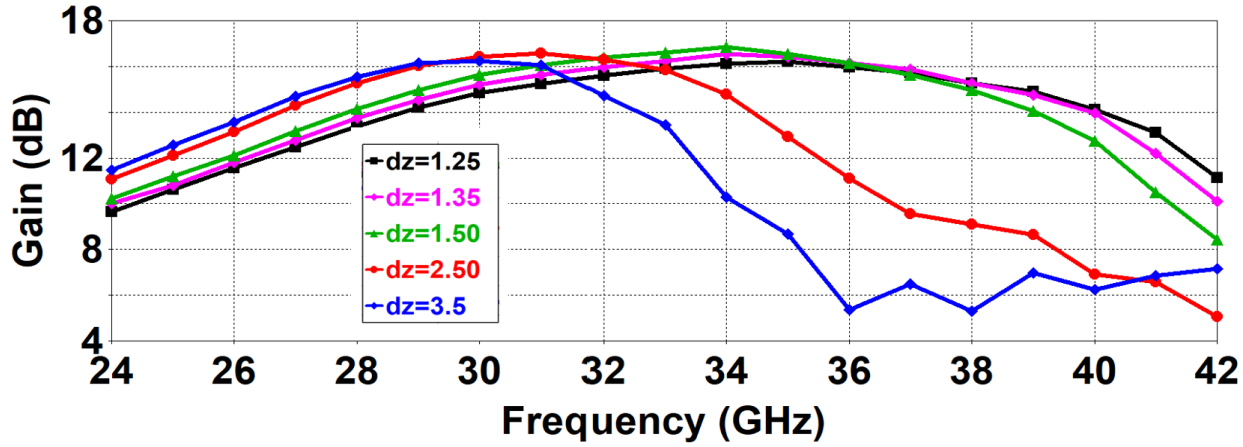

(b)

Figure 3.16: RCDL Performance variation with corrugation period: (a) Reflection coefficient, (b) Gain.

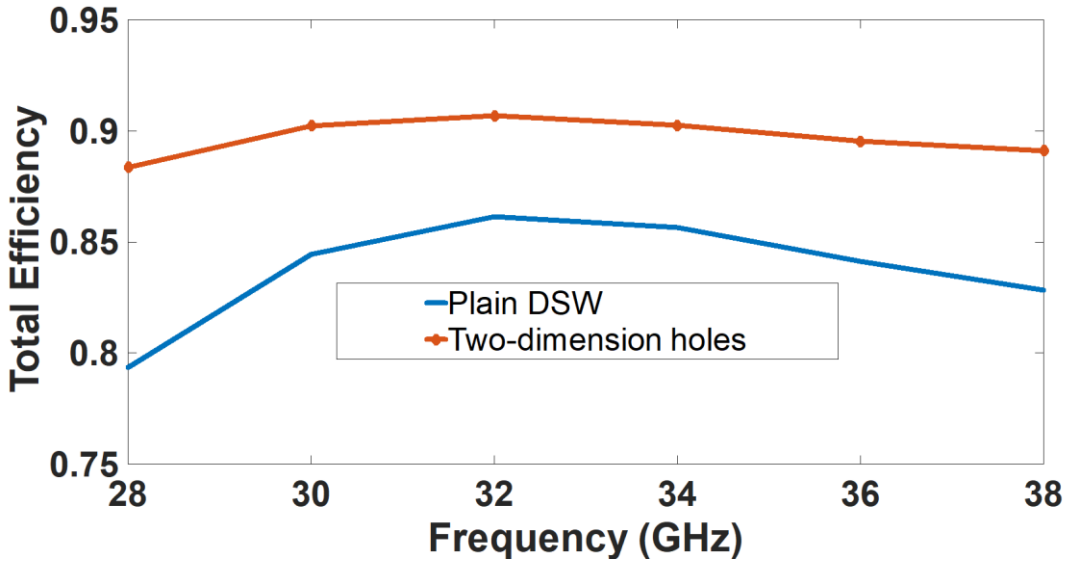

Figure 3.17: Simulation total efficiency of the Quasi-Yagi.

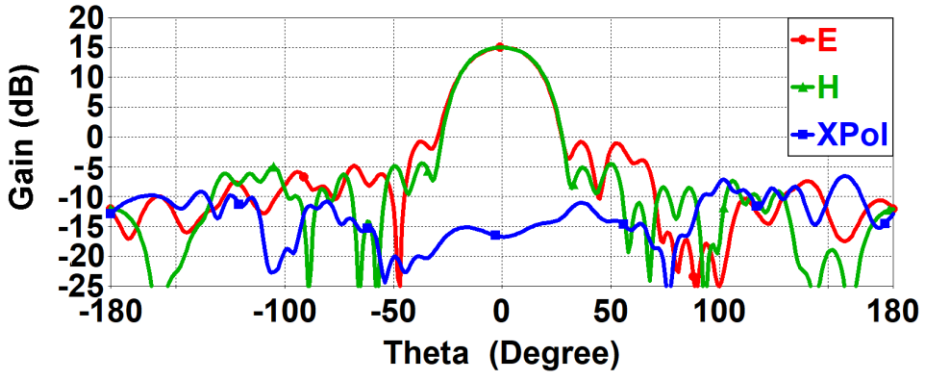

(a)

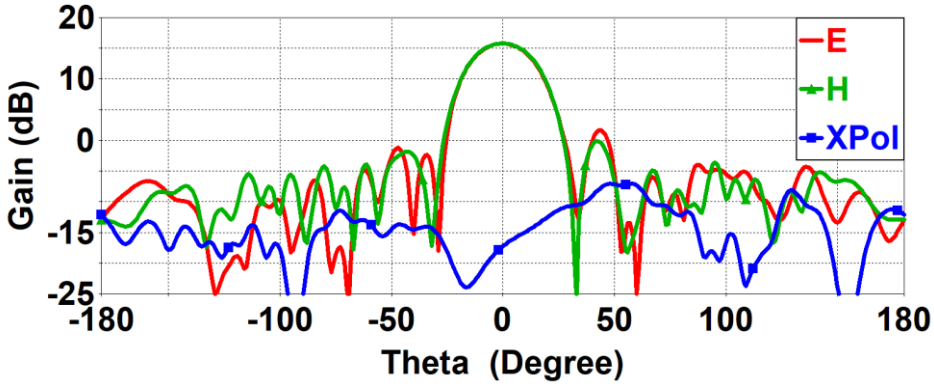

(b)

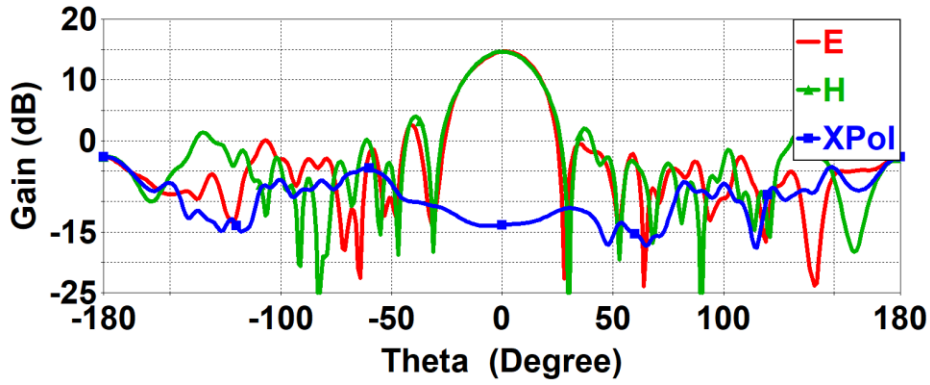

(c)

Figure 3.18: Simulation RCDL Quasi-Yagi antenna's radiation patterns: (a) 30 GHz. (b) 34 GHz. (c) 38 GHz.

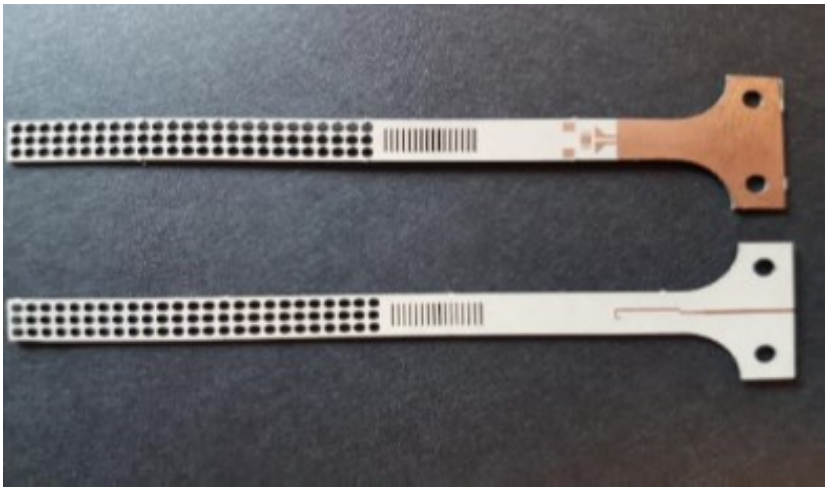

Figure 3.19: RCDL prototype.

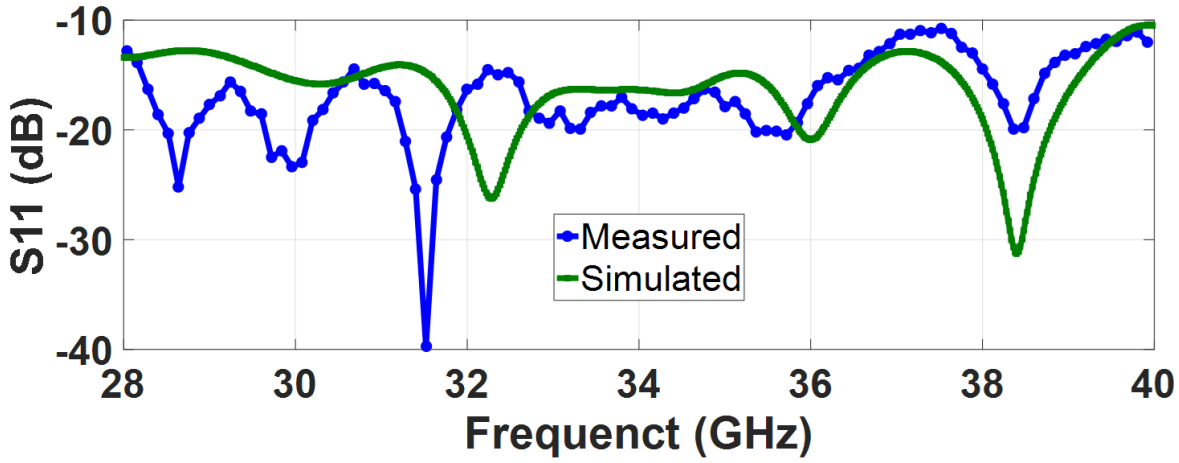

(a)

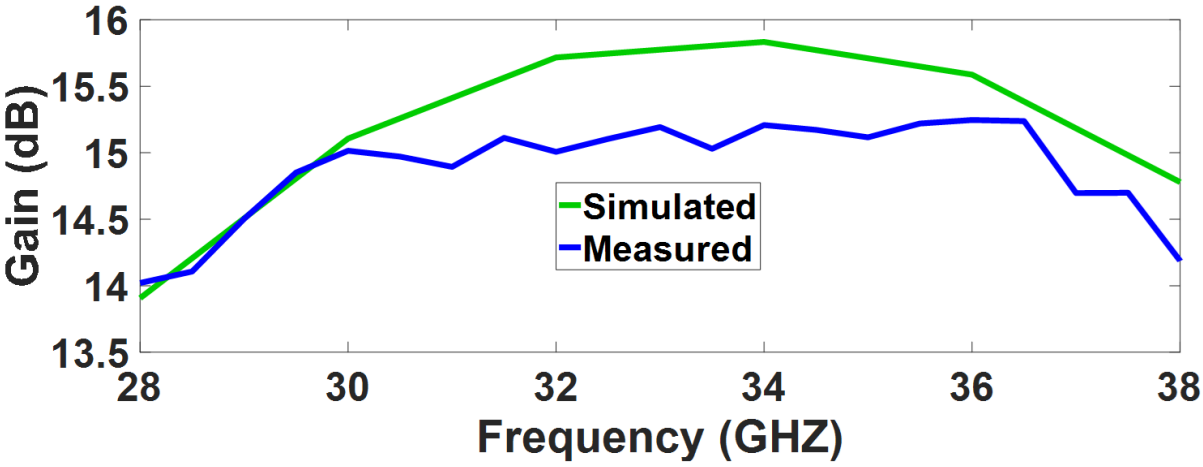

(b)

Figure 3.20: Measured and simulated RCDL Antenna Performance: (a) Reflection coefficient. (b) Gain.

Table 3. 2: **Comparison of the Proposed Quasi-Yagi Dielectric Lens with other related works.**

References	Excitation	Frequency GHz	FBR, dB	XPol. dB	Gain dBi	Efficiency %	Electrical Size mm^2
[46]	MS-fed	22-26	20@24 GHz	-16	10	90 @ 24 GHz	2.30 λ_0 × 3.3 λ_0
[56]	MS-Patch	1.84-4.59	>10	-16	9	83 @ 3.5 GHz	0.58 λ_0 × 1.1 λ_0
[59]	MS-to-SL	57-66	-	-15	11.7	-	1.84 λ_0 × 2.0 λ_0
[60]	Patch-fed	26-30	-	< -15	18.5	85 @ 28.5 GHz	11 λ_0 × 13 λ_0
This work	MS-to-SL	24-40	25@30 GHz	< -20	15	90 @ 30 GHz	0.45 λ_0 × 5.9 λ_0

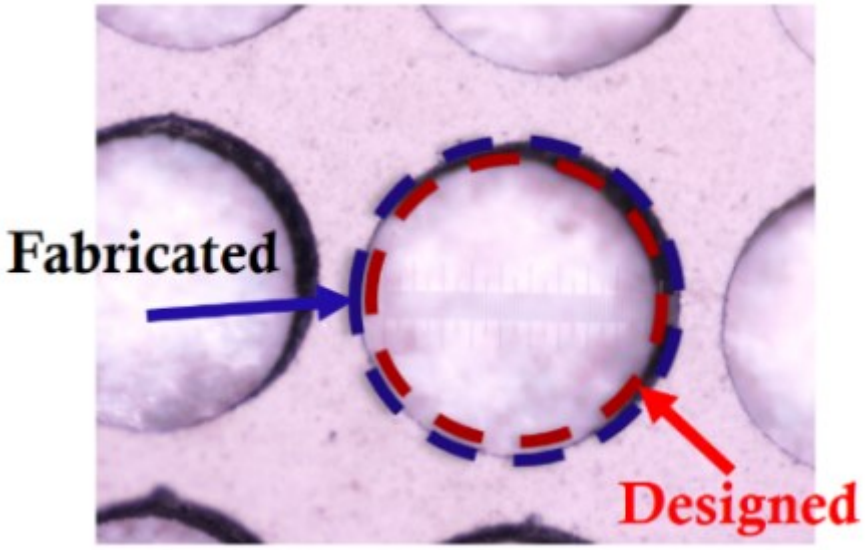

Figure 3.21: Fabrication oversizing.

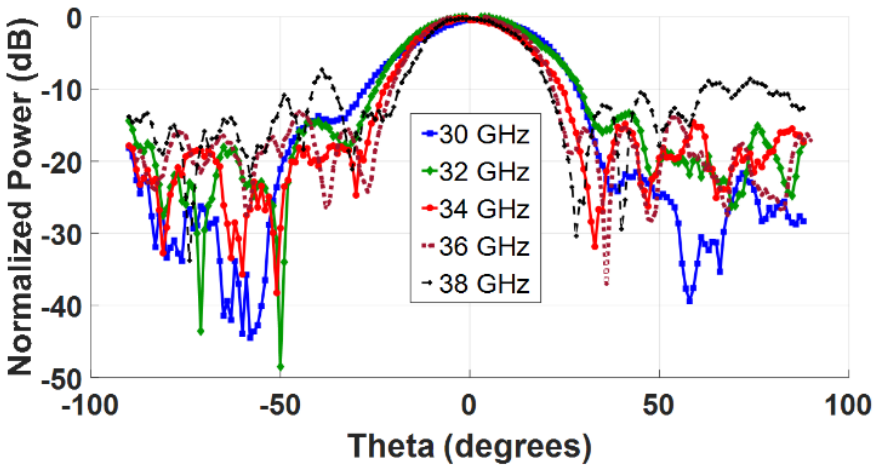

(a)

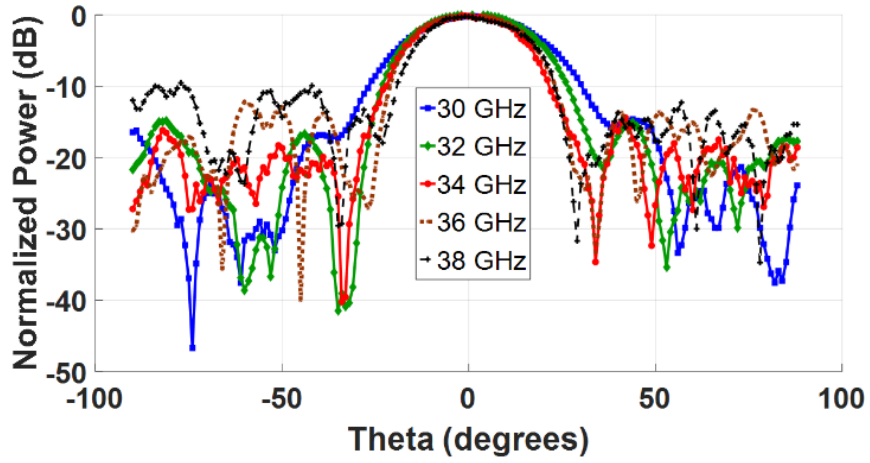

(b)

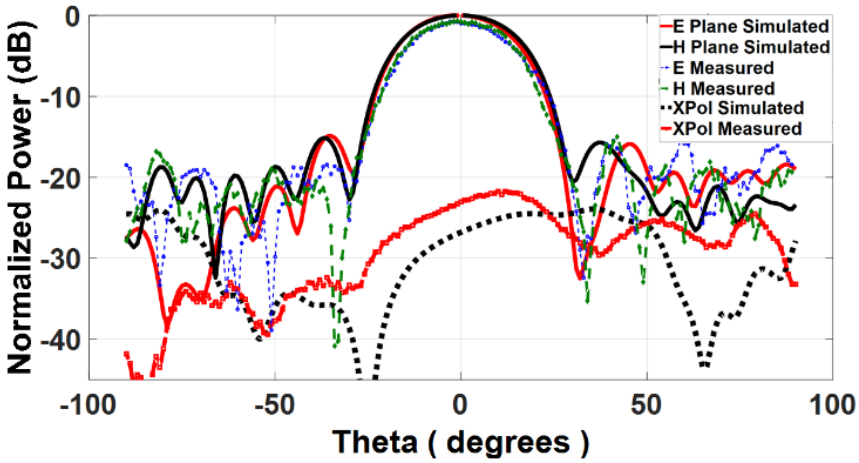

(c)

Figure 3.22: The radiation patterns of proposed RCDL: (a) Measured E plane. (b) Measured H plane. (c) Simulated and measured 34 GHz E, H and XPol.

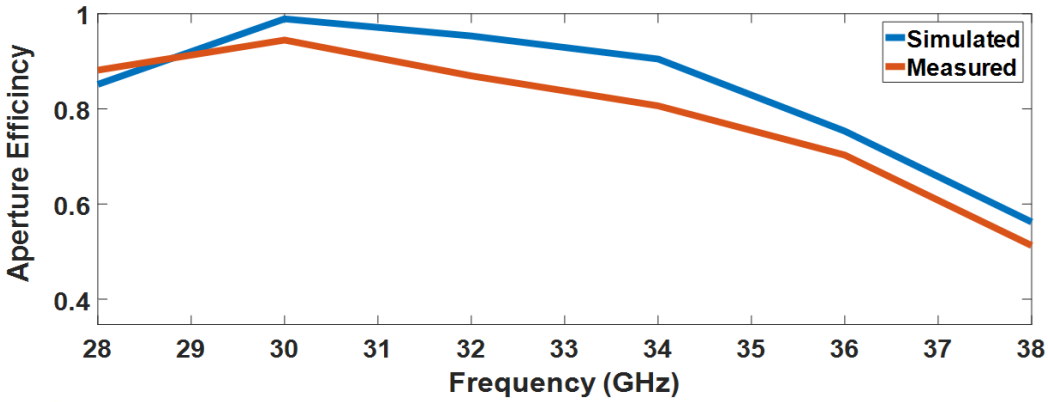

Figure 3.23: The aperture efficiency of the proposed Quasi-Yagi with RCDL.

3.5 Summary

A new millimeter-wave Quasi-Yagi antenna with a perturbed dielectric lens—based on subwavelength gratings and effective medium theories for gain enhancement, bandwidth broaden, and higher order mode suppression—is presented. The proposed design methodology is validated by the designed, fabricated, and measured antenna. The experimental prototype results show that, compared to the ordinary DSW lens, the gain of the proposed antenna has been improved. The proposed antenna exhibits a good impedance matching that is better than -10 dB in the band, which is 24–40 GHz more than 17 GHz (42 % FBW). The measured cross-polarization level is also better than -22 dB. The antenna measured gain ranges between 14 to 15.2 dB over the operating frequency band 30–38 GHz. Therefore, this antenna can be considered as a competitive planar high gain antenna for 5G applications. It can be scaled to 60, 77, or 94GHz for 5G wireless point-to-point, point-to-multipoint backhaul communication systems as well as automotive radar.

CHAPTER 4: Rotman Lens-bsed Analog Beamforming

4.1 Introduction

Beamforming is a method of using an array of antennas—that each have a shifting phase and amplitude—to precisely focus a signal toward a specific angular direction, which is accomplished whilst ignoring interfering signals that come from other directions. It is, essentially, used for mm-wave band to overcome two main problems: blockage by objects and signal attenuation over long distances. Furthermore, the propagation environment at mm-wave frequencies lends itself to a beamforming structure, which is where antenna arrays are required to obtain the necessary link budget [96].

In this chapter, seven-beam ports Rotman lens feeding eight Quasi-Yagi antenna array is implemented in the PCB technology. The proposed lens was designed to operate in the frequency band of 26–40 GHz. The lens was designed according to Hansen's design procedure for optimum Rotman lens parameters, and with a maximum gain and minimum phase error [77]. The proposed work addresses both the amplitude and the phase error performance while, at the same time, determining the design parameters of the proposed Rotman lens. The performance of the proposed BFN is compared to related beamforming networks with different fabrication technologies, and it exhibits a relatively high gain, broadband, and reasonable scanning performance, which is in addition to being of a low-cost and low profile in terms of MMIC compatible.

The rest of the chapter is organized as follows. Section 4.2 discusses the beamforming network design configuration of Rotman lens based on Hansen's modification of original Rotman and Tuner equations. Section 4.3 shows the simulation results of the proposed BFN. A prototype of the proposed BFN along with its measured results and discussion are presented in Section 4.4. Lastly, the summary is presented in Section 4.5.

4.2 Beamforming Network Design Configuration and Analysis

Rotman lens was invented in 1963 by W. Rotman and R.F. Turner [81]. Afterward, several methods were proposed as a means of improving the performance of Rotman lens, which were based on modifying the lens geometry or using optimization methods, (e.g., [77,80,82,97]). Hansen's modification of Rotman lens is adopted in this work. The design configuration and

analysis of the proposed Rotman lens is explained in subsection 4.2.1, while, subsection 4.2.2 discusses the configuration of a single antenna element used for the BFN.

4.2.1 Rotman Lens Design Configuration and Analysis

The proposed BFN was designed with eight array ports ($N = 8$), as shown in *Figure 4.1*. The original design requires seven beam port ($M = 7$), to steer the beam within a maximum scan angle of ± 40º, and minimum array element spacing of $0.5\lambda_0$. If Rotman lens was designed with beam ports less than M, the generated beams will not overlap within 3 dB BW of the resultant array pattern, and, hence, there would be a signal drop while the steering process. However, some applications—such as satellite communications—require no overlapping between the generated beams within 3 dB BW. In this case, the system is described as a multi-beam rather than a beamforming network, for it can still generate beams pointing in different directions, but overlap beyond 3 dB BW [70,71,86].

A minimum on-axis focal length of $4.5\lambda_0$ is calculated using (2.6.6). Therefore, f_1 is set to be $5\lambda_0$. Consequently, ζ is calculated using (2.6.9). The proposed Rotman lens was fabricated on a dielectric substrate with a permittivity of ($\varepsilon_r = 10.2$), thus, all dimensions of the lens are reduced by a factor of $\sqrt{\varepsilon_r}$ [80].

Since the main objective is to minimize both of the variations in the amplitude of the array-ports and the variation in the phase difference between adjacent array-ports, α and β are carefully chosen by repeating the steps 6 and 7 of the design methodology in subsection 2.6.4. To explain the effect of α and β on the phase and amplitude performance of a Rotman lens design, provided that all other parameters remain unchanged, three different α-β pairs are selected. Accordingly, the path difference and the amplitude variation are calculated for each α-β pair. *Figure 4.2* shows the path difference for three different α-β pairs at the center frequency. Based on (2.6.11), the total absolute path difference of $\alpha = 35°$ and $\beta = 0.875$, shown in *Figure 4.2a*, is 0.7994, increases to 0.9318 for $\alpha = 35°$ and $\beta = 0.92$, displayed in *Figure 4.2b*, and even more in case of $\alpha = 40°$ and $\beta = 0.92$, depicted in *Figure 4.2c*. However, the path difference minimization does not reflect the whole performance of the BFN, where the amplitude performance shown in *Figure 4.2d* indicates that about 4.363 dB amplitude variation between the center beam and the outer one in case of $\alpha = 35°$, $\beta = 0.875$, which is relatively high. This variation is improved to 2.243 dB in case of $\alpha = 35°$ and $\beta = 0.92$, and even better for $\alpha = 40°$ and $\beta = 0.92$ with only 1.754 dB of amplitude variation. In other

words, Rotman lens designer should satisfy, for typical applications, a reasonable phase error, and amplitude performance together. *Table 4.1* summarizes the amplitude and the total path difference performance for the three α-β pairs.

The last major part of the Rotman lens design is the transmission lines which adjust the phase of each array-port and are calculated using $(2.6.12 - 2.6.22)$. To have equal length transmission lines, so that the system is frequency independent, additional space between the lens array-ports and the array antenna elements is necessary.

Finally, each sidewall of Rotman lens parallel plat region is attached to one dummy port horn, which has a wide aperture that assembles having multiple dummy ports at the sidewall; this also reduces the number of the dummy loads needed for terminating the side walls of the parallel plate region.

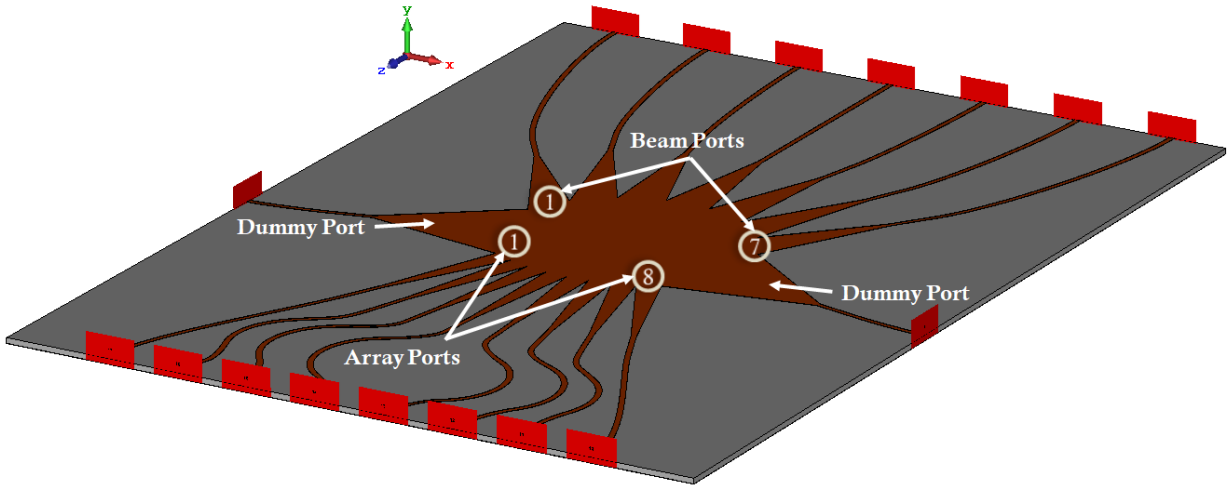

Figure 4.1: Simulated 7×8×2 Rotman lens design.

Table 4. 1: Path difference and amplitude performance comparison for three α-β pairs.

α	β	Total Path difference $\lvert\delta P\rvert_{Total}$	Amplitude Variation (dB)
35°	0.875	0.7994	4.363
35°	0.920	0.9318	2.243
40°	0.920	1.2092	1.754

Other parameters are set to be $\gamma = 1$, $f_1/\lambda = 4$, and $\theta_0 = 45°$

4.2.2 Antenna Design Configuration

The single antenna element of the proposed BFN is a Quasi-Yagi antenna of [J1]. Unlike the narrowband microstrip patch antenna, this type of antennas provides ultra-wideband that makes it a good selection for TTD beamforming networks. The selected Quasi-Yagi antenna with its dielectric lens follows the endfire radiation antennas' family. Likewise, Vivaldi antenna own ultra-wideband and the endfire radiation. Vivaldi antenna has wider *BW* and broader frequency band than Quasi-Yagi antenna. However, Quasi-Yagi antenna provides higher gain, more compact size, and lighter weight than Vivaldi antenna [98]. Another advantage of the endfire antennas that makes them suitable for planar Rotman lens-based BFNs is that their main radiation is less affected by the unwanted radiations, emitted by twisted transmission lines of the array or beam port sides than the broadside antennas, especially at mm-wave frequency band. Since one of our main objectives in this chapter is to design a compact size BFN, Quasi-Yagi antenna is selected for its compact size, low profile and light-weight in addition to its ultra-wideband.

4.3 Simulation Results

Following the calculation and parametric optimization of the lens parameters (as discussed in section 4.2), the analog beamforming network was designed with the parameters specified in *Table 4.2*. The performance of the beamforming network is evaluated for the single antenna element, lens structure, and the overall integrated beamforming network as follows.

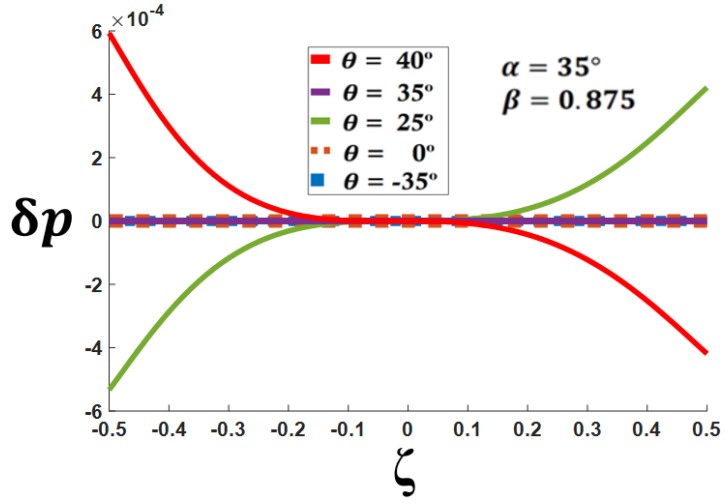
×10^-4
δp
ζ
θ = 40°
θ = 35°
θ = 25°
θ = 0°
θ = -35°
α = 35°
β = 0.875

(a)

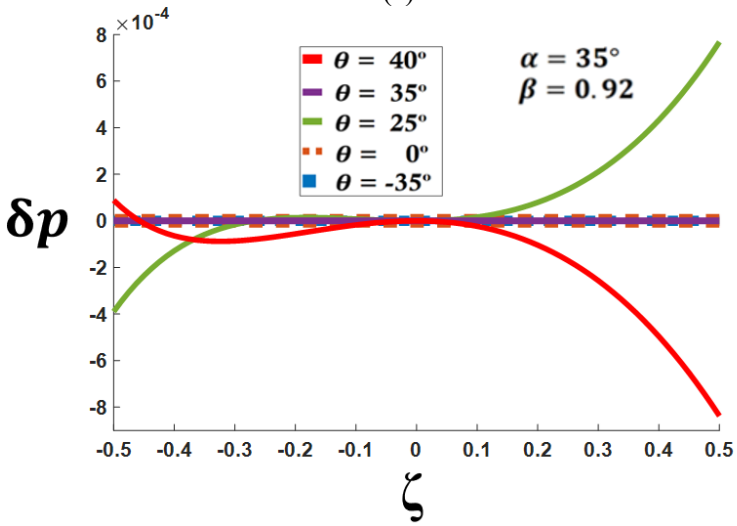
×10^-4
δp
ζ
θ = 40°
θ = 35°
θ = 25°
θ = 0°
θ = -35°
α = 35°
β = 0.92

(b)

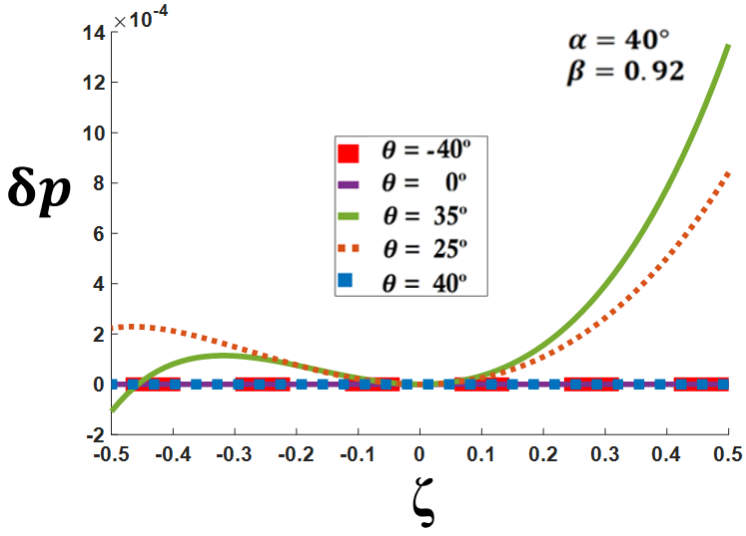
×10^-4
δp
ζ
θ = -40°
θ = 0°
θ = 35°
θ = 25°
θ = 40°
α = 40°
β = 0.92

(c)

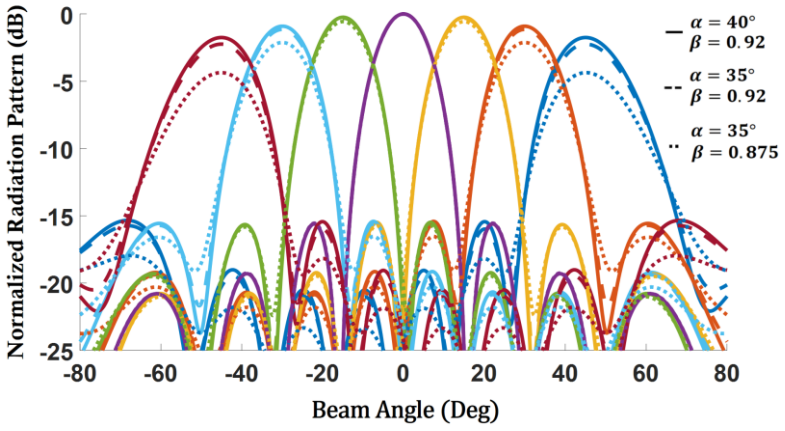

(d)

Figure 4.2: Path difference and amplitude performance for different α-β pairs : (a) . $\alpha = 35°$, $\beta = 0.875$, and $\theta_0 = 45°$. (b) $\alpha = 35°$ and $\beta = 0.92$. (c) $\alpha = 40°$ and $\beta = 0.92$. (d) Normalized radiation patterns for three different α-β pairs. The rest of parameters are ($\gamma = 1$, $f_1/\lambda = 4$, and $\theta_0 = 45°$).

4.3.1 Single Element

Quasi-Yagi antenna of [J1] was designed with lower gain for broader 3dB beamwidth performance so that it allows a wide scanning range. As shown in *Figure 4.3a*, the single element of Quasi-Yagi antenna exhibits broadband of (26-40) GHz. The antenna shows an average gain of 7 dBi and *BW* better than (>83º) in the band (26-34) GHz and gradually decreases to 70º for (34-40) GHz, which is normal due to the larger aperture with respect to operating wavelength as shown in *Figure 4.3b*. This is reflected on the absence of the 3 dB *BW* overlap beyond 34 GHz.

4.3.2 Rotman Lens

The simulation results indicate good impedance matching for the proposed lens, where reflection coefficients of all beam ports, as illustrated in *Figure 4.4a*, are better than −13 dB. The ideal average power level at the eight element array-ports fed by the center beam port, in the absence of material losses, is about -9 dB for each port. However, the selection of, relatively, high dielectric material with high tangential loss ($\tan\delta = 0.0023$) results in a dielectric loss, in addition to metallic and other types of loss.

Table 4. 2: **Main Parameters of the proposed PCB Rotman lens.**

Parameter	Symbol	Value
On-axis focal length	f_1	$5\lambda_0$
Focal angle	α	40°
Focal ratio	β	0.9
Expansion Factor	γ	1
Scanning range	$\pm\theta_0$	±40°
Number of Array-ports	N	8
Number of Beam ports	M	7
Number of Dummy-ports	D	2
Substrate thickness	h	0.381 mm
Total Lens length	l	70.00 mm
Total Lens width	w	50.00 mm
dielectric constant	ε_r	10.2

Also, there is a modest amplitude tapering experienced by array-ports, due to different distances from beam port. The tapering effect increases when feeding from the edge beam port. All these effects contribute to power level reduction. Consequently, the BFN's gain decreases compared to the gain of ideal N element, uniformly excited and equally spaced linear array. The relative total transmitted power accounts for all types of loss and is calculated using the simulated S-parameter of all array-ports fed by each beam port as follows [70]

$$P_j = \sum_{i=1}^{N} \left|S_{ij}\right|^2 \quad , j = 1, 2, \dots M \tag{4.3.1}$$

The proposed BFN has good S-parameters magnitude at the array-ports, with a relative transmitted power level ranges between -1.5 dB to -2.9 dB over 26-40 GHz as shown in *Figure 4.4b*. The rest of the ports are not reported for symmetry reason. These levels indicate an efficiency above 71% for the center beam port, 60.3% for beam port 3, 55% for beam port 2, and 51.3% for beam port 1. These losses are expected as discussed and increase unavoidably with the increase of the

scanning angle, especially, at higher frequencies. However, the lens size is significantly reduced compared to air-filled or low dielectric material Rotman lens design as shown in *Figure 4.5*.

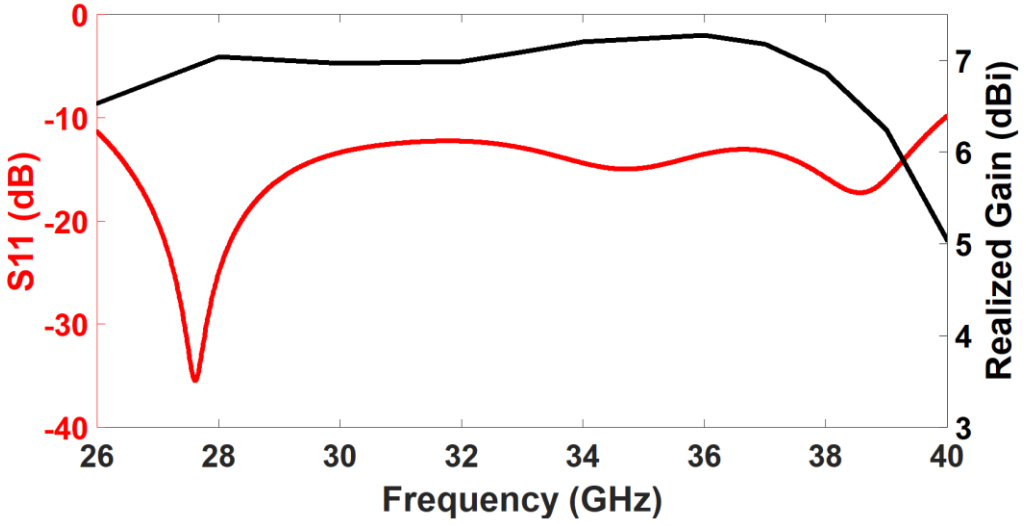

(a)

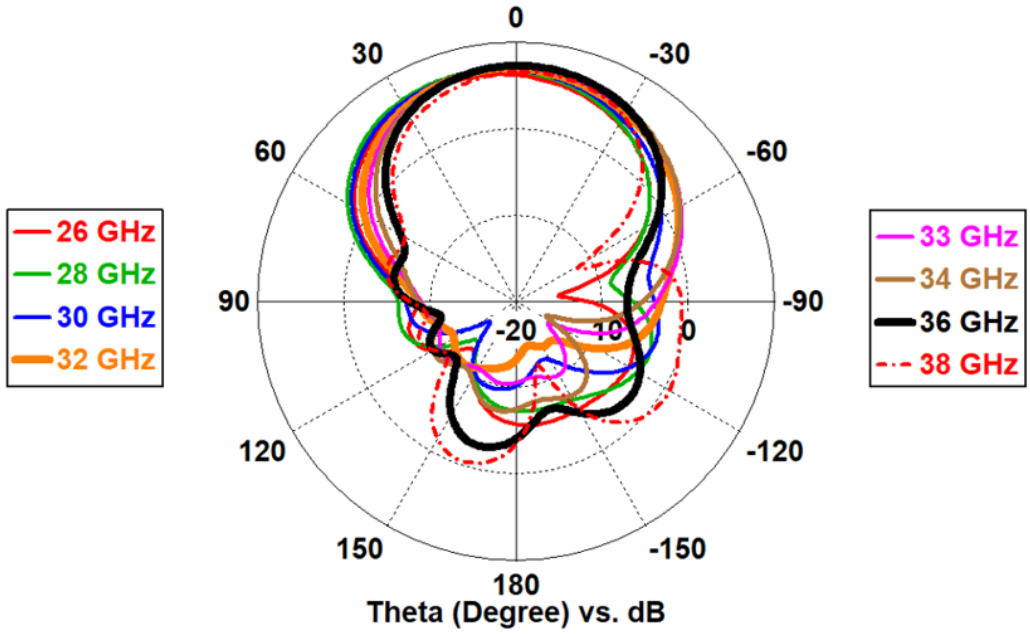

(b)

Figure 4.3: Simulated Quasi-Yagi antenna performance over (26-38) GHz: (a) Gain and reflection coefficient (S_{11}). (b) Radiation patterns.

The phase distributions across the array-ports show a linear behavior as depicted in *Figure 4.6*. Although the phase error of the three focal points is theoretically zero, the multipath reflection might result in some phase deviation. The phase error for the center beam port is about ±3.5°, increases to the maximum phase error of ±6.6° for beam port 1 due to the multipath reflection and the mutual coupling between adjacent ports. A phase error of ±5.4° is for beam port 2 and ±6.2°, for beam port 3. Nevertheless, the radiation patterns, in the next section, indicate that the phase error is still within an acceptable range.

4.3.3 Rotman Lens-Based Beamforming network

Eight Quasi-Yagi antennas are integrated with the proposed lens as shown in *Figure 4.7*. The main beam points at seven different angular directions, as shown in *Figure 4.8* covering the range of $\pm 40°$. The beam directions are uniformly distributed at ±40°, ±26.7°, ±13.33°, and 0°. The maximum achieved simulated realized gain is 14.5 dBi at 28 GHz for the center beam. There is a side lobe of a significant level (SLL ~ -9 dB) when beam port 1 is activated at 28 GHz, however, it is out of the designated field-of-view. The radiation patterns of 38 GHz show a gain drop beyond 3dB at ±40º due to the single antenna element's 3dB *BW*, as explained previously in section 4.3.1.

4.4 Prototyping and Experimental Results

To validate the proposed analog BFN, Rotman lens with seven input ports feeding eight Quasi-Yagi antenna array was fabricated and tested as shown in *Figure 4.9*. The lens is 50mm by 70mm size. The measured reflection coefficients depicted in *Figure 4.10* show good impedance matching below −10 dB over a broad frequency band (26-40) GHz, for all beam ports. The maximum measured gain for the center beam is about 14 dBi at 28 GHz. The radiation patterns shown in *Figure 4.11* validate the system steering capability by providing beams at -39.7º, -26.5º, -13.3º, 0º, +13.3º, +26.5º, and +39.5º.

The radiation patterns have some ripples, especially for the wide angle rays, this is due to some imperfections of the chamber room. The steered beam radiation patterns are vulnerable to such ripples due to the contribution of their side lobes to multipath reflection from different walls of the chamber room, while the central beam has no or less ripples. It can be seen from *Figure 4.4a*, *Figure 4.8*, *Figure 4.10* and *Figure 4.11* that the simulation and measurement results are in a good

agreement. Measured gain is slightly less than the simulated one and ranges between 13.8 to 14 dBi for the center beam port. This difference might be caused by the excessive dielectric losses in the additional length that is needed to separate the connectors at the input port side, and also the use of the end lunch connector to excite the microstrip line introduces additional losses. However, the measured results are quite encouraging taking into account the misalignment losses.

The proposed analog BFN is compared to some relevant works as summarized in *Table 4.3*. It exhibits a reasonable gain level, especially with its compact size. It is smaller than all systems mentioned in the table except [67], [69], and [15] but is better than both of [67] and [69] for its FBW and better than [15] for its low-cost, low profile, and extremely light-weight. Besides, the proposed system has a wide scanning range of ±40º which is better than most of the relevant systems in Table 4.3. [71] has wider scanning range and a quite high gain but is very narrowband with only 4.17 % FBW. [99] and [15] present BFN systems of 100% FBW, which is really a quite broadband, but they have a low scanning range ($|\theta_0| \leq 30°$) compared to the proposed BFN system in this work.

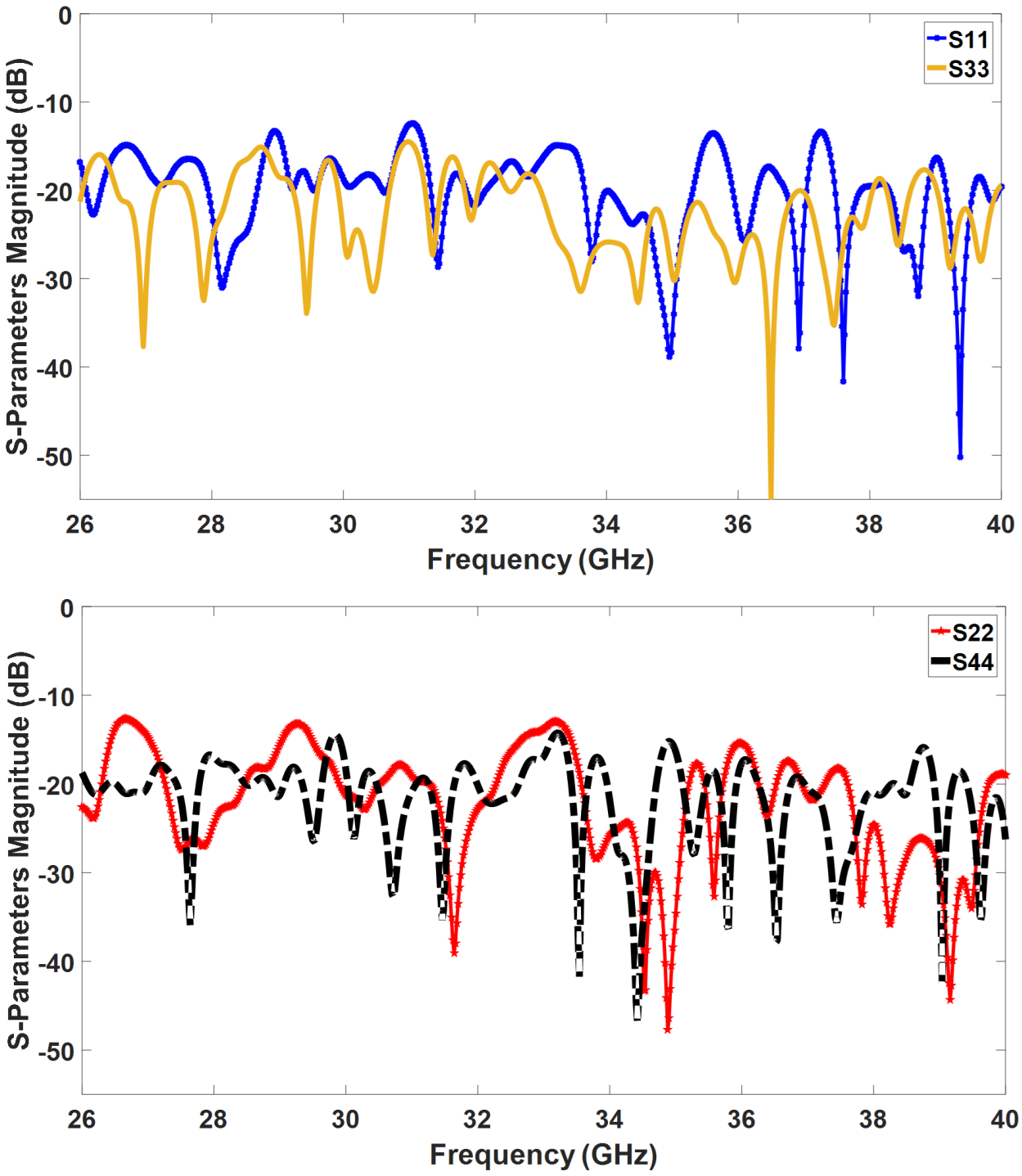
S11
S33
S-Parameters Magnitude (dB)
Frequency (GHz)
0
-10
-20
-30
-40
-50
26
28
30
32
34
36
38
40
S22
S44
S-Parameters Magnitude (dB)
Frequency (GHz)

(a)

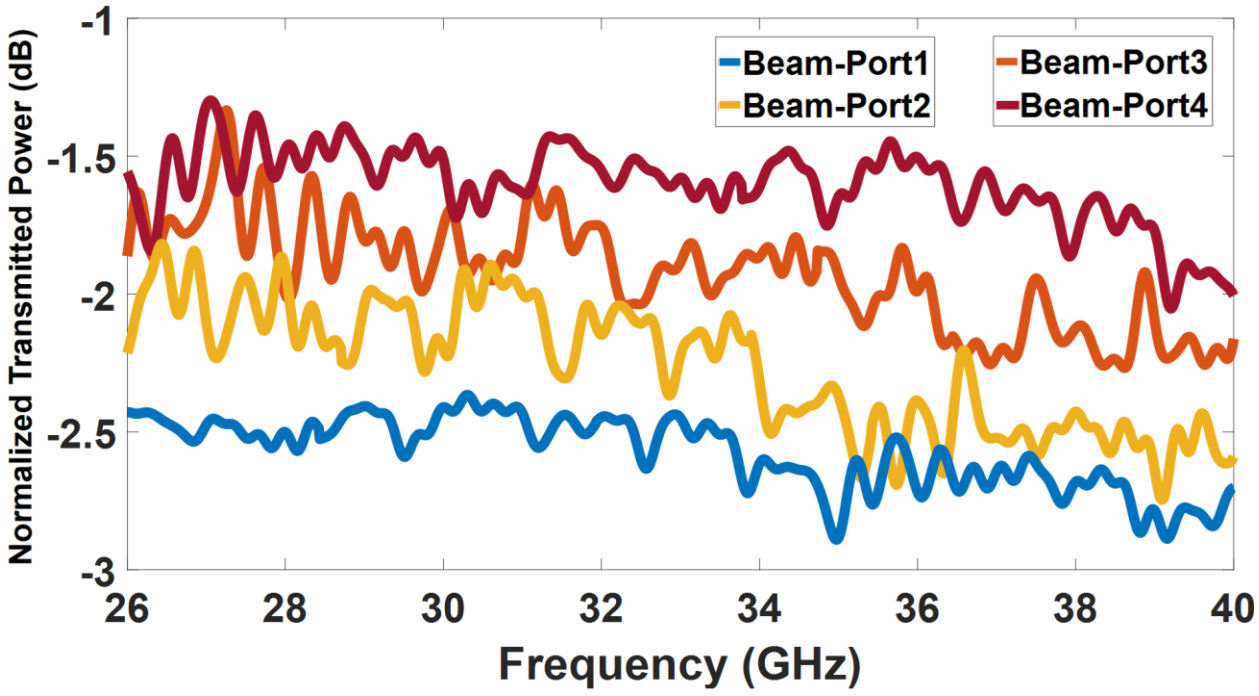

(b)

Figure 4.4: Simulated S-parameters performance of the proposed Rotman lens-based BFN: (a) Reflection coefficients' magnitude. (b) The normalized transmitted power for each beam port. The rest of the ports are not reported for symmetry reason.

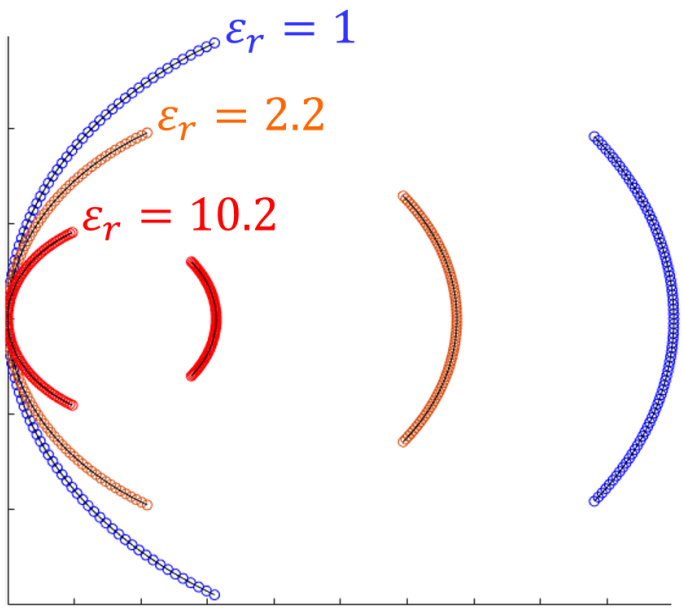

Figure 4.5: The relative size of the proposed Rotman lens with high dielectric material.

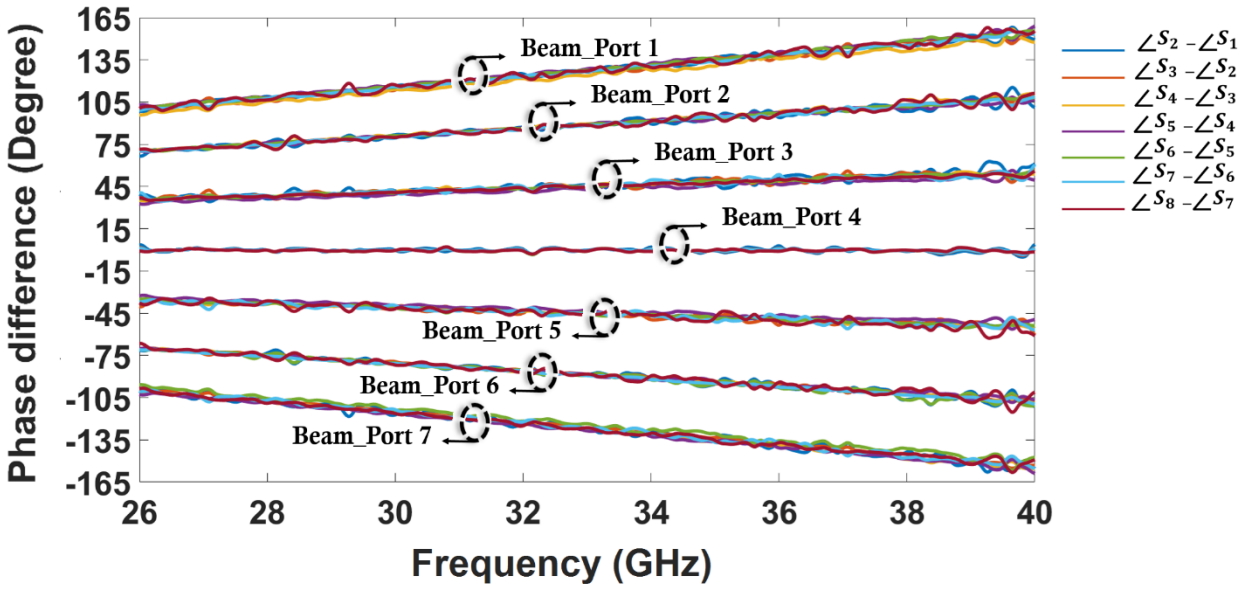

Figure 4.6: Simulated phase performance of the proposed Rotman lens. Each bundle denotes the variation of the phase progression in the array antenna elements with the frequency corresponding to one beam port excitation. Each color represents the phase difference between a pair of adjacent array ports.

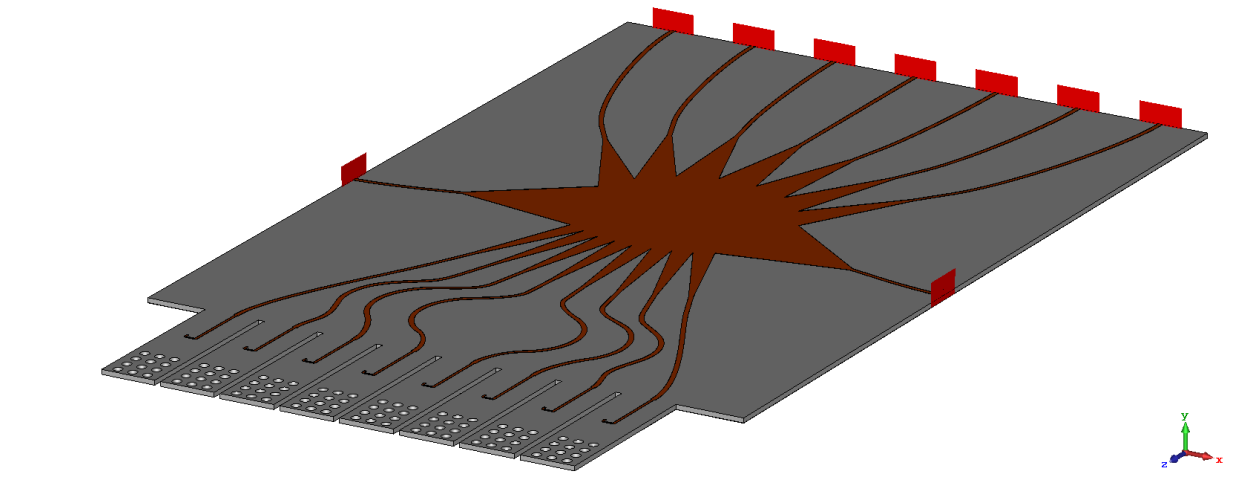

Figure 4.7: Integration of the antenna array with Rotman lens.

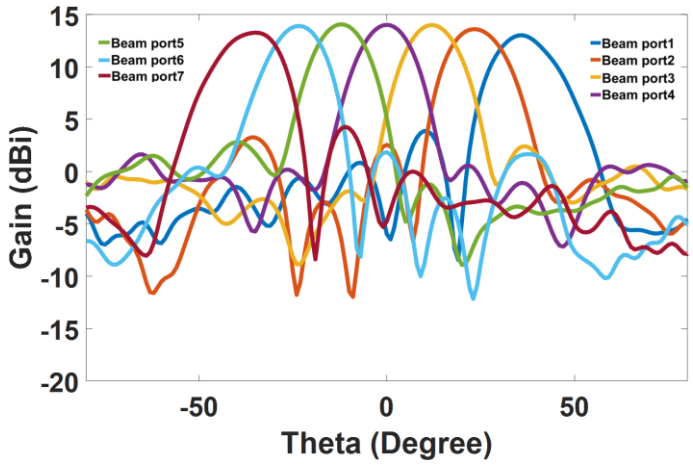

(a)

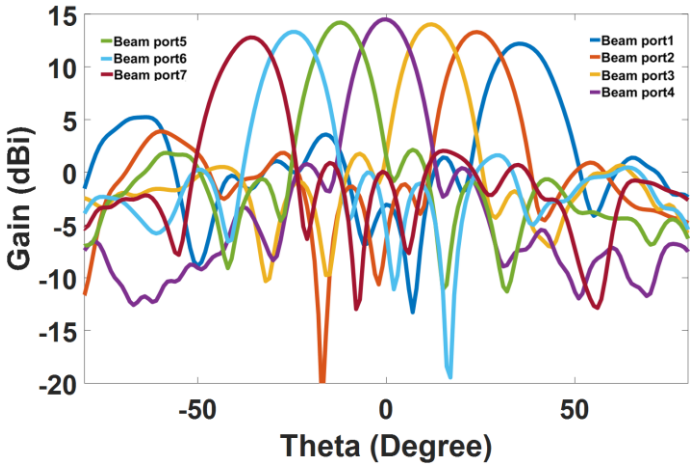

(b)

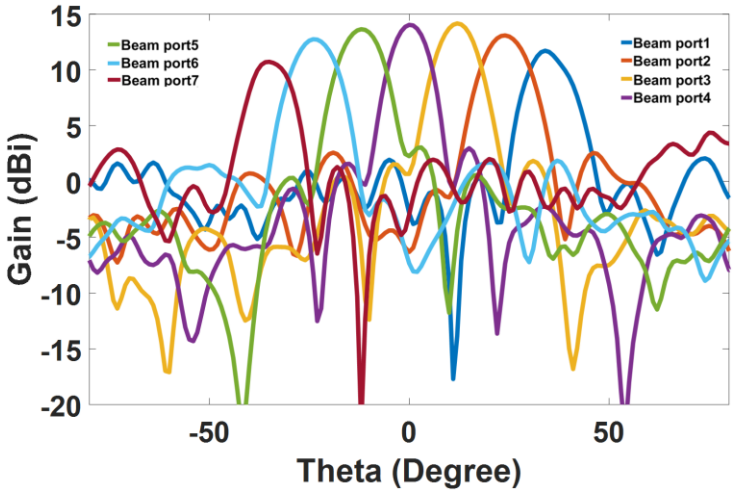

(c)

Figure 4.8: Simulated Radiation patterns of the proposed BFN: (a) 26 GHz. (b) 28 GHz. and (c) 38GHz.

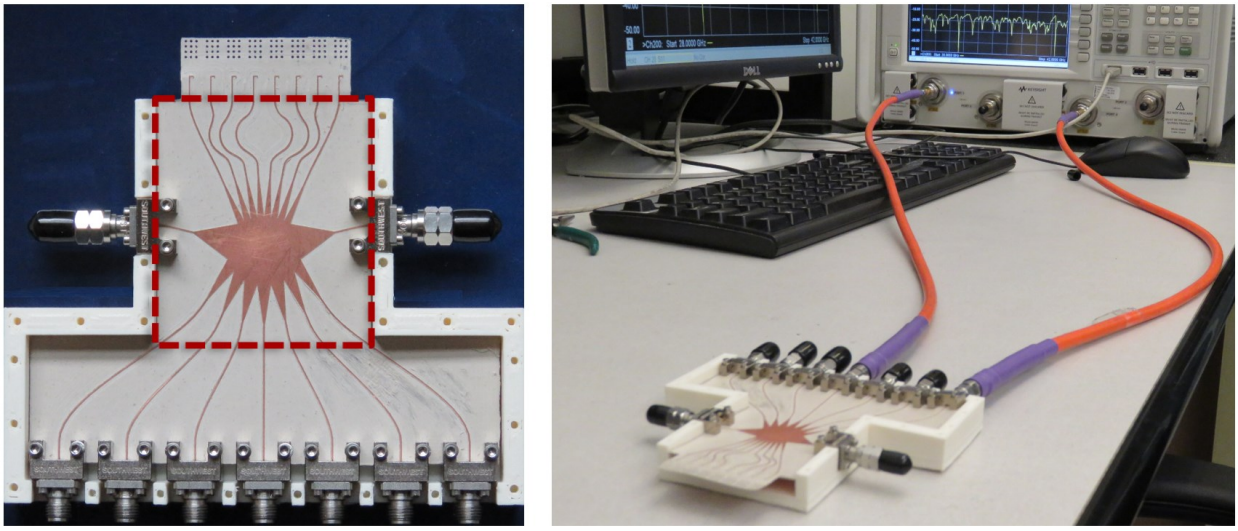

Figure 4.9: Proposed BFN prototype.

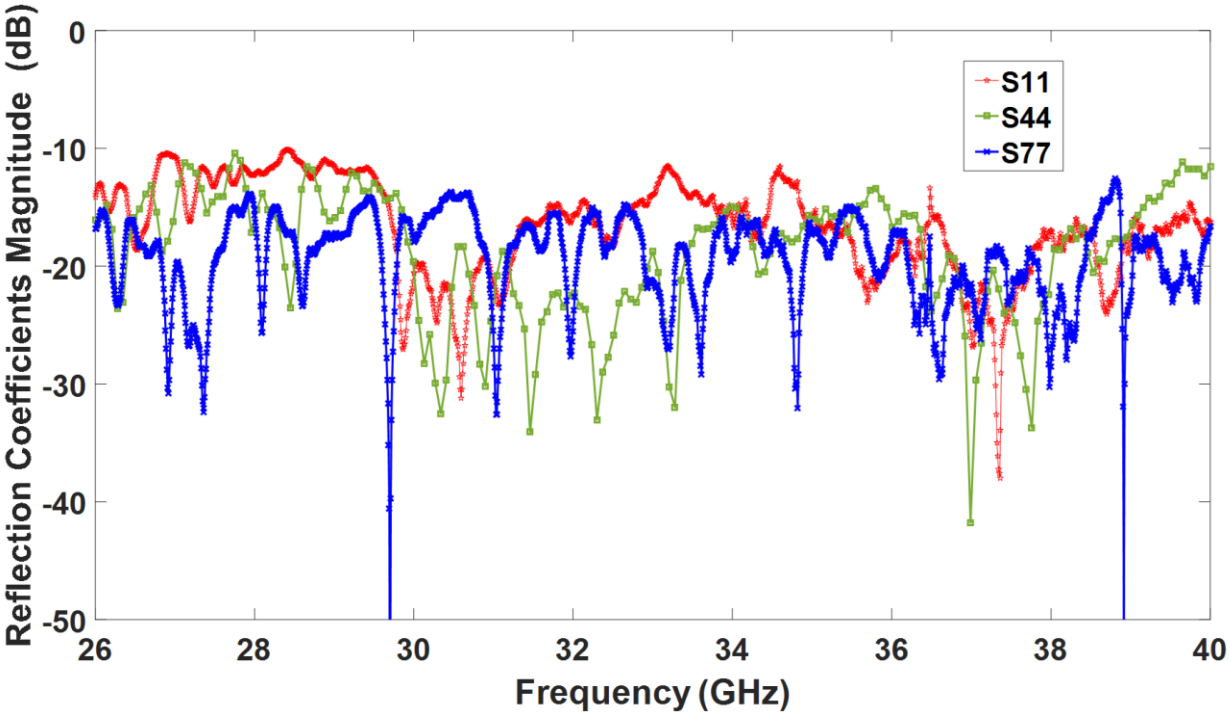

(a)

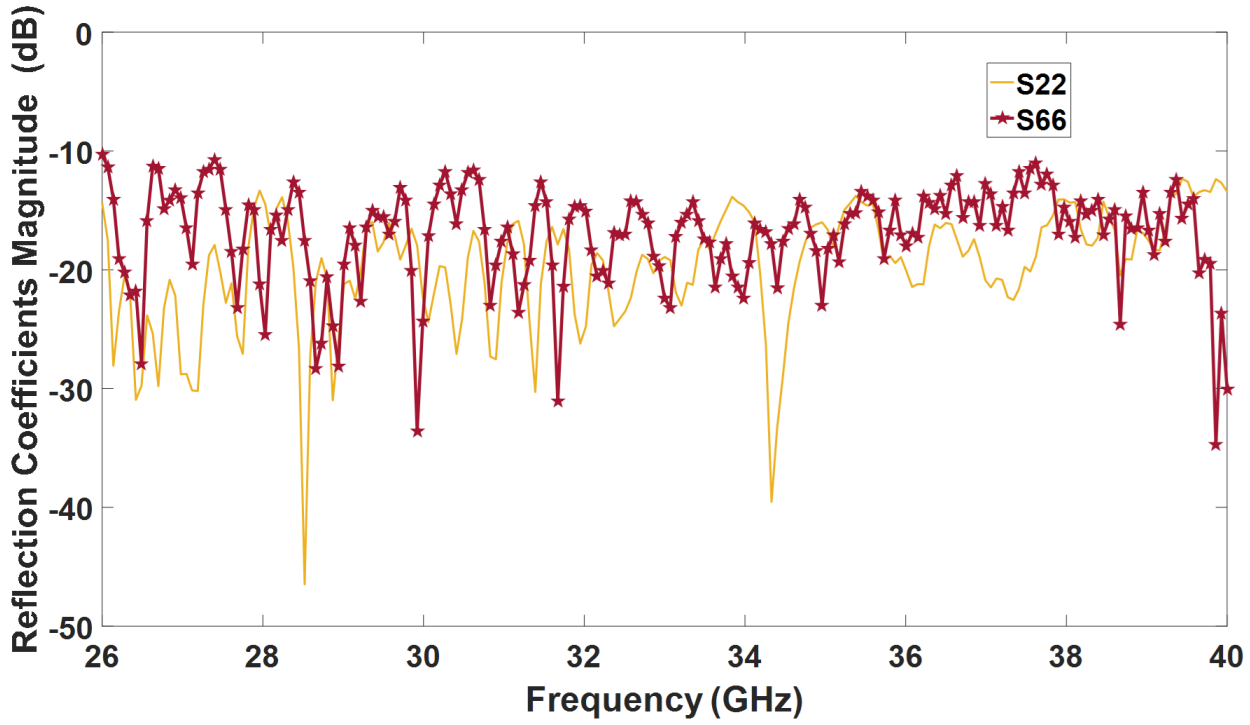

(b)

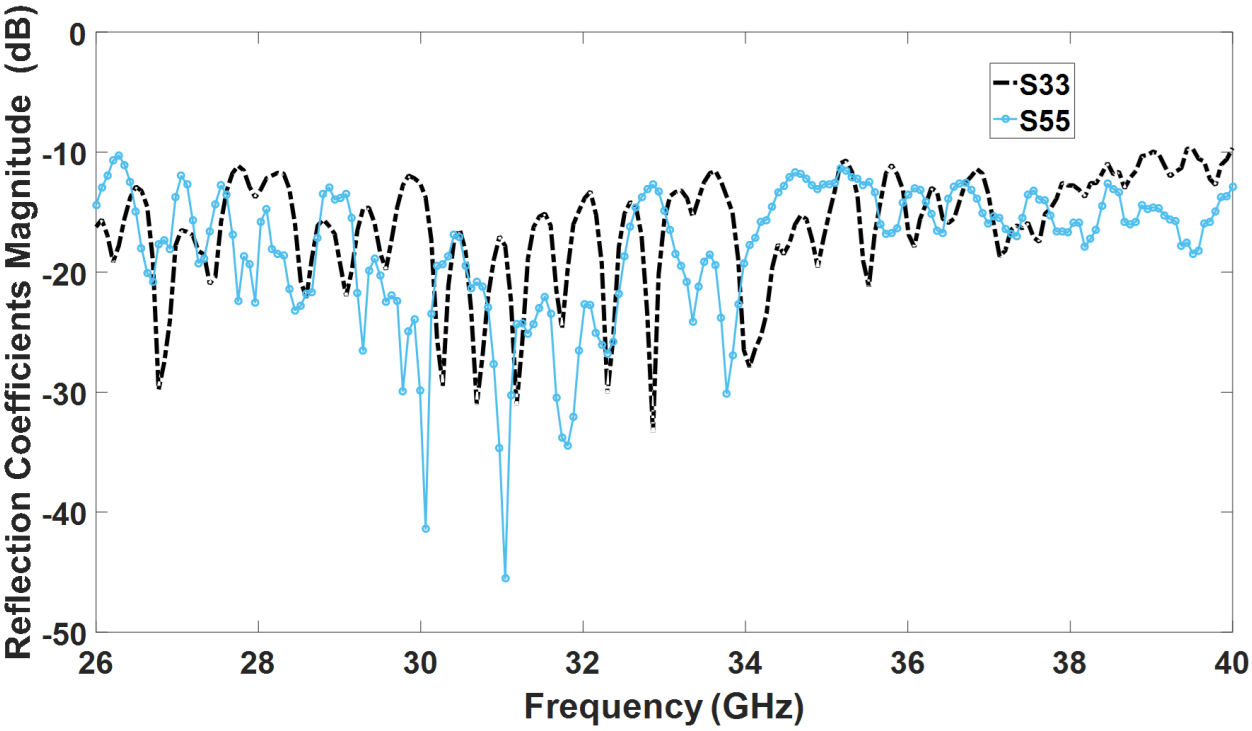

(c)

Figure 4.10: Measured reflection coefficients of the proposed BFN: (a) The center and the two edge beam ports. (b) Beam ports number 2 and 6 (symmetric). (c) Beam ports number 3 and 5 (symmetric).

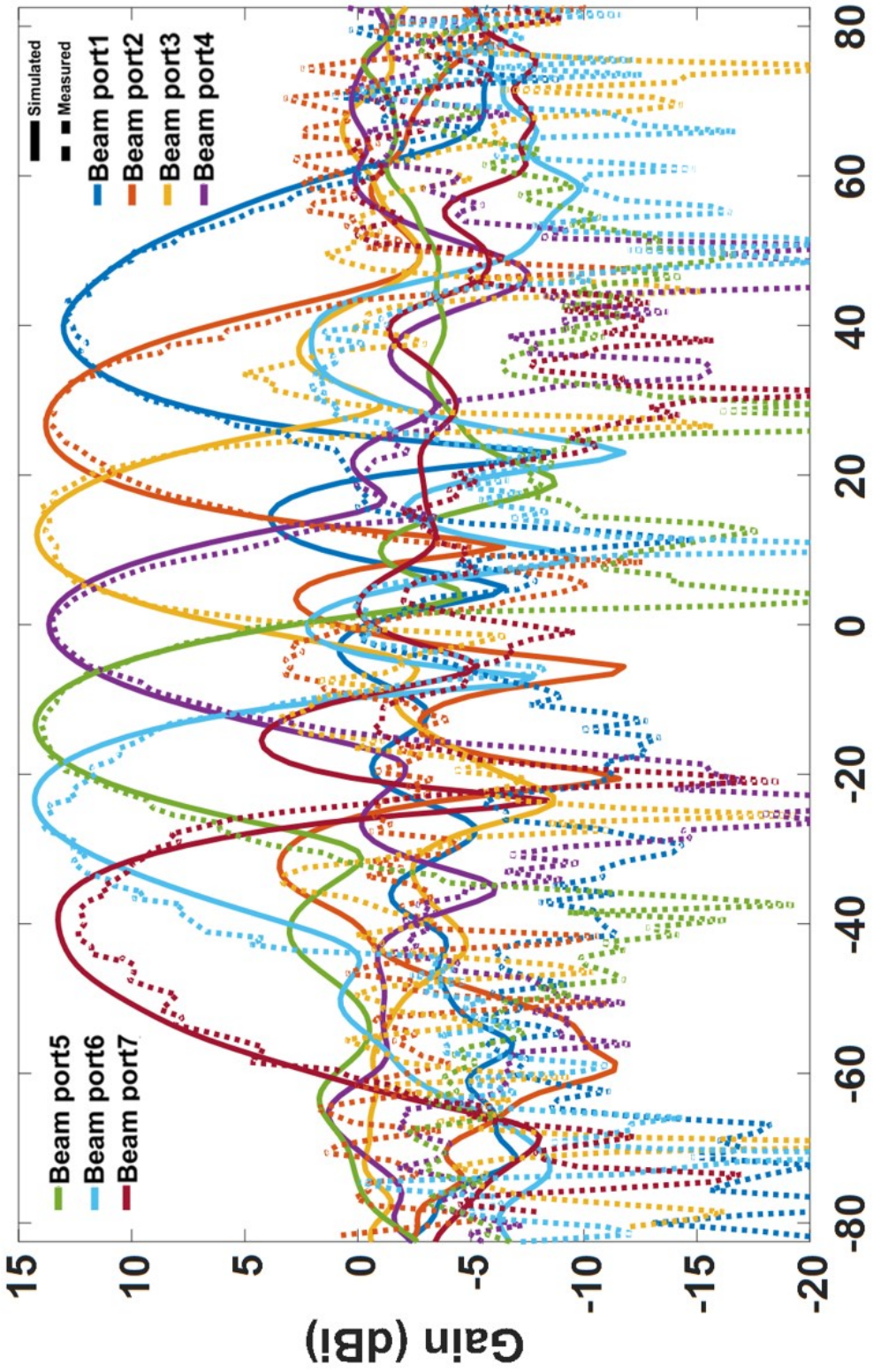

Figure 4.11a: Radiation patterns of the proposed Rotman lens-based BFN at 26 GHz

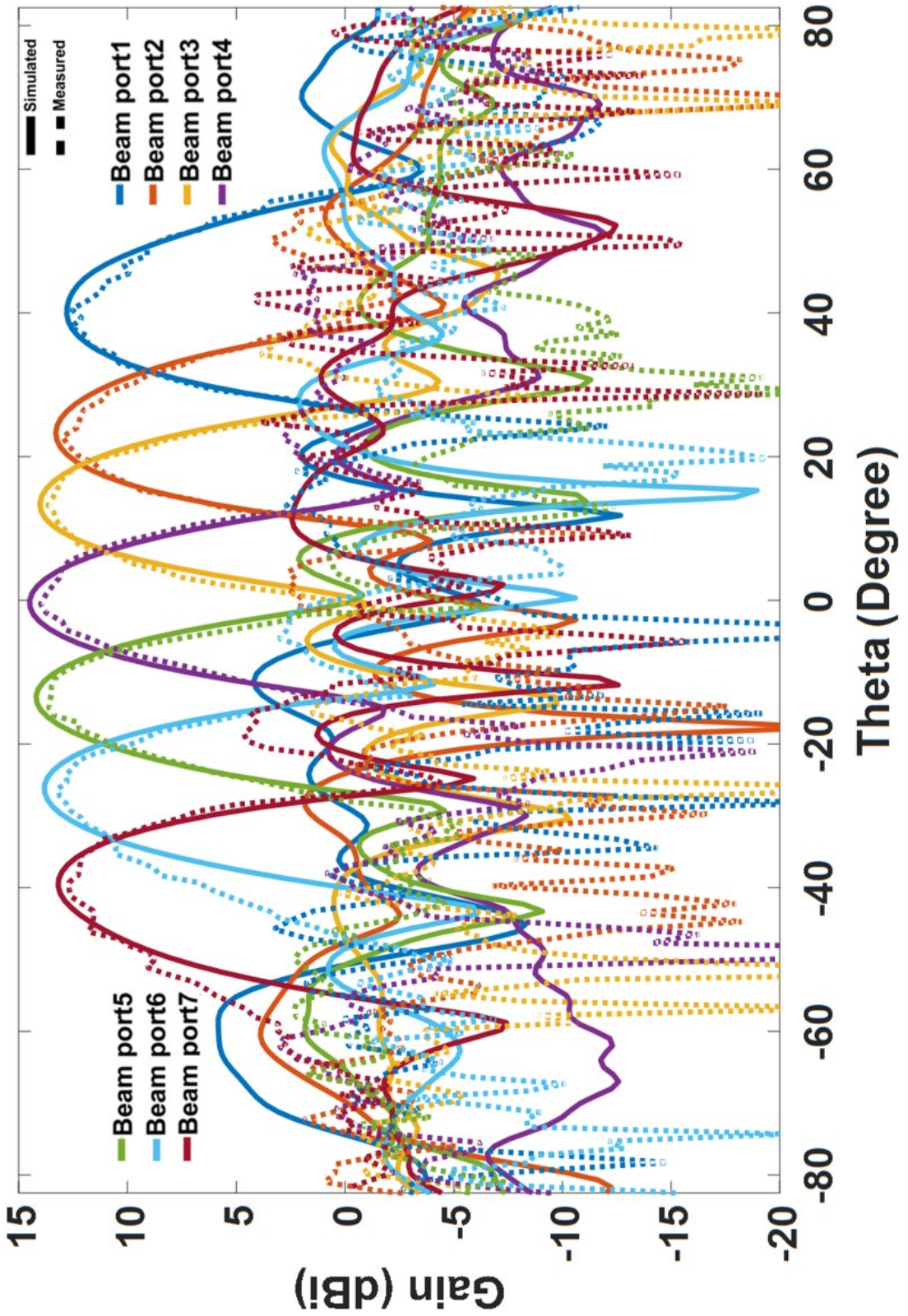

Figure 4.11b: Radiation patterns of the proposed Rotman lens-based BFN at 28 GHz

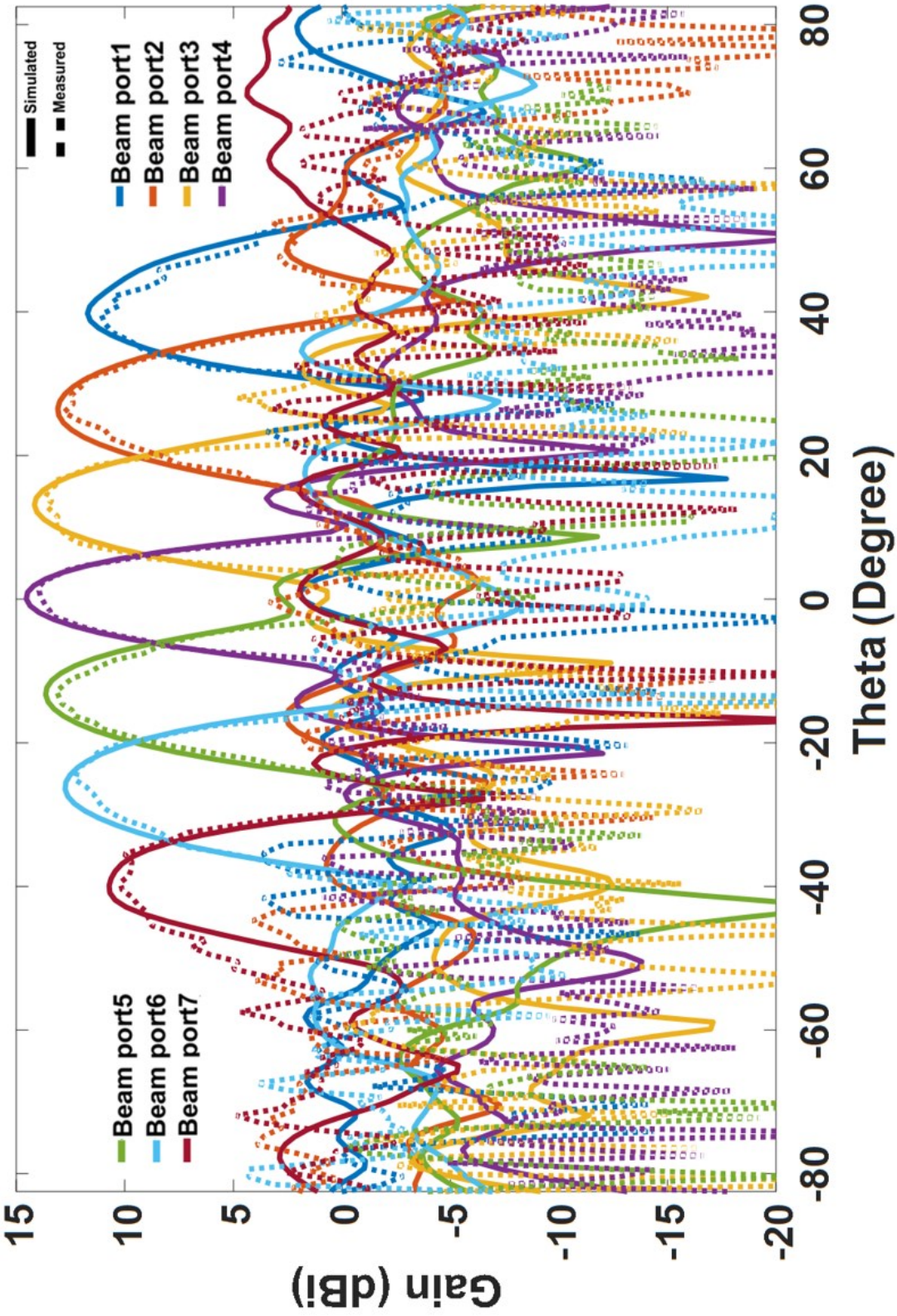

Figure 4.11c: Radiation patterns of the proposed Rotman lens-based BFN at 38 GHz

Table 4. 3: **Comparison of the proposed beamforming network with other related works**

Reference	Number of Ports	Frequency	FBW	Scanning Range	Gain	Electrical Size	Fabrication Technology	Antenna Element
	M×*N*×*D*	GHz	%	degree	dBi	mm^2		
[69]	7×7×8	15.5-16.5	6.25	-30˚ to +30˚	13	5.3 λ_0 × 6.4 λ_0	SIW	Vivaldi
[71]	7×15×2	23.6-24.6	4.17	-48˚ to +48˚	22.6	7.2 λ_0 × 12 λ_0	SIW	Slotted WG
[73]	5×7×14	26.4-40.1	41.2	-20˚ to +20˚	-	>17.8 λ_0 × 17.8 λ_0	RWG	WR28
[74]	11×16×8	60	-	-40˚ to +40˚	-	Not reported	PRGW	-
[15]	5×5×0	6-18	100	-30˚ to +30˚	9-13	5.2 λ_0 × 6.12 λ_0	3DP-RGW	Double ridge horn
[75]	5×8×8	50-70	33.3	-30˚ to +30˚	-	7.6 λ_0 × 8.77 λ_0	inkjet	-
[99]	8×10×28	6-18	100	-28˚ to +28˚	2-20.6	12 λ_0 × 12 λ_0	PCB	Double ridge
[67]	7×10×8	26-29	10.9	-29˚ to +29˚	14.3	4.0 λ_0 × 8.40 λ_0	PCB	Patch
[66]	5×6×4	25-30	18.2	-40˚ to +40˚	-	7.3 λ_0 × 11.2 λ_0	PCB	Patch
This work	7×8×2	26-40	42.4	-40˚ to +40˚	14.0	5.5 λ_0 × 7.70 λ_0	PCB	Quasi-Yagi

4.5 Summary

An analog beamforming network using a compact-size Rotman lens fed eight Quasi-Yagi antenna array for 5G and mm-wave applications is presented. The proposed system was fabricated using standard planar low-cost processing PCB technology for MMIC in the 26-40 GHz band. The antenna and the beamforming network design methodology is described in details, and its performance is confirmed experimentally. The system exhibits good impedance matching and beam steering capability. A range of ±40º is achieved which is better than most of the relevant systems in *Table 3*. The BFN bandwidth ($S_{11} < -10$ dB) is larger than 42 % and is limited by the single antenna element bandwidth. With such performance and compactness, the proposed system is qualified for a wide range of potential 5G applications such as the advanced MIMO and hybrid beamforming networks.

CHAPTER 5: Rotman Lens-based BFN with RGW

5.1 Introduction

RGW is a promising technology for mm-wave devices, and integrated systems as only air and metal are used so that the propagating mode is a quasi-TEM inside an air gap [100-104].

This chapter mainly concerns the RGW for the implementation of Rotman lens-based analog BFN. Section 5.2 addresses the basic concept of RGW technology, which depends on two main principles—Soft and Hard surface and EBG structures—which were already discussed in chapter 2. These principles are used for designing an RGW unit cell in subsection 5.2.1, which is carried out while a PRGW unit cell is covered in 5.2.2. Section 5.3 explains why this technology has been selected to replace the traditional guiding structure (such as MS technology). After that, Rotman lens-based BFN (introduced in chapter 4) with MS technology is replaced by a new one with the RGW technology in section 5.4, the simulation results of the new BFN is presented in subsection 5.4.1. Similarly, subsection 5.4.2 covers simulation results of the Rotman lens-based BFN with the PRGW. Finally, the summary comes in section 5.5.

5.2 Ridge Gap Waveguide System Design Configuration and Analysis

Simply put, RGW is to create a parallel plate guiding structure that consists of a metallic ridge surrounded by a periodic structure—that is, to act as an artificial magnetic conductor (AMC) [105] (as shown in *Figure 5.1*) and an upper metallic plate, which, essentially, allows the wave propagation in a specific region and prevents the propagation in all other directions. The gap between the upper plate and the ridge is smaller than $\lambda/4$. The propagating mode inside the air gap is a quasi-TEM, while the transverse fields are forced to be zero in the surrounding areas, which is according to the Hard and Soft Surfaces principle.

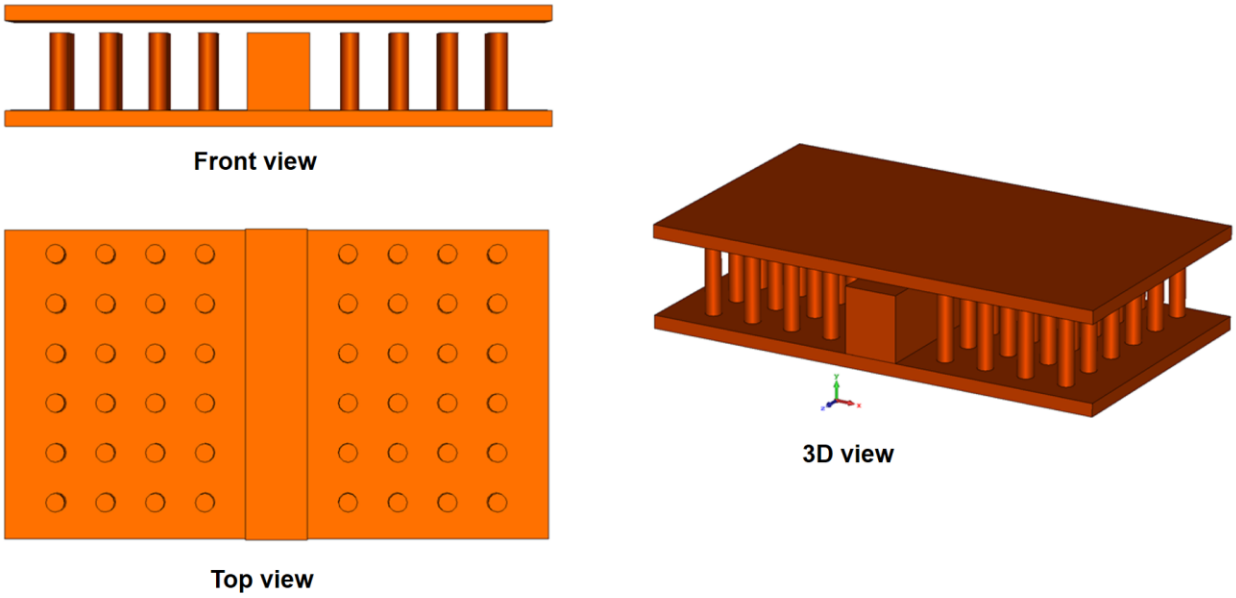

Figure 5.1: Geometry of RGW with upper plate is hidden.

5.2.1 RGW Unit Cell Analysis

The starting point for designing RGW is determining its operational frequency band. Ideally, the stop band of the unit cell is the operational band of the integrated RGW system. Because the surrounding surfaces are periodic structures that form parallel plate gap waveguides with one textured metal pin surface, they should be designed based on numerical analysis for a unit cell of specific EBG. *Figure 5.2a* illustrates the dispersion diagram of an RGW unit cell, which was computed using CST Microwave Studio Eigenmode solver. The gap waveguide with ridges was not included in the simulations because the focus was only on the cut-off region where no waves are allowed to propagate. In essence, it shows that the periodic structure of this unit cell can prevent the electromagnetic wave propagation from 24 GHz to 52 GHz. the cell dimensions are given in *Table 5.1*. After designing the unit cell, a ridge with a width of W for certain characteristic impedance Z_0 is constructed and simulated as shown in *Figure 5.2b*. The ridge characteristic impedance is approximated by a strip line equation to calculate the initial dimension [106]. More details pertaining to the effect of different parameters of the unit cell are found in [78]. The distance between the ridge and the nail center should be around half of the unit cell period (a). It can be seen that the wave propagates as a quasi-TEM and the bed of nails successfully prevents the wave

propagation beyond the ridge area. *Figure 5.3* depicts the electric field distribution on the RGW at the center frequency. The S-parameters are simulated using CST and HFSS are shown in *Figure 5.4*, which confirm the role of the bed of nails in preserving the quasi-TEM propagating mode within the ridge area—specifically, for the frequency band 26 GHz to more than 52 GHz.

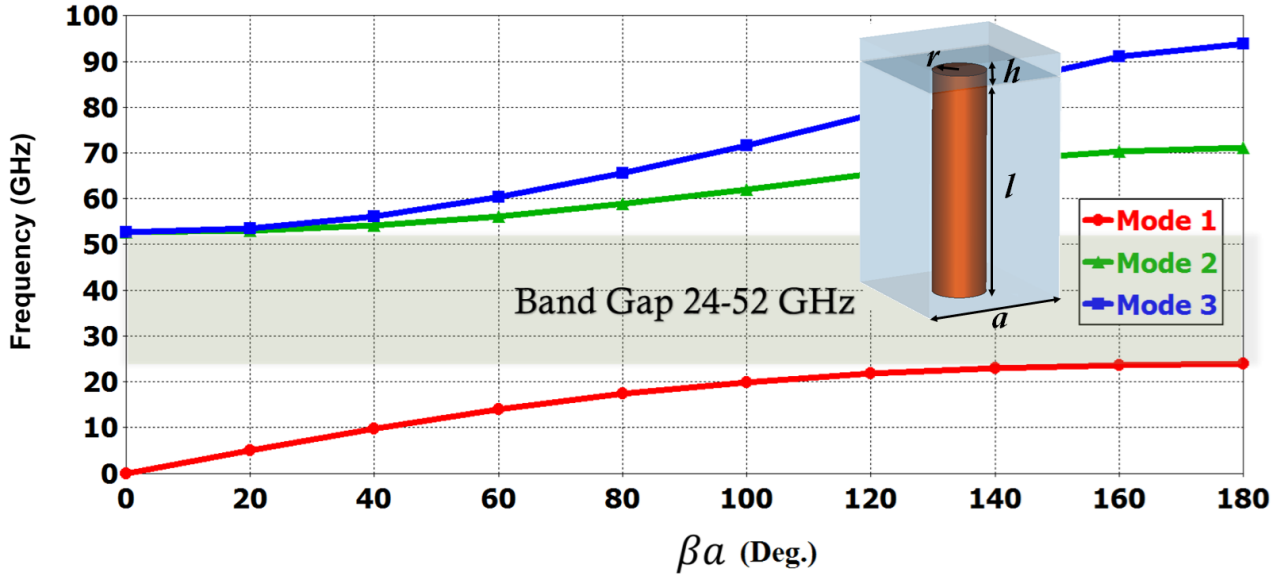

(a)

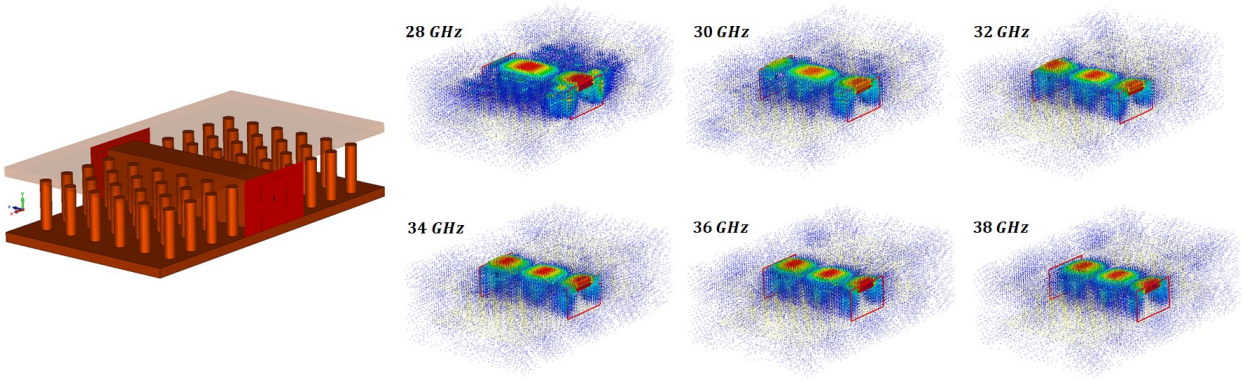

(b)

Figure 5.2: The parallel plate gap waveguide with one textured metal pin surface: (a) The unit cell dispersion relation. (b) The wave propagation as a quasi-TEM in the RGW system for different frequencies

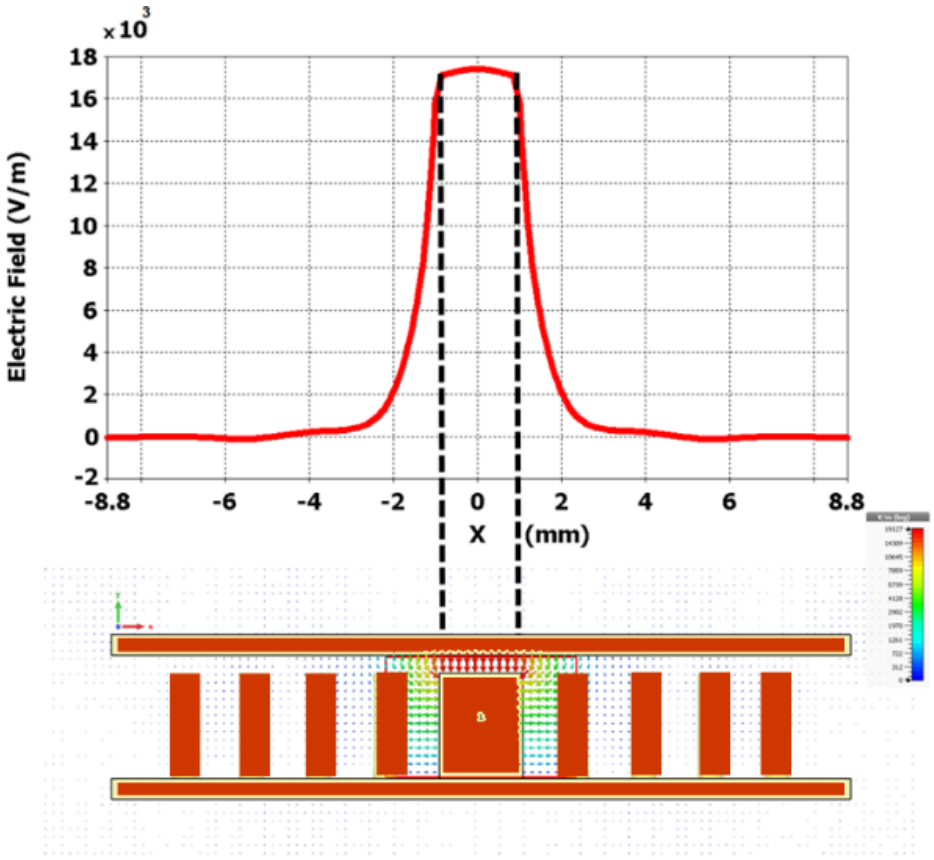

Figure 5.3: The Electric field distribution on the RGW at the center frequency.

Table 5. 1: **Unit cell dimensions of the proposed RGW**

Parameter	Value (mm)
a	1.600
h	0.398
l	2.500
r	0.300

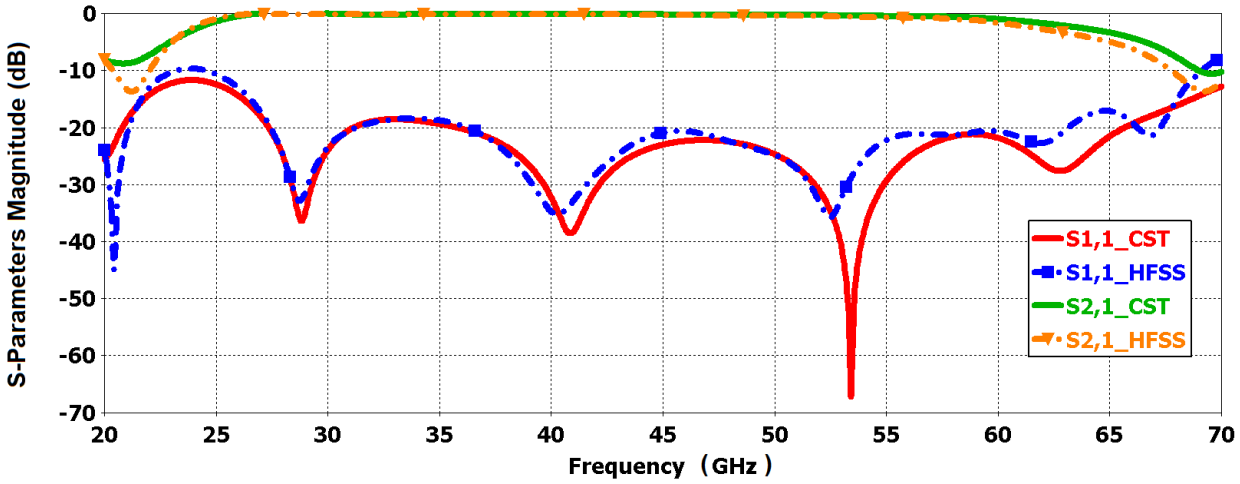

Figure 5.4: The S-parameters of the RGW with the proposed unit cell.

5.2.2 Printed Ride Gap Waveguide

PRGW is a RGW that is implemented using a traditional PCB technology. It is a new cost-effective guiding structure for mm-wave systems because the propagating mode is a quasi-TEM inside an air gap, which provides low signal distortion and low losses compared to microstrip technology [J2],[19],[74]. The printed ride line is realized by connecting the microstrip line to the ground through metallic pins, and then the surrounded AMC surface is realized using a mushroom-shaped unit cell (as shown in *Figure 5.5*). The dispersion diagram of a PRGW unit cell is illustrated in *Figure 5.6a* and the dimensions are tabulated in *Table 5.2.* It shows that the periodic structure of this unit cell has a band-gap from 26.5 GHz to 40 GHz. Therefore, the PRGW is constructed and simulated as shown in *Figure 5.6b*. It can be seen that the wave propagates as quasi-TEM and the mushroom surface prevent wave propagation beyond the ridge area for different frequencies. As the frequency approaches the edges of the band-gap, the electric field leaks from the printed ridge through the mushroom surface. *Figure 5.7* shows the electric field distribution on the PRGW at the center frequency. The S-parameters of the PRGW are shown in *Figure 5.8* confirm the role of the mushroom surface in preserving the quasi-TEM propagating mode—that is, within the printed ridge area for the frequency band 26.5 GHz to 40 GHz.

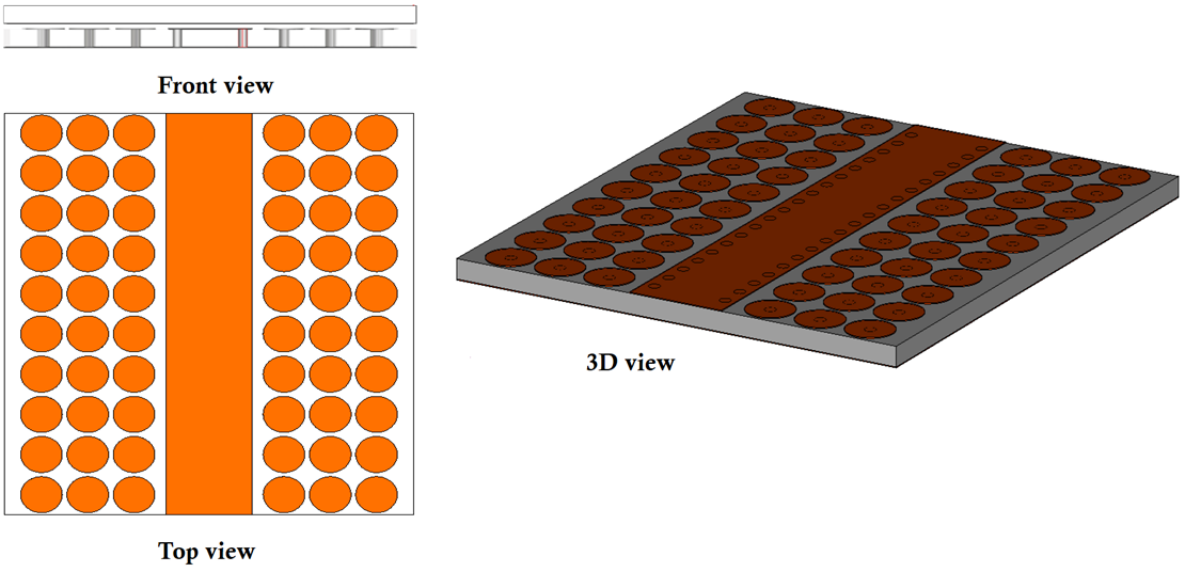

Figure 5.5: Geometry of PRGW with upper plate is hidden.

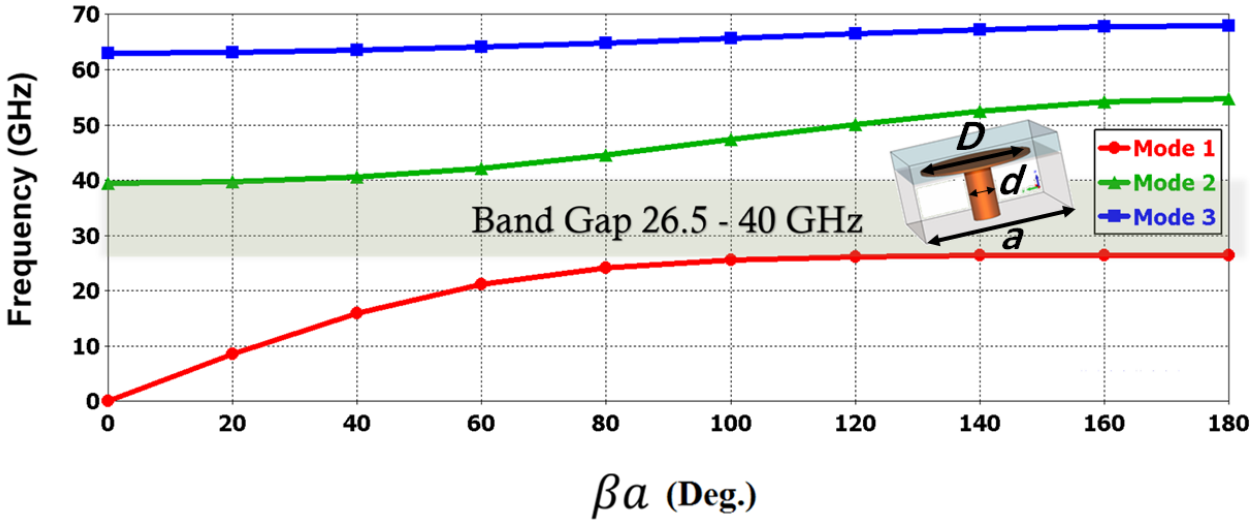

(a)

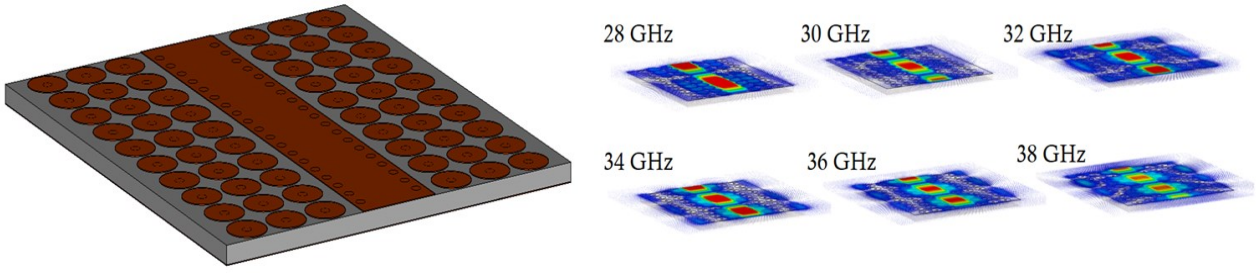

(b)

Figure 5.6: The printed ridge gap waveguide with mushroom-shaped unit cell: (a) The unit cell dispersion relation. (b) The wave propagation as a quasi-TEM in the PRGW system for different frequencies

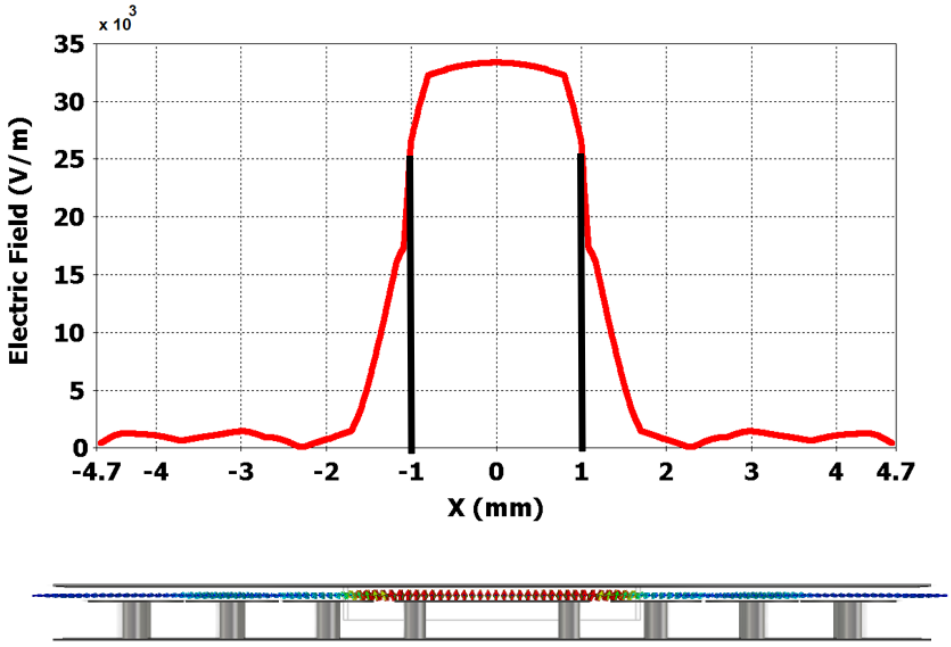

Figure 5.7: The Electric field distribution on the PRGW at the center frequency.

Table 5. 2: **Unit cell dimensions of the proposed PRGW**

Parameter	Value (mm)
a	0.500
h	0.127
l	0.381
D	0.860
d	0.100

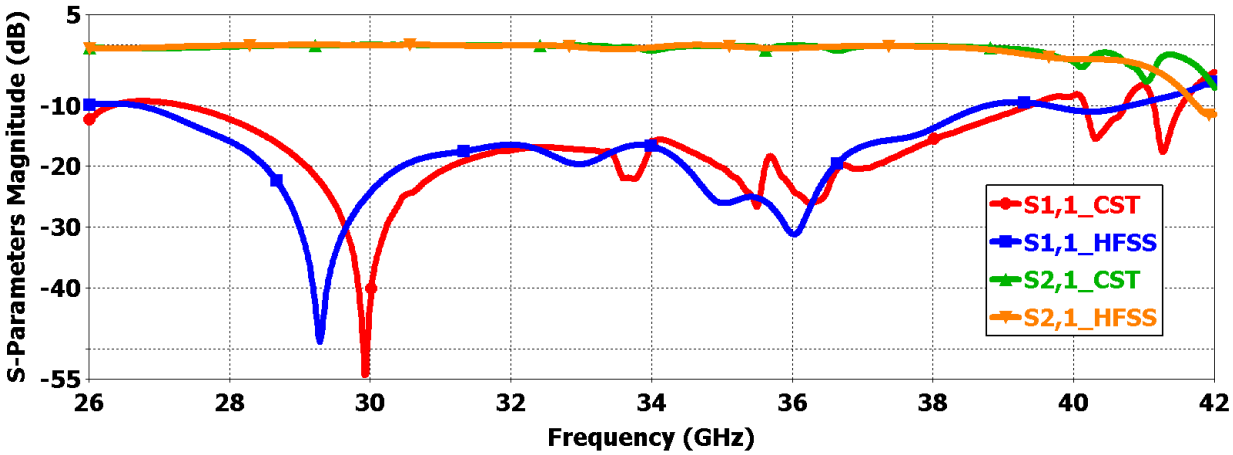

Figure 5.8: The S-parameters of the PRGW TL with the proposed mushroom-shaped unit cell.

5.3 Comparison Between Ridge Gap Waveguide and Microstrip Technologies

The microstrip waveguides have been widely used in microwave technology in many applications for their simple structure, cost-effective and ease of fabrication process. However, MS technology-based systems suffer excessive dielectric losses, especially at high-frequency bands. Thus, RGW is introduced to replace MS technology [J2,19]. Both the MS and the RGW have advantages and disadvantages compared to each other. Both technologies carry quasi-TEM mode, but the MS-based guiding structure involves a dielectric loss due to its substrate. On the other hand, the RGW has no dielectric loss where the wave propagates inside an air gap. Both technologies have conductor loss, and the MS has higher conductor loss than the RGW [105]. In terms of the size and cost, MS technology is smaller than RGW, especially when high dielectric materials are used. However, the mechanical strength of the RGW component and power handling is much higher for the same components based on MS. Hence, it is only the application or the required performance that bias the choice between the two technologies. PRGW is a compromise solution, where it possesses ease of fabrication with the PCB technology, in addition to the advantage of the wave propagation in air only as the metallic RGW. Another alternative choice is the 3DP-RGW. In which, a copper electroplated PerFORM, which is an opaque white plastic that behaves similarly to polycarbonate and has elevated heat resistance, is used instead the whole metal RGW [107].

5.4 Simulation Results

Rotman lens-based BFN (introduced in chapter 4) with MS technology is replaced by a new one with the RGW technology, in subsection 5.4.1. Similarly, subsection 5.4.2 covers the Rotman lens-based BFN with the PRGW.

5.4.1 RGW Rotman Lens-based BFN

This subsection discusses, mainly, the simulation results of the transition between the RGW line and the microstrip line in subsection 5.4.1.1. Then, the integration between the proposed single element and the RGW line in subsection 5.4.1.2. The proposed Rotman lens, implemented in the RGW, is explained in subsection 5.4.1.3. Finally, the overall RGW beamforming network is covered in subsection 5.4.1.4.

5.4.1.1 Microstrip Line to RGW Transition

In order to connect the RWG Rotman lens to standard 50 Ω connectors, a simple microstrip line and a matching section in the ridge are designed and simulated as shown in *Figure 5.9a*. The transition section requires a substrate of a dielectric constant close to one. Because the microstrip line and is a sort of a dielectric filled parallel plate structure, while the ridge gap waveguide is an air filled parallel plate-like structure. Therefore, the permittivity of the matching section substrate should be reduced. There are different methods to implement specific values of the dielectric constant using standard substrates of higher dielectric constant which are discussed in many applications like the dielectric lens antennas and the microwave devices [J1, 62–65]. Perforating method is selected in this work. Accordingly, an equivalent effective dielectric constant model was designed using the equation (2.6.3). The values of d_x and d_z are set to be 1.25 mm, which is the minimum recommended value by the fabrication rules. Similarly, the maximum possible hole diameter is 1.00 mm due to some fabrication rules, where a minimum clearance between the hole and the line edges must be maintained. The geometry of the transition section between MSL to RGW along with S-parameters with and without perforating are depicted in *Figure 5.9.* It can be seen that the transition section has good impedance matching ($|S_{11}|$<-15 dB) in the entire operational bandwidth.

5.4.1.2 Integration Between Quasi-Yagi Antenna and RGW

The RGW-to-MS transition section, designed in the previous subsection, is replaced by a quasi-Yagi antenna as shown in *Figure 5.10a*. The overall system reflection coefficients, depicted in *Figure 5.10b*, is better than -10 dB in the entire frequency band 26-40 GHz. However, compared to the single element described in chapter 3, the relatively large ground results in narrower 3dB *BW* for the frequencies higher than 36 GHz, as shown in the radiation patterns of the antenna in *Figure 5.10c*.

5.4.1.3 RGW Rotman Lens Design

Rotman lens with eight array ports was simulated in the RGW technology as shown in *Figure 5.11*. The lens was designed according to the methodology described in chapter 2 (2.6.4) for optimum amplitude and phase error performance in the frequency band 26-40 GHz. The original design requires Nine beam ports, to steer the beam within a maximum scanning range of ± 40º, and a minimum array element spacing of $0.5\lambda_0$. Thus, a minimum focal length of $4.5\lambda_0$ is calculated. Therefore, the focal length is set to be $5\lambda_0$. To have a frequency independent system, additional space between the lens array ports and the array antenna elements is necessary. the analog beamforming network was designed with the parameters specified in *Table 5.3*.

Table 5. 3: **Main Parameters of the proposed RGW Rotman lens**

Parameter	Symbol	Value
On-axis focal length	f_1	$5\lambda_0$
Focal angle	α	40°
Focal ratio	β	0.92
Expansion Factor	γ	1
Scanning range	$\pm\theta_0$	±40°
Number of Array-ports	N	8
Number of Beam ports	M	9
Number of Dummy-ports	D	2
Total BFN length	LBFN	192 mm
Total BFN Width	WBFN	124 mm

Figure 5.12 shows the electric field of the propoded RGW Rotman lens. It can be seen that the propagating mode in the parallel plate region is a pure TEM, and the transmission lines are isolated from each other, carrying a quasi-TEM. The simulation results indicate good impedance matching for the proposed lens, where reflection coefficients of all beam ports, as illustrated in *Figure 13a*, are better than −10 dB. The proposed BFN has good S-parameters magnitude at the array-ports, with a relative transmitted power level ranges between -0.8 dB to -2.85 dB over 27.5-40 GHz, as shown in *Figure 13b*. The rest of the ports are not reported for symmetry reason. It should be noted that there is a modest amplitude tapering experienced by array-ports, due to different distances from beam port. The tapering effect increases when feeding from the edge beam port. Besides, the spillover losses and the absorbed power by the dummy loads contribute to power level reduction. Consequently, the BFN's gain decreases compared to the gain of ideal *N*-element, uniformly excited, and equally spaced linear array. The relative total transmitted power accounts for all types of loss and is calculated using Equation (4.3.1). These losses are expected as discussed and increase unavoidably with the increase of the scanning angle, especially, at higher frequencies. However, the lens amplitude and phase error performance are quite good. The phase distributions across the array-ports show a linear behavior, as depicted in *Figure 5.14a* and *Figure 5.14b* in the entire operational band except below 27.5 GHz. this might be due to a lens size, where its on-axis focal length is about $5\lambda_0$ of the center frequency and should have been selected larger to allow reasonable parallel plate region for TEM mode propagation in case of larger operational wavelengths.

Although the phase error of the three focal points is theoretically zero, the multipath reflection might result in some phase deviation. The phase error for the center beam port is about, ± 40º increases to the maximum phase error of ± 6º for beam port 3 due to the multipath reflection and the mutual coupling between adjacent ports. Besides, the phase error increases for rays between foci [57]. Nevertheless, the radiation patterns, in the next section, indicate that the phase error is still within an acceptable range.

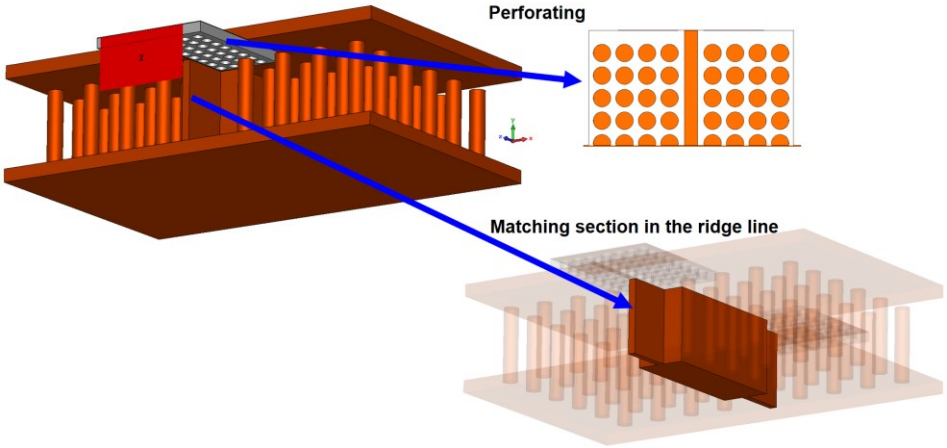

(a)

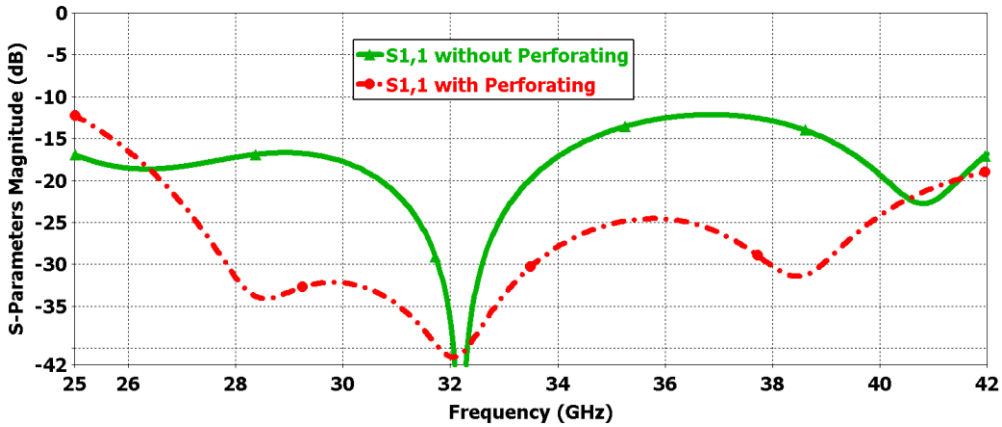

(b)

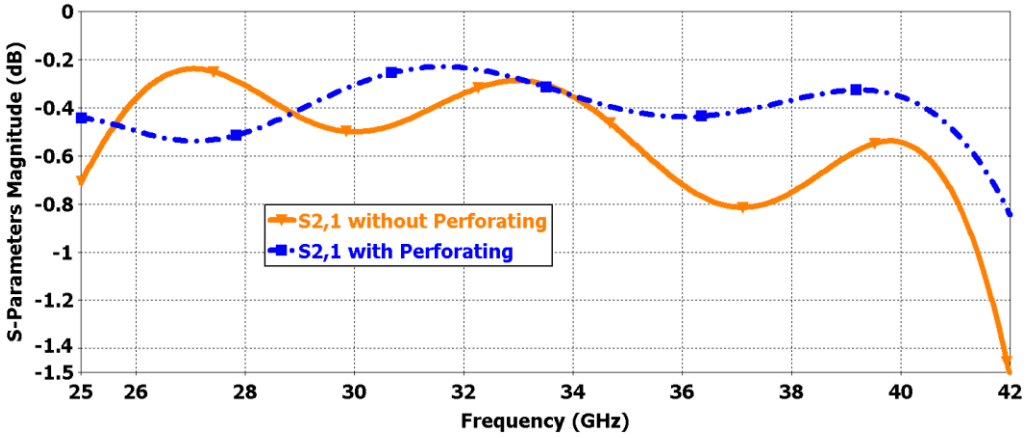

(c)

Figure 5.9: MSL to RGW transition: (a) 3D structure. (b) Reflection coefficient magnitude. (c) Transmission coefficient magnitude.

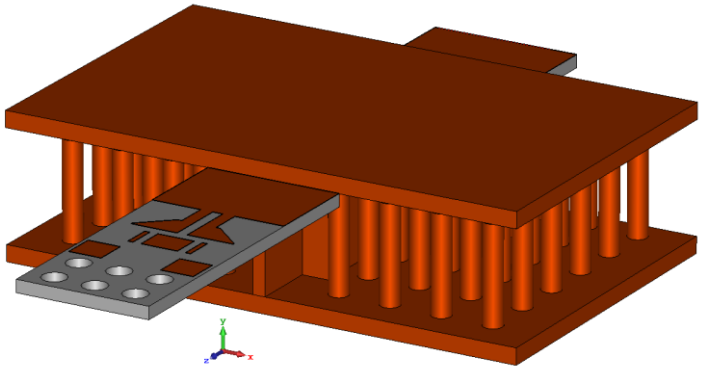

(a)

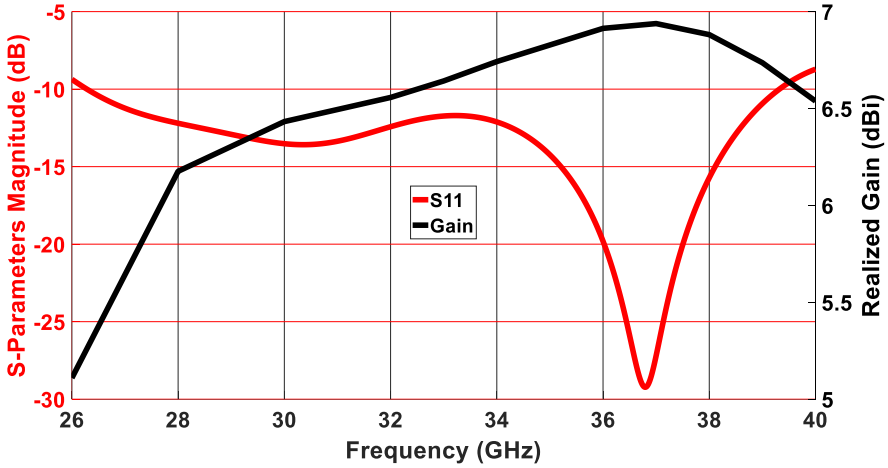

(b)

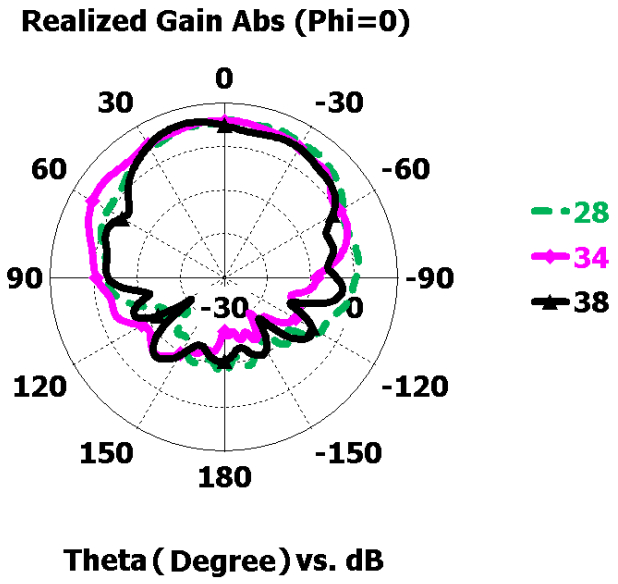

(c)

Figure 5.10: The integrated MS Quasi-Yagi antenna and RGW system: (a) Geometry. (b) Reflection coefficient. (c) Radiation patterns.

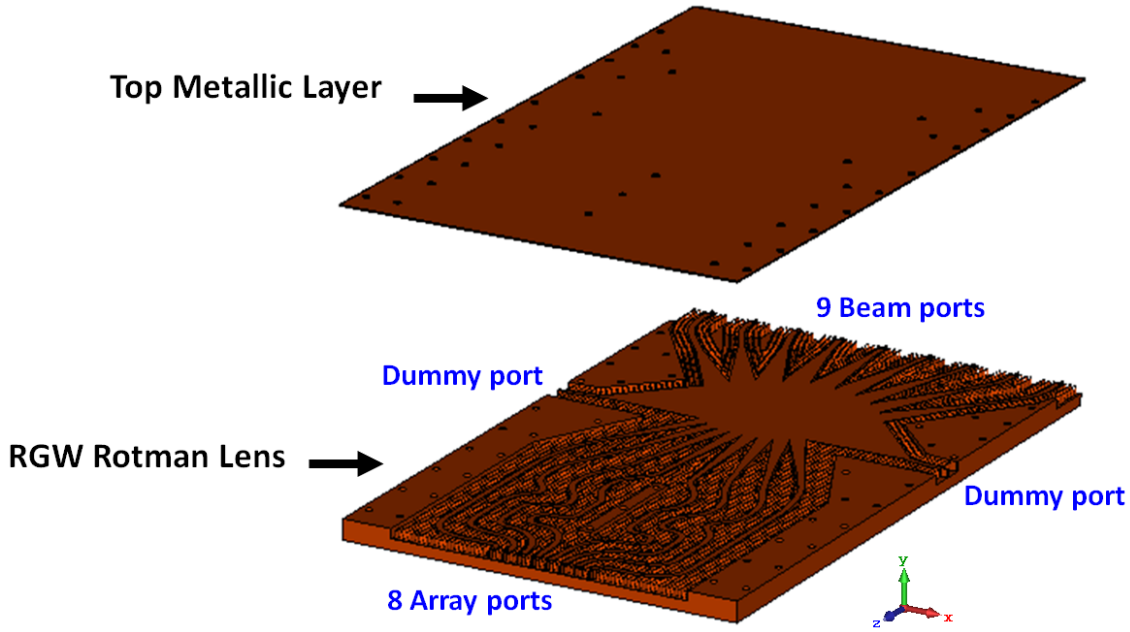

Figure 5.11: The proposed 9×8×2 RGW Rotman lens.

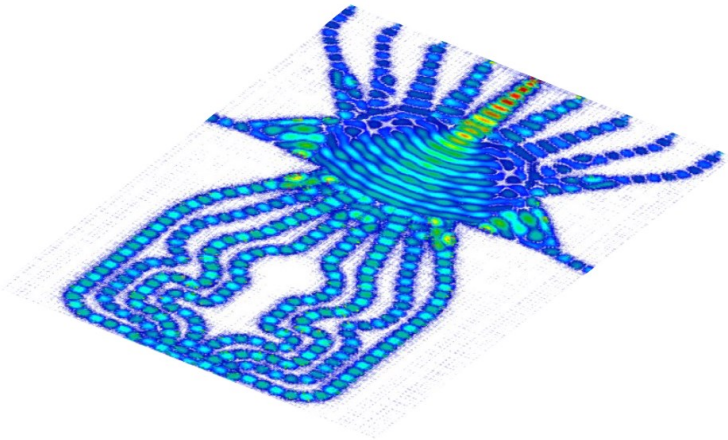

Figure 5.12: The electric field distribution in the simulated proposed RGW Rotman lens with smooth curved lines.

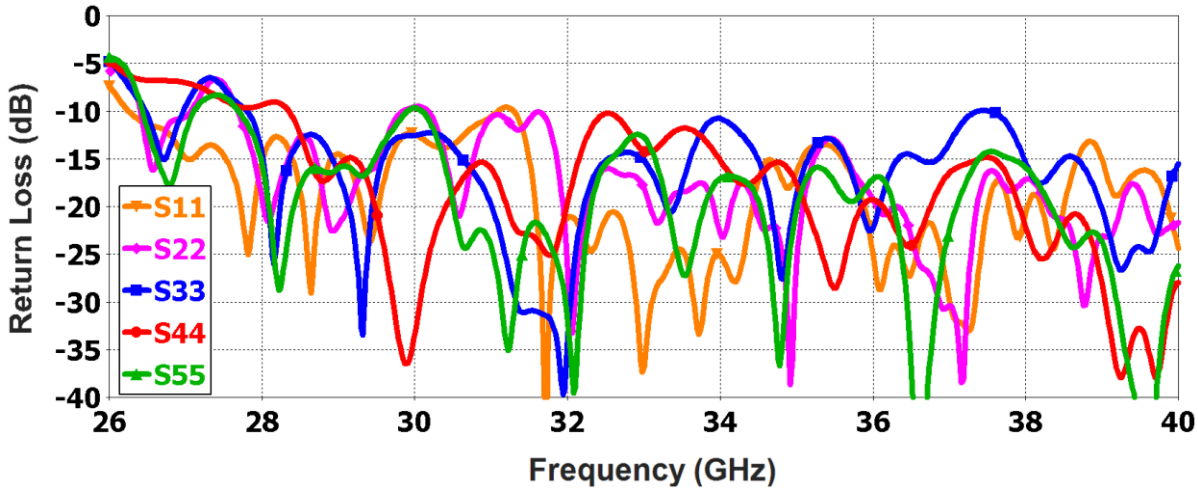

(a)

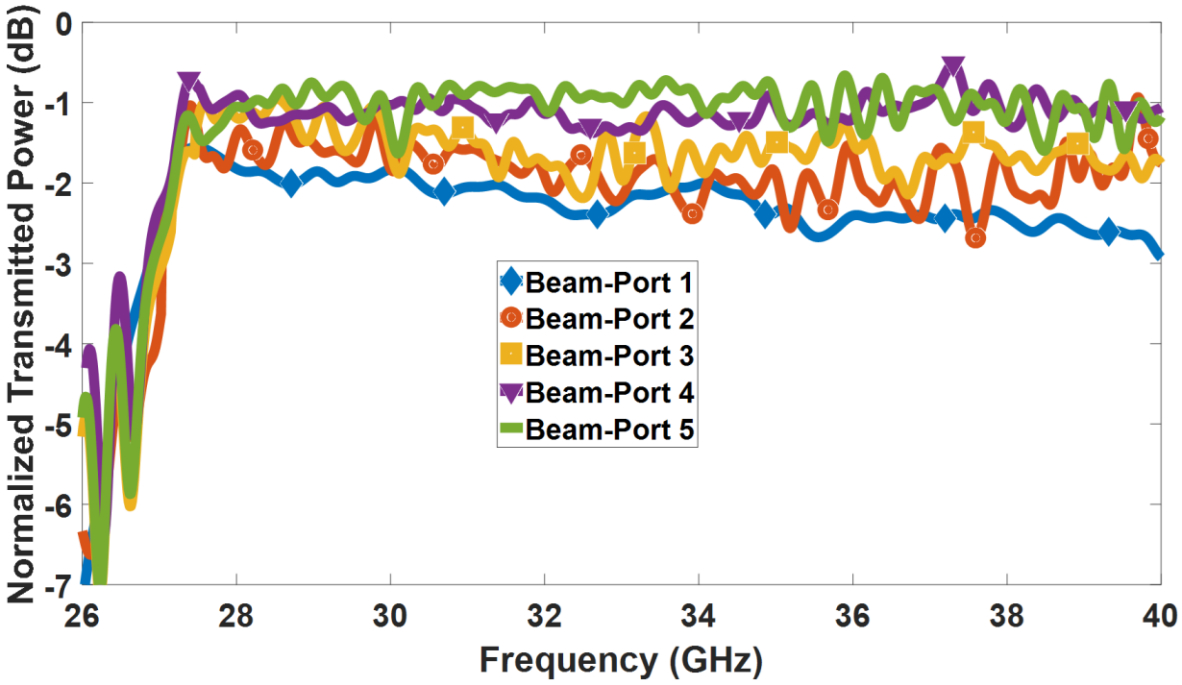

(b)

Figure 5.13: Simulated S-parameters of RGW Rotman lens: (a) Reflection coefficients magnitude of the beam ports. (b) Normalized transmitted power of the beam ports. The rest of the ports are not reported for symmetry reason.

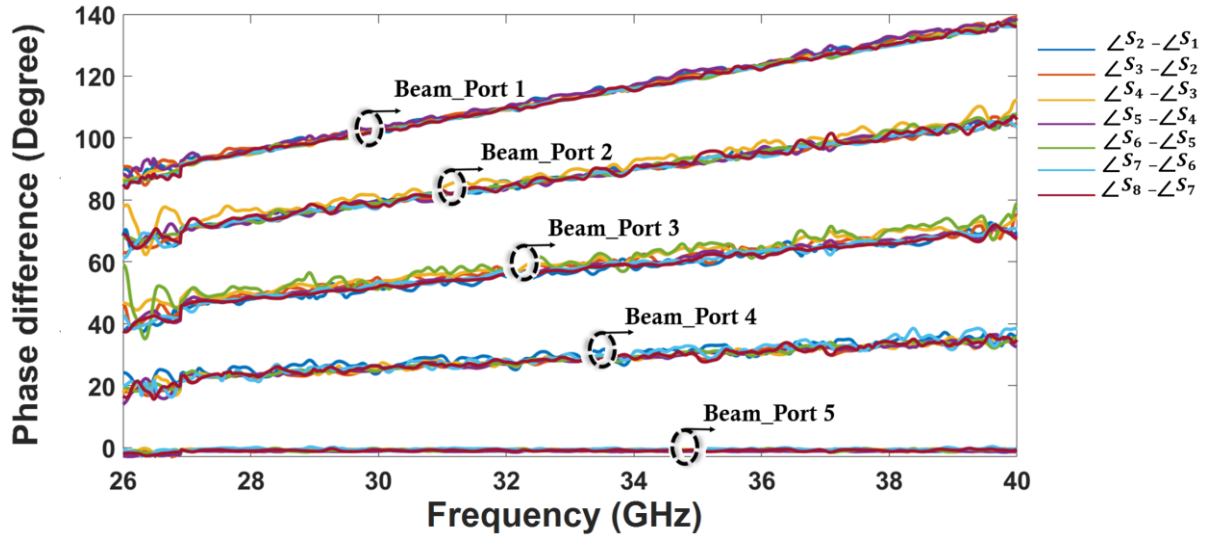

Figure 5.14: Simulated phase performance of the proposed Rotman lens. Each bundle denotes the variation of the phase progression in the array antenna elements with the frequency corresponding to one beam port excitation. Each color represents the phase difference between a pair of adjacent array ports. The rest of the ports are not reported for symmetry reason.

5.4.1.4 RGW Rotman Lens-Based BFN

Eight Quasi-Yagi antennas are integrated with the proposed RGW Rotman lens as shown in *Figure 15*. The overall structure consists of three main parts. The first part is the RGW Rotman lens. the second part is the antenna array layer, which contains the array elements in the frontend along with the MSL to RGW transition section and the input ports in the backend. The last part is the ground layer on top of an air-gap. The main beam points at nine different angular directions, as shown in *Figure 16* covering the range of ± 40º. The beam directions are uniformly distributed at ± 40º, ± 30º, ± 20º, ± 10º, and 0º. The maximum achieved simulated realized gain is 15.2 dBi at 37 GHz for the center beam. The radiation patterns show a gain drop beyond 3dB *BW* at for frequencies above 37 GHz due to the single antenna element's 3dB *BW*, as explained previously in section A.

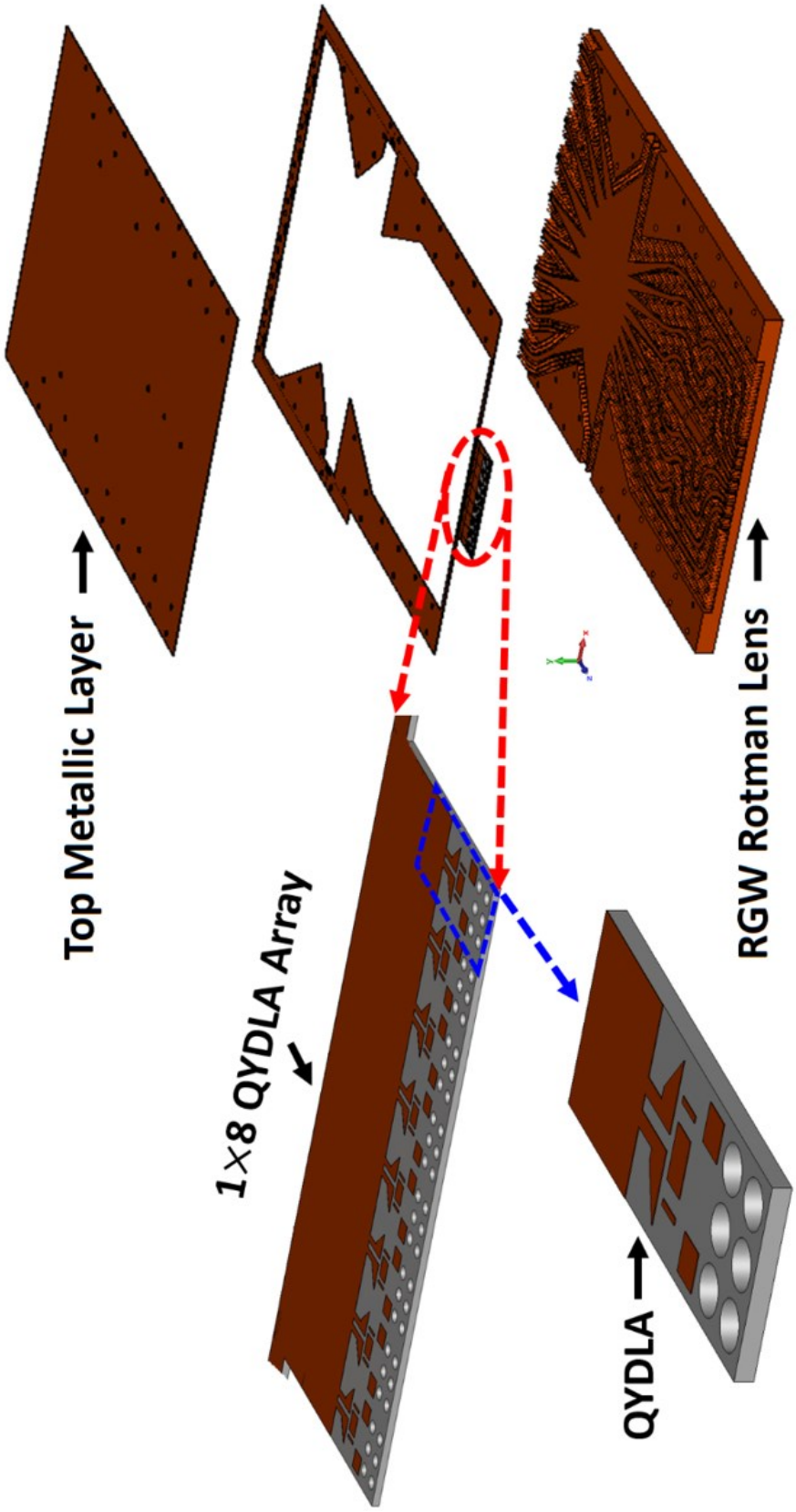

Figure 5.15: The proposed RGW Rotman lens-based BFN.

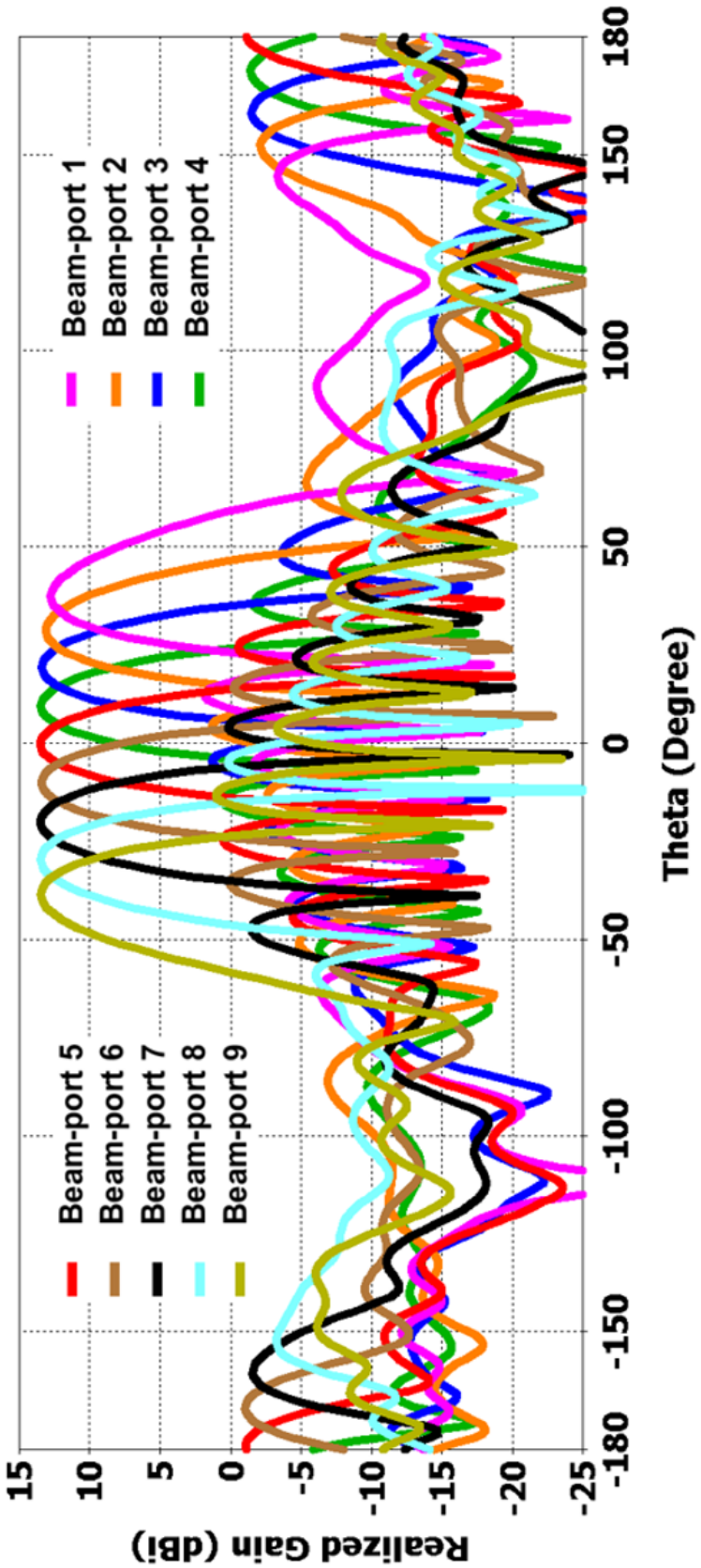

Figure 5.16a: Simulated radiation patterns of the proposed RGW Rotman lens-based BFN at 28 GHz.

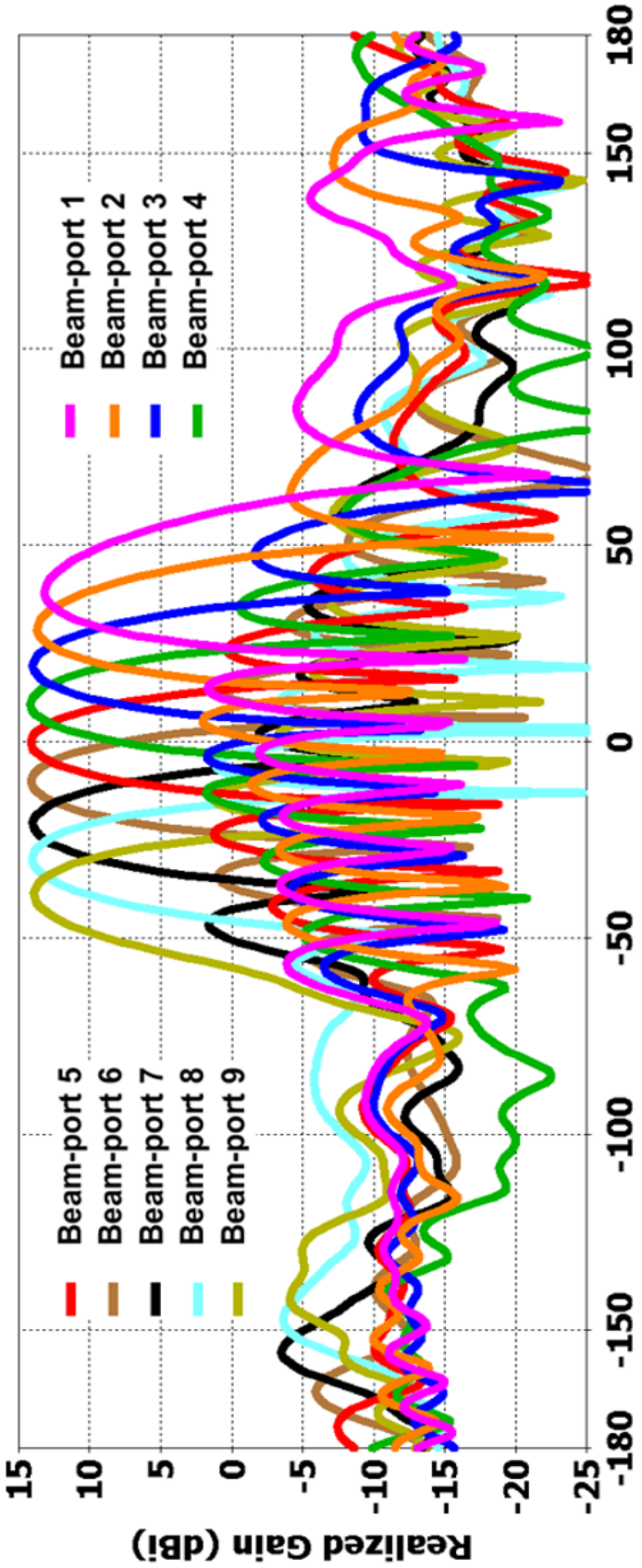

Figure 5.16b: Simulated radiation patterns of the proposed RGW Rotman lens-based BFN at 30 GHz.

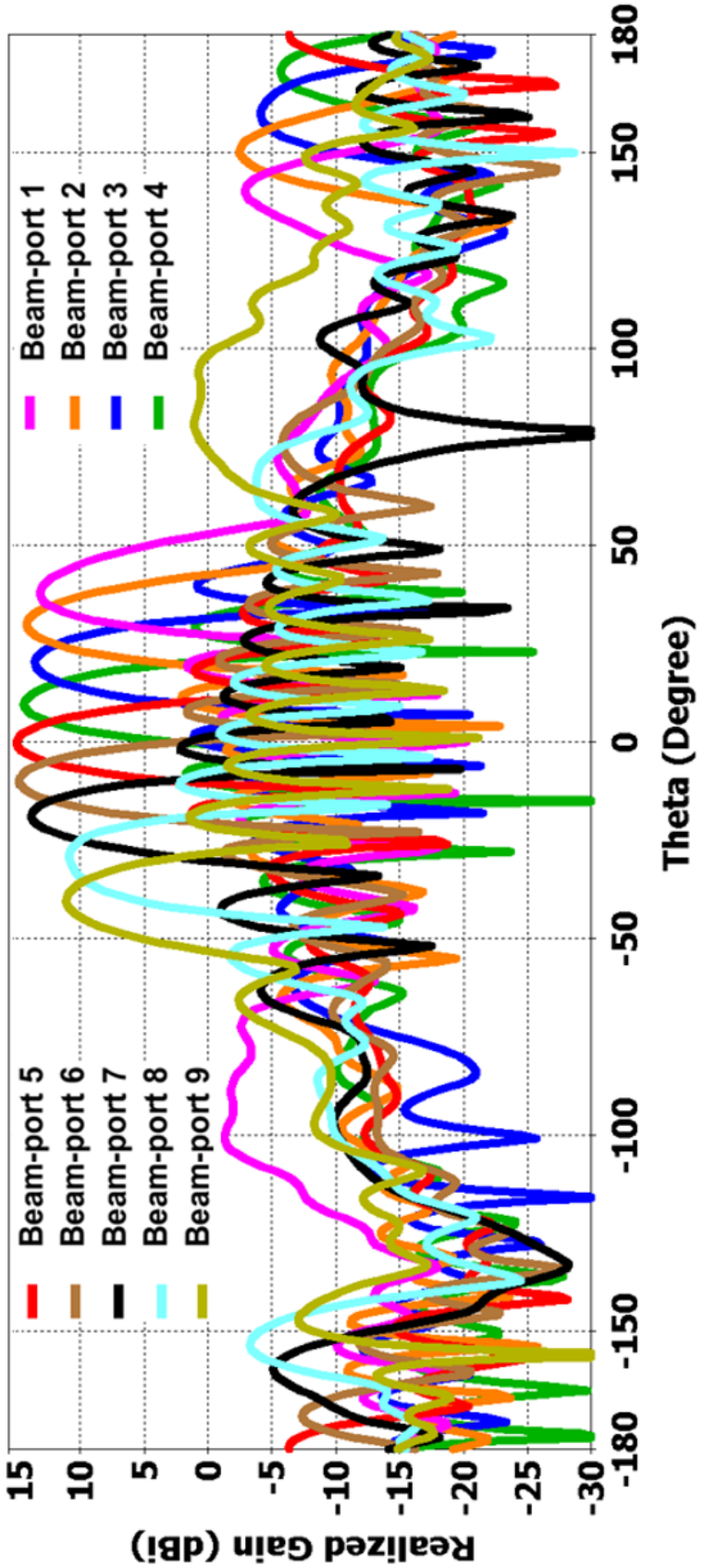

Figure 5.16c: Simulated radiation patterns of the proposed RGW Rotman lens-based BFN at 38 GHz.

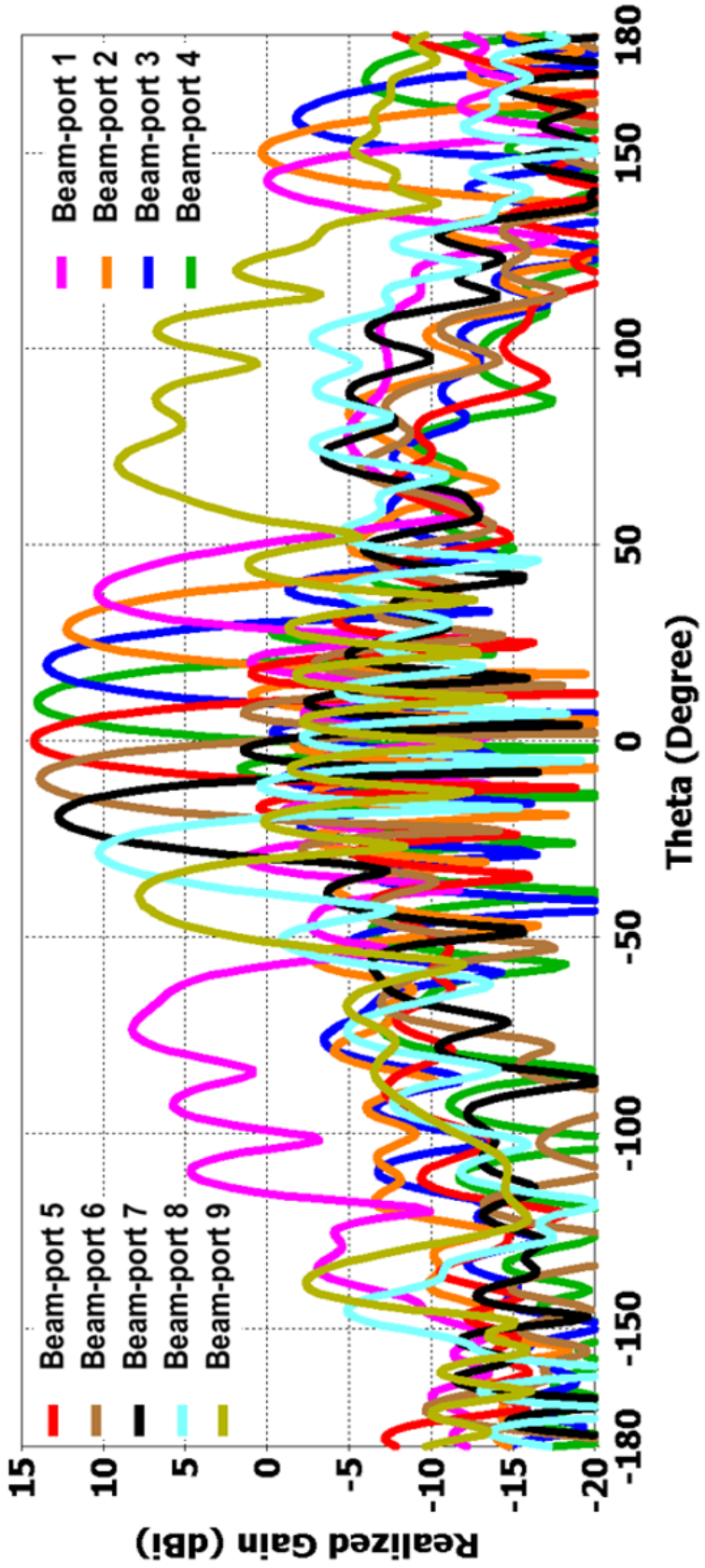

Figure 5.16d: Simulated radiation patterns of the proposed RGW Rotman lens-based BFN at 40 GHz.

5.4.2 PRGW Rotman Lens-based BFN

5.4.2.1 Microstrip Line to PRGW Transition

Connecting the PRWG Rotman lens to standard 50 Ω connectors, can be done by using MSL to RGW transition section discussed in the previous subsection and shown in *Figure 5.17a*. It can be seen that the transition section has good impedance matching ($|S_{11}|$<-10 dB) in the entire operational bandwidth as depicted in *Figure 5.17b*.

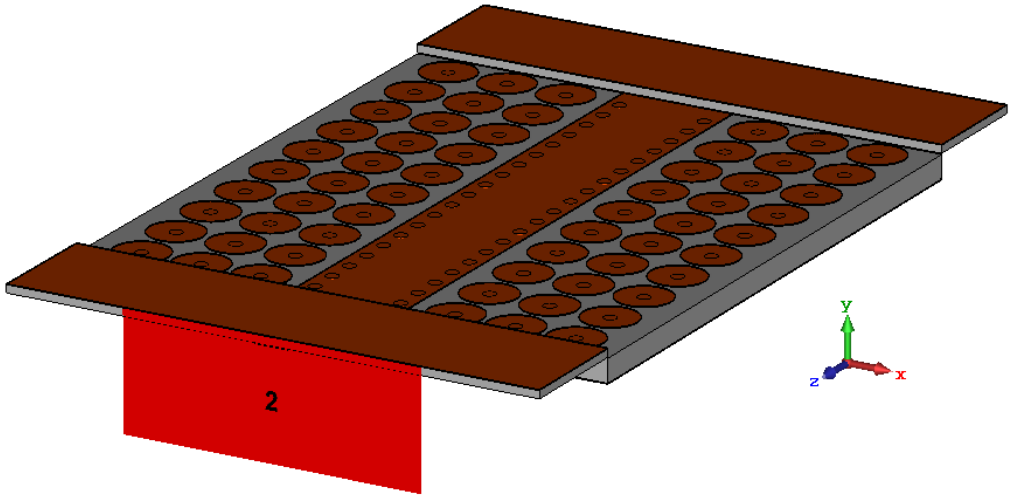

(a)

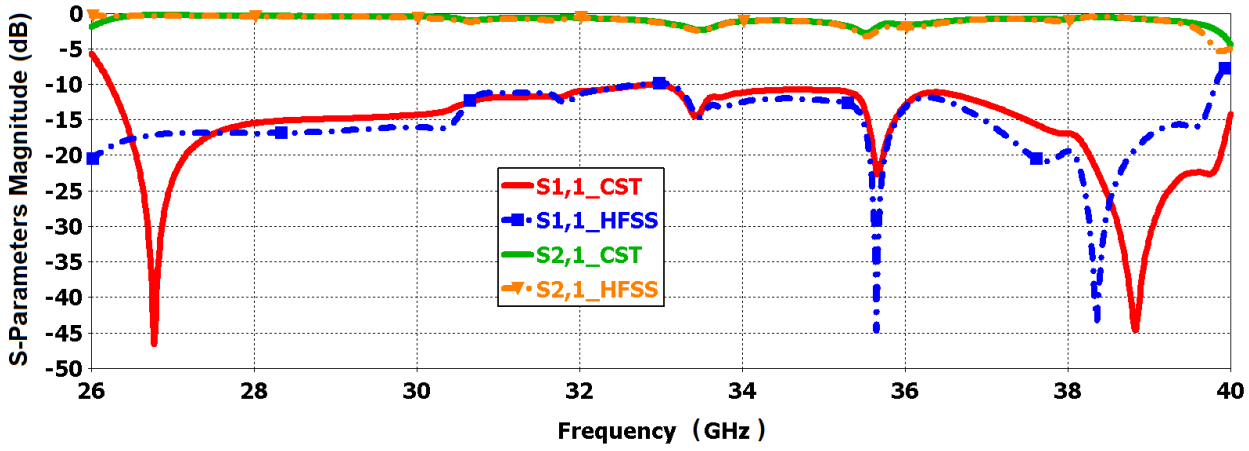

(b)

Figure 5.17: MS to PRGW transition: (a) 3D structure. (b) Simulated S-parameters.

5.4.2.2 PRGW Rotman Lens Design

Rotman lens with eight array ports was simulated in the PRGW technology as shown in *Figure 5.18*. The lens was designed for optimum amplitude and phase error performance in the frequency band 26.5-40 GHz. The original design requires five beam ports, to steer the beam within a maximum scanning range of ± 30º, and a minimum array element spacing of $0.5\lambda_0$.

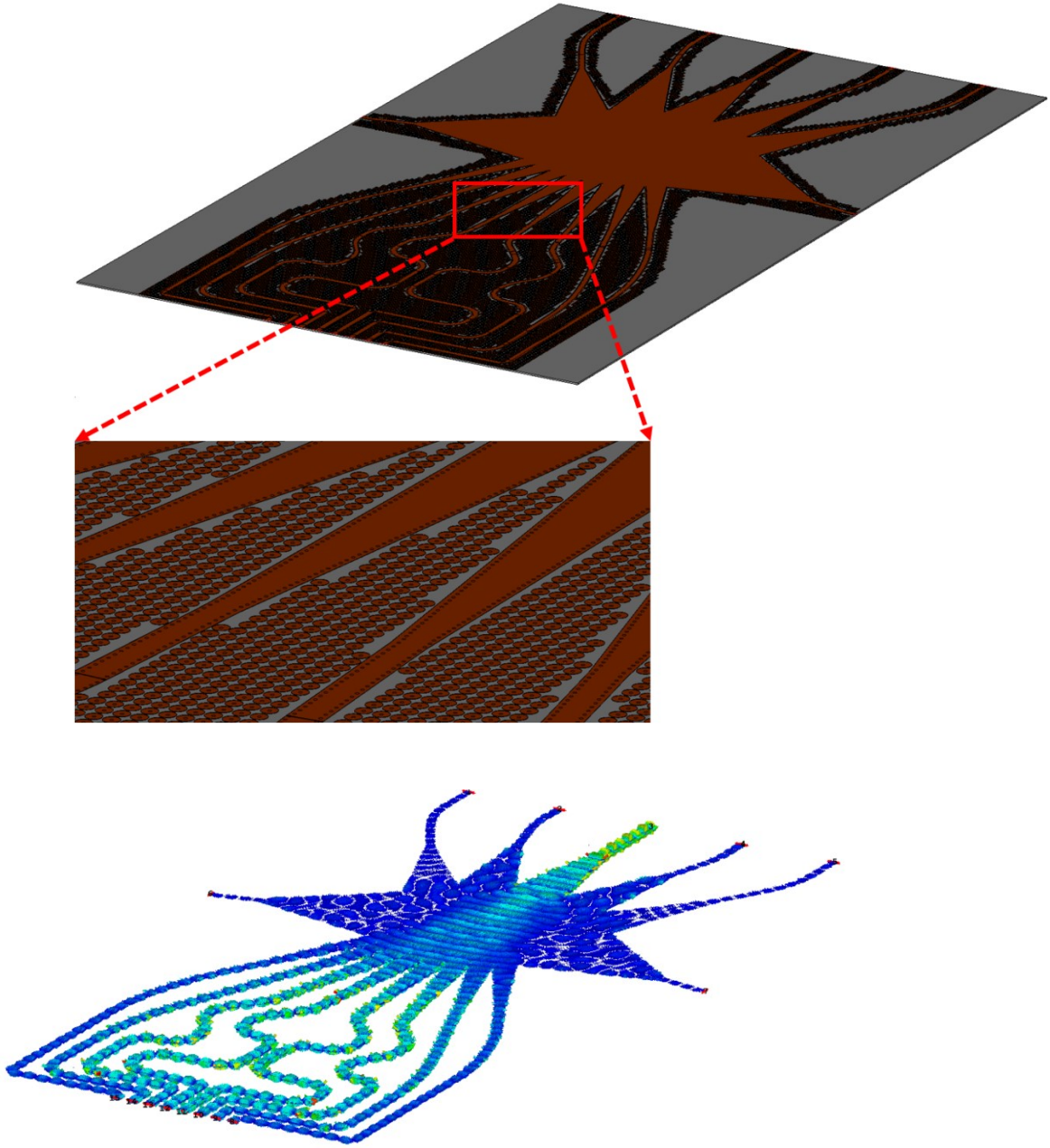

Figure 5.18: Simulated Rotman lens design with PRGW technology.

It can be seen that the propagating mode in the parallel plate region is pure TEM and the mushroom surface efficiently prevents the wave propagation beyond the printed ridge area as the array ports' transmission lines are isolated from each other. *Figure 5.19* shows the performance of the PRGW Rotman lens in terms of S-parameters phase of the array-ports and the reflection coefficients of the beam ports. All of the beam ports are matched with better than −10 dB. The phase distributions across the array-ports show a linear behavior as depicted in *Figure 5.19a*. The maximum phase error is ±6° for beam port 2. This can be explained by non-focal points might have more phase error than focal points which theoretically have zero phase error.

The significant performance improvement achieved using the PRGW technology compared to the MS Rotman lens is the power level at the array ports. The normalized transmitted power of the PRGW system indicate that about 1 dB improvement of the insertion loss, which mainly represents the dielectric loss of the MS Rotman lens.

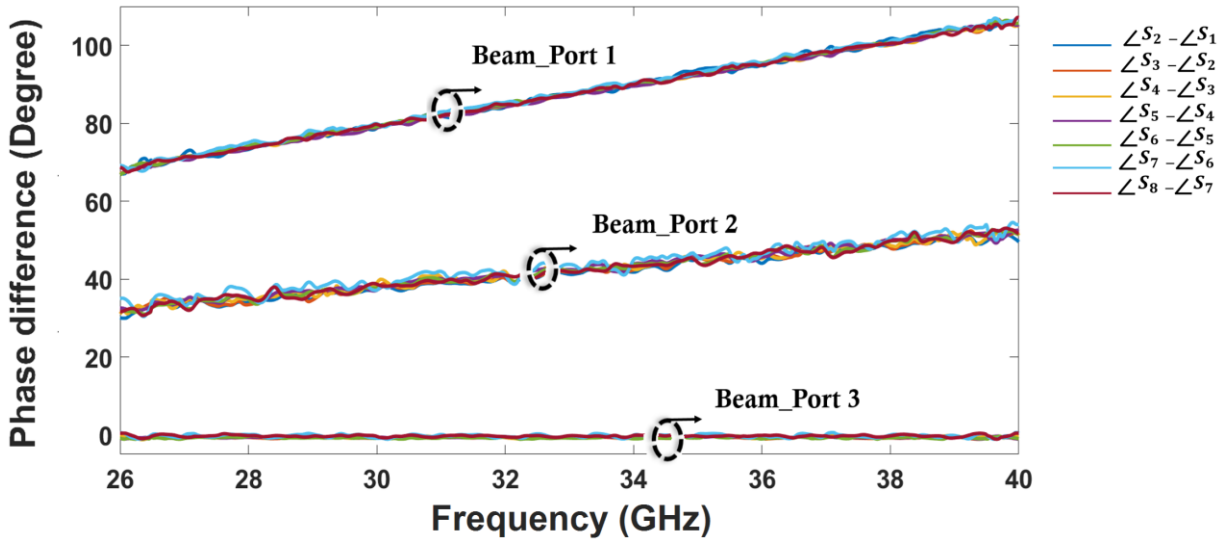

(a)

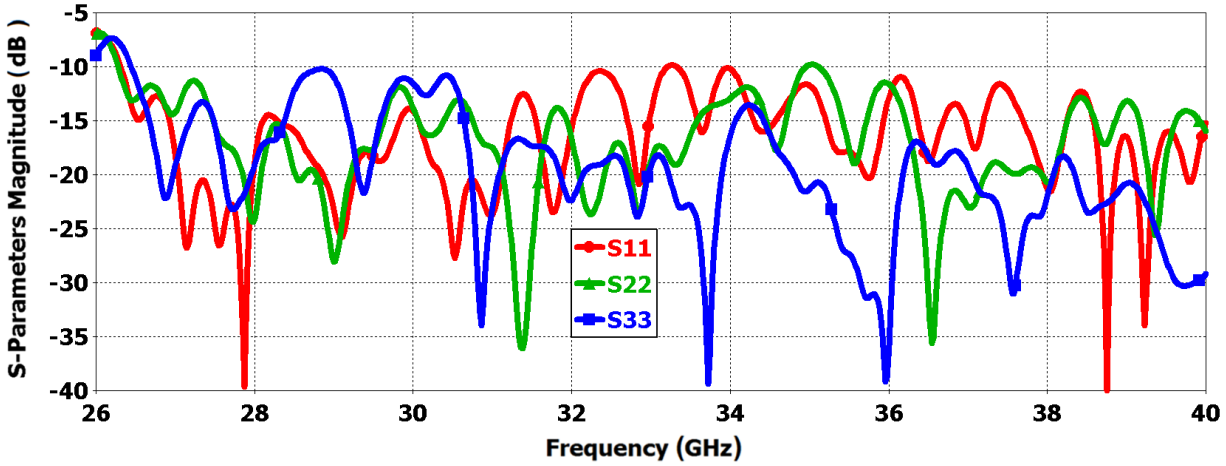

(b)

Figure 5.19: Simulated S-parameters of the proposed PRGW Rotman lens: (a) The Phase performance of the proposed Rotman lens. (b) Reflection coefficients magnitude at the beam ports.

5.5 Prototyping and Experimental Results

The RGW Rotman lens, 1×8 Quasi-Yagi antenna array, and the MS-to-RGW transition sections are shown in *Figure 5.20*. To ease the RGW Rotman lens fabrication and avoid the extremely cost of the CNC full metal RGW Rotman lens, the lens is made with the metalized 3D-printing technique. The antenna and the excitation of the RGW, described in the previous sections, are manufactured using PCB technique. The measured reflection coefficients at the beam ports are plotted in *Figure 5.21*, while the radiation patterns are shown in *Figure 5.22*. All reflection coefficients are lower than -10 dB over the (27.5-40) GHz band. The antenna scanning range is about $\pm$39.5º. The radiation patterns, measured and simulated, for selected frequencies between 27.5 and 40 GHz in E-plane are provided in *Figure 5.*22. The maximum measured gain is 14.95 dBi at 37 GHz. The simulations and measurements are in a good agreement, despite the slightly higher SLL observed experimentally for some beams. However, considering the complexity of the beamformer stack-up (*Figure 5.*20) and fabrication constraints (the clearance between adjacent holes is 0.254 mm); the misalignment between MS transmission lines and the matching section in the RGW lines, and the fabrication tolerance, the results are quite satisfactory.

The proposed RGW beamforming network is compared to some relevant works as summarized in *Table 4.3*. It exhibits a reasonable gain level and scanning capabilities, which have been verified experimentally. The proposed system here has a wider scanning range (±39.5°) than [73] of (±20°) maximum steering angle. Also, machining of such device in the mm-waves band is exceptionally costly, while the proposed system in this thesis (3DP-RGW) is much lower cost than the metal RGW of [73]. The PRGW of [74] has similar scanning range as the proposed 3DP-RGW in this work. However, the reported amplitude variation between array ports of [74] is (-10 dB), which indicates a poor amplitude performance. Besides, to the best authors' knowledge, the physical implementation and measurement results of mm-wave RGW and PRGW Rotman lens are not reported yet in the open literature. [15] presents a beamforming network of 100% FBW, which is really a quite broadband compared to 38% of the proposed system in this work, but it has a lower scanning range (±30°) and lower gain (9-13 dBi) compared to the proposed beamforming network in this work. In addition, the beamforming network of [15] is proposed for the band 6-18 GHz, and scaling it to mm-wave band might result in some expected gain and bandwidth limitations.

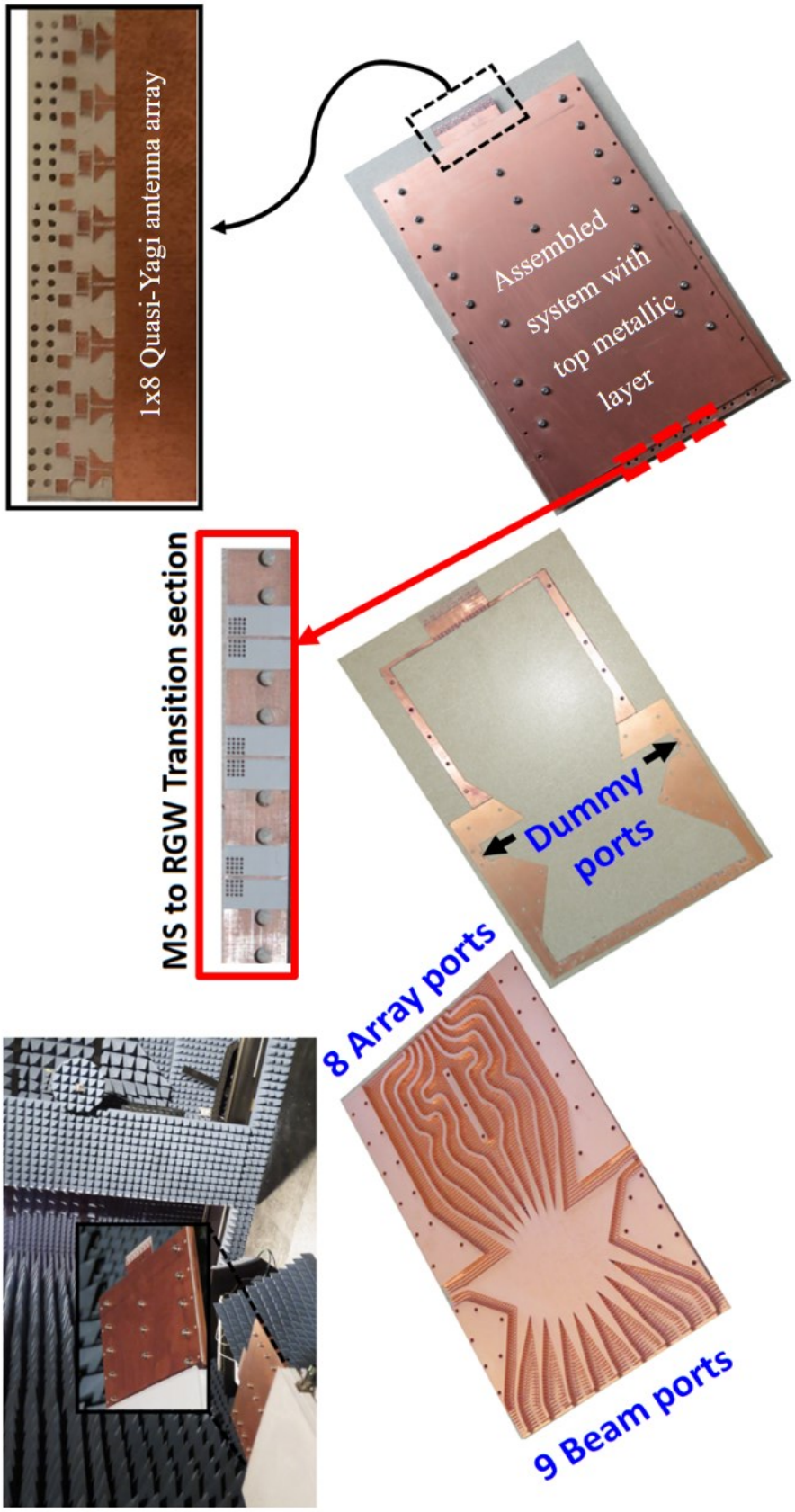

Figure 5.20.: Photographs of the proposed RGW Rotman lens-based BF prototype: Top and Bottom views of different layers. Measurement setup of the radiation patterns at the top left corner.

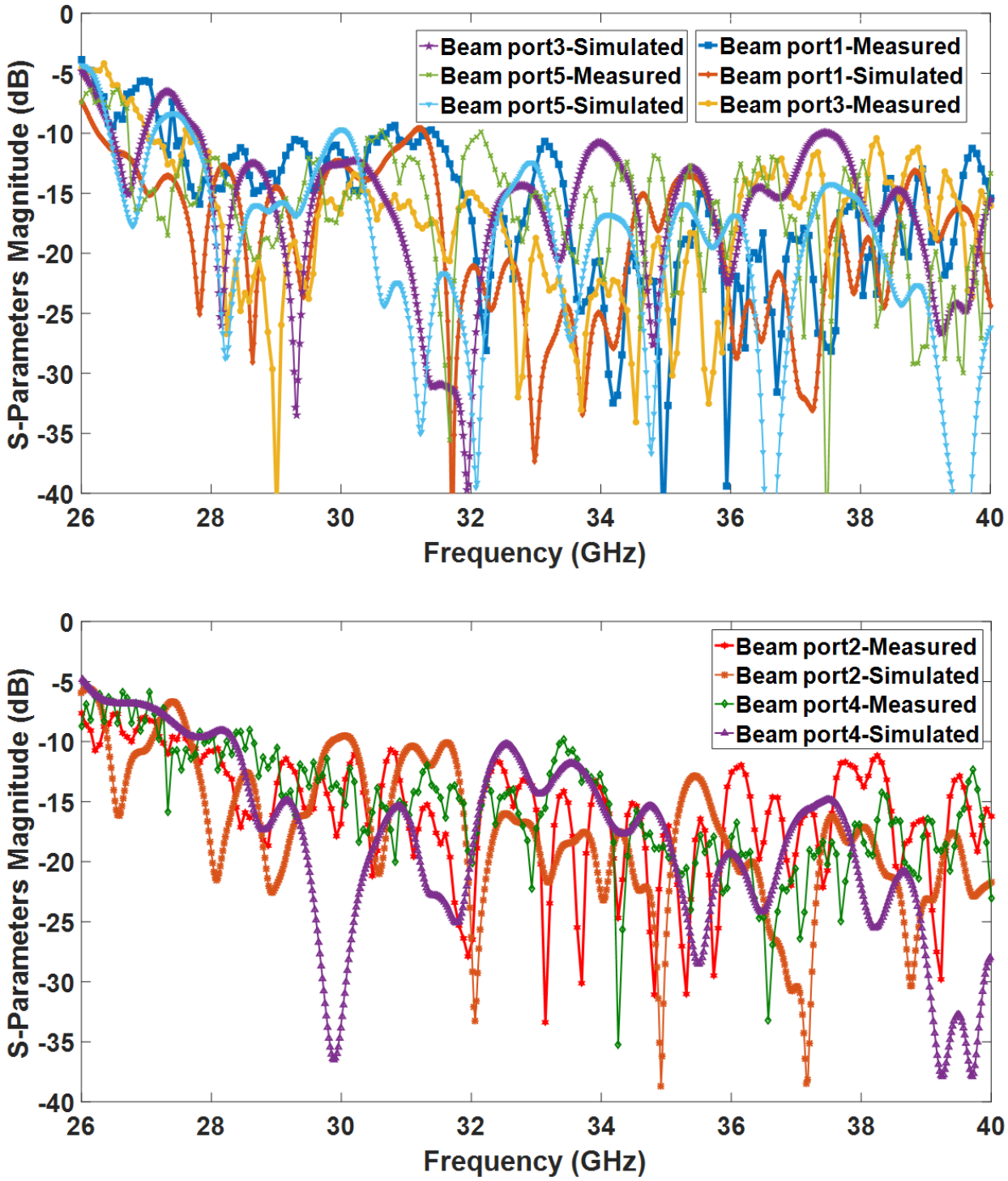

Figure 5.21: Measured Reflection coefficients magnitude of the beam ports. The rest of the ports are not reported for symmetry reason.

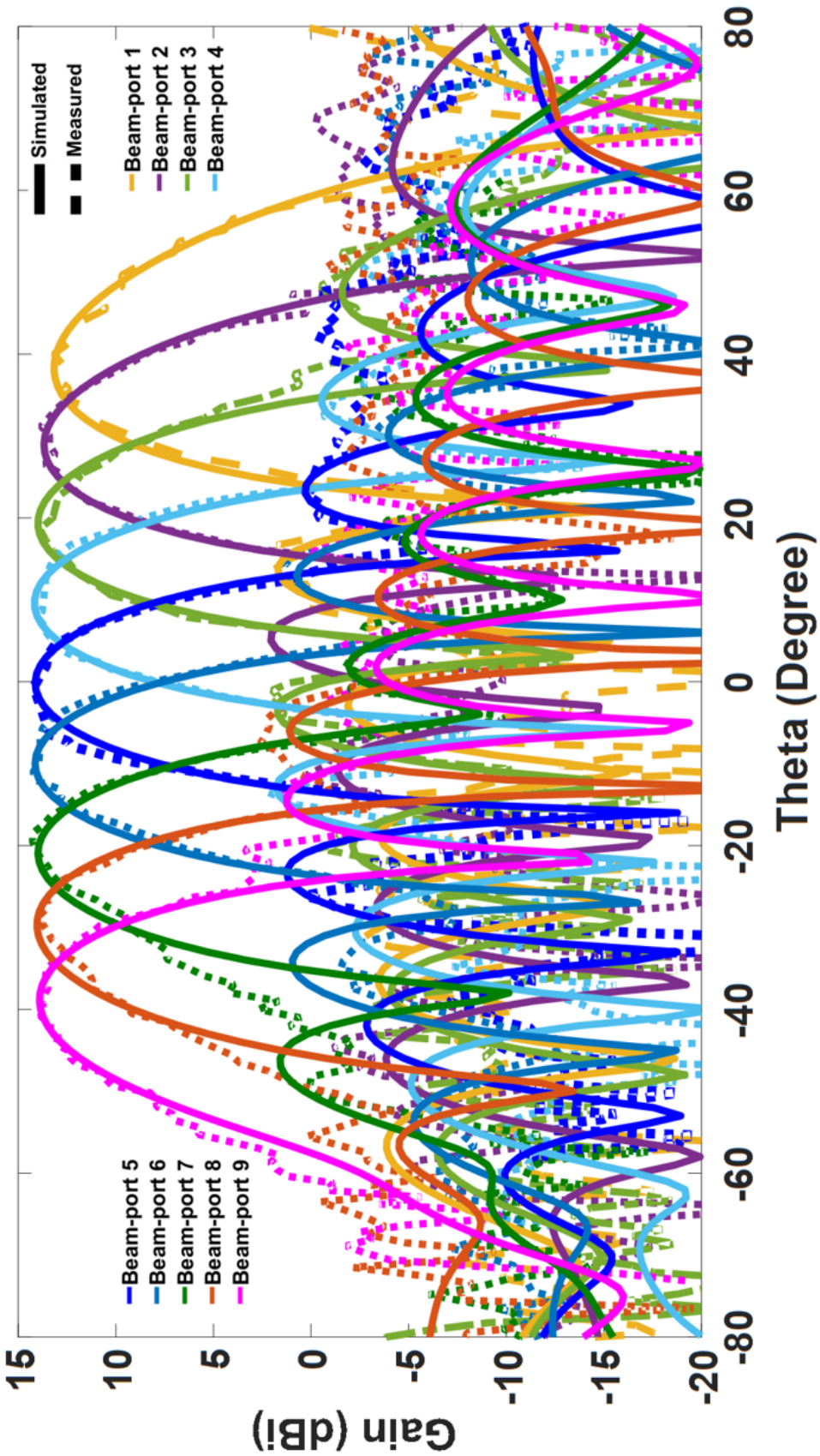

Figure 5.22a: Radiation patterns of the proposed RGW Rotman lens-based BFN at 30 GHz.

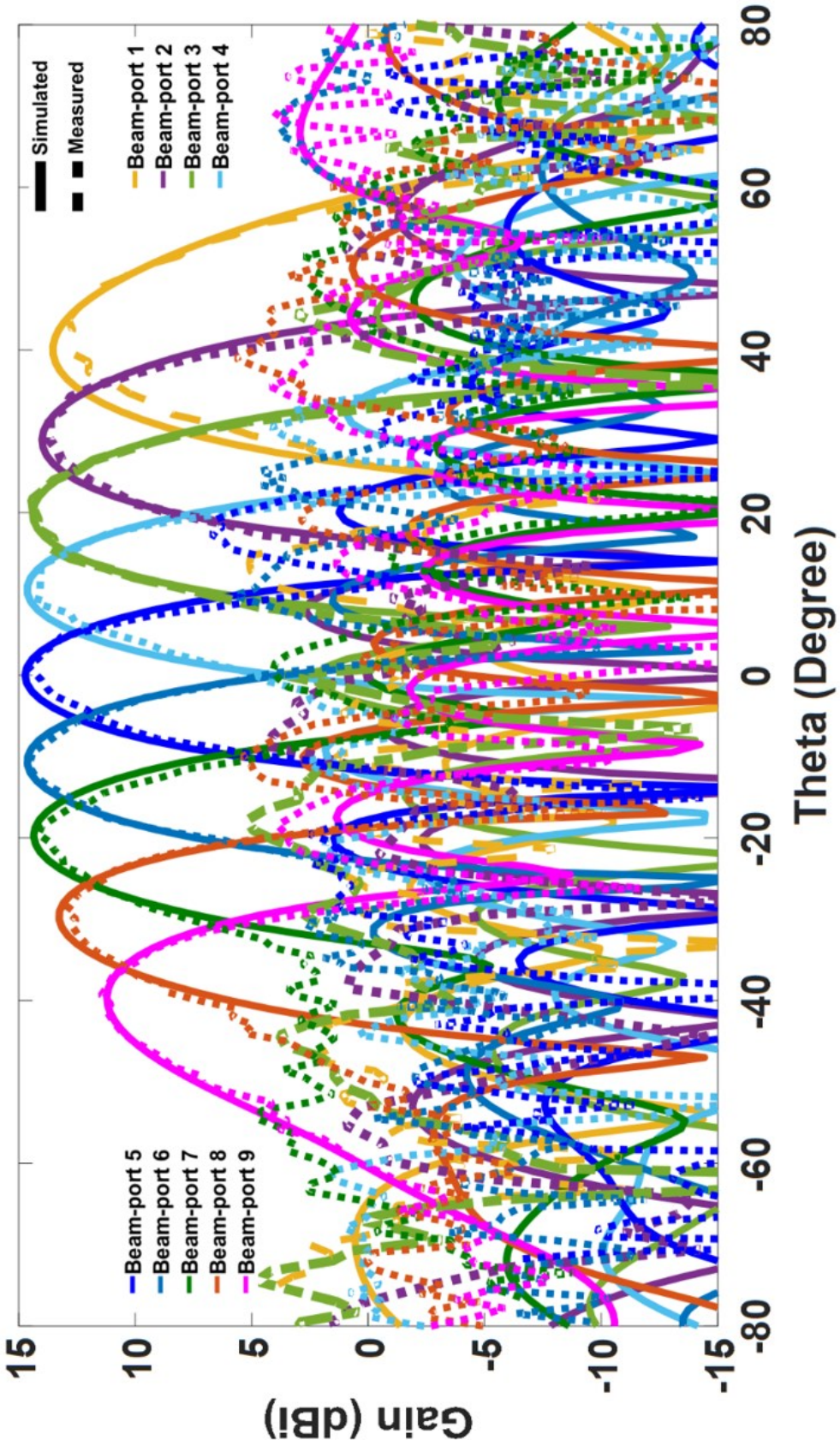

Figure 5.22b: Radiation patterns of the proposed RGW Rotman lens-based BFN at 34 GHz.

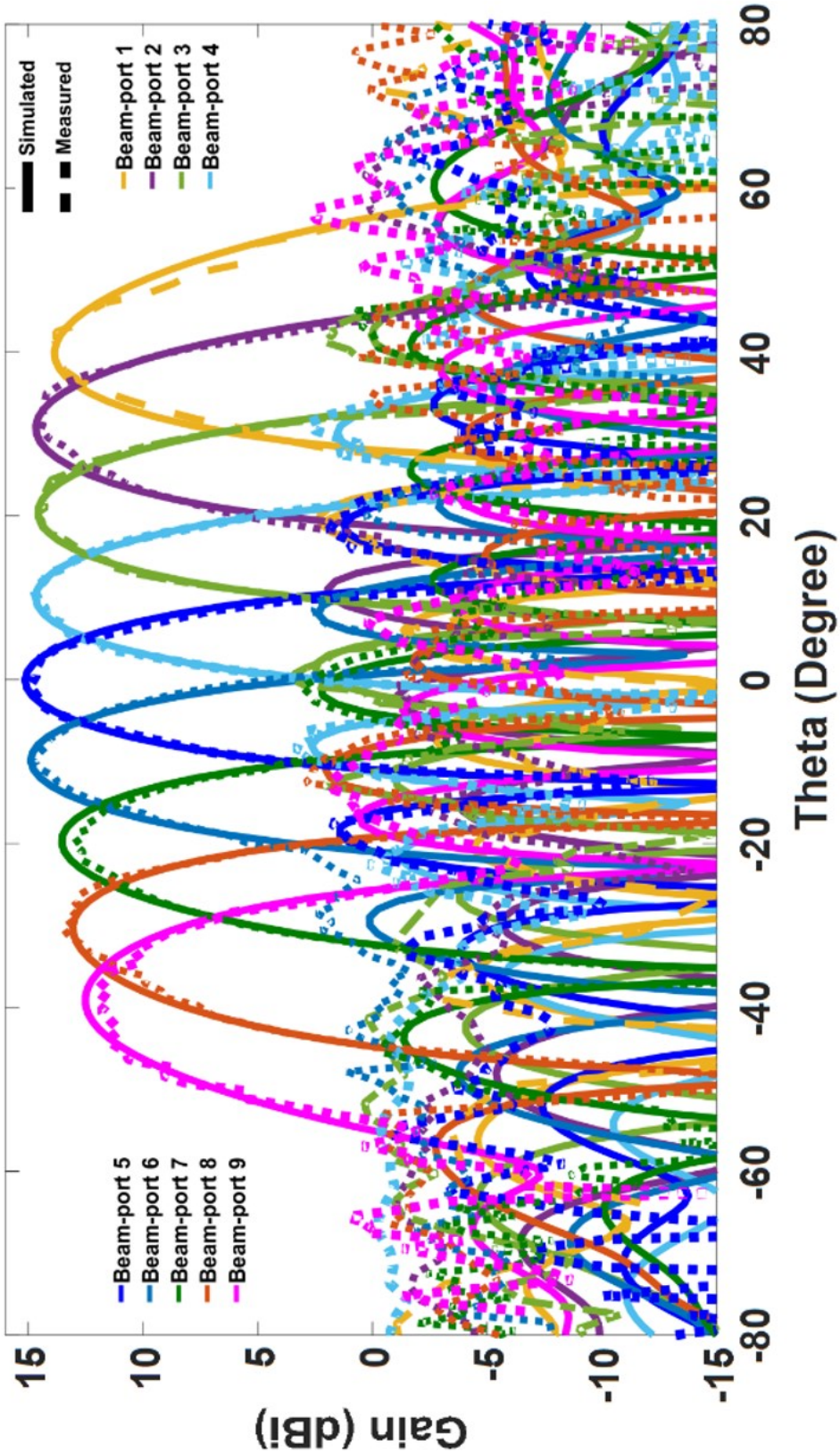

Figure 5.22c: Radiation patterns of the proposed RGW Rotman lens-based BFN at 37 GHz.

5.6 Summary

An analog Rotman lens-based beamforming network (BFN) using RWG technology, along with the excitation and the antenna array elements was designed, simulated, manufactured, and measured. The proposed system was realized using the metallized 3D-Printing technology, in order to reduce the implementation cost of the full metal RGW Rotman lens. The measured results demonstrate that the system scan range equals $\pm$39.5º in the band 27.5-37 GHz decreases to 30º in the band 37-40 GHz .The antenna bandwidth for VSWR < 2 is larger than 38% and is limited by the bandwidth of the radiating part and its beamwidth as well. Aiming to reduce the implementation cost, the printed version of the RGW (PRGW) is proposed and simulated. The PRGW Rotman lens-based BFN shows a good amplitude and phase error performance in the band 26.5 GHz to 40 GHz. The maximum phase error was 6º with about 1 dB insertion loss improvement compared to MS Rotman lens-based beamforming network were achieved. The performance of the proposed beamforming network makes it very attractive for potential 5G applications such as the advanced MIMO and hybrid beamforming networks.

CHAPTER 6: Conclusion and Future Work

6.1 Conclusion

This thesis dealt with two main requirements in the mm-wave band. As high gain antennas are among the essential requirements of 5G, different millimeter antenna structures and configurations were studied. For the advantages of low profile, lightweight, ease of fabrication and installation, high directivity, and high radiation efficiency, the Quasi-Yagi antenna and dielectric lens were selected to form a new antenna of enhanced gain and bandwidth. The enhancement is achieved by, based on subwavelength gratings and effective medium theories, treating a thin dielectric slab waveguide (DSW) to ensure a single mode of operation. The first part of this work proposed a new type of Quasi-Yagi antenna that showed a promising behavior. Two different variants of the dielectric lens have been presented: parallel line dielectric corrugation (PLDC) and ray combiner dielectric lens (RCDL). These lenses enhanced the gain and the impedance matching bandwidth of the ordinary Quasi-Yagi antenna, which was fabricated with the printed circuit board (PCB) technology. Then, a brief and straightforward design methodology for designing these types of antennas was provided. The characteristics of the new Quasi-Yadi dielectric lens Antenna (QYDLA) made it suitable for a wide range of millimeter wave applications.

The prototype's experimental results showed a gain improvement compared to the conventional DSW lens. The proposed antenna exhibits a good impedance matching better than -15 dB in the band 24-40 GHz more than 17 GHz (>42 % FBW). Measured cross-polarization level is better than -22 dB. The antenna measured gain ranges between 14 to 15.2 dB over the operating frequency band 30-38 GHz. Therefore, this antenna can be considered as a competitive planar high gain antenna for 5G applications. It can be scaled to 60, 77, or 94GHz for 5G wireless point-to-point, point-to-multipoint backhaul communication systems, and automotive radar.

The second major part of this thesis has been dealing with the beamforming networks because the nature of mm-wave propagation lends itself to a beamforming structure, which is where antenna arrays are required to obtain the necessary link budget. Therefore, an analog beamforming network (BFN)—using a compact-size Rotman lens—feeding eight Quasi-Yagi antenna array for 5G and mm-wave applications was presented. The proposed system was fabricated using standard planar and low-cost processing PCB technology in the 26–40 GHz band. The antenna and the beamforming network design methodology was described in detail, and its performance was

experimentally confirmed. The system exhibits good impedance matching and beam steering capability. A scanning range of ±40º was achieved, which is better than most of the relevant systems. The BFN bandwidth ($|S_{11}| < -10$ dB) is greater than 42% and is limited by the single antenna element bandwidth. The performance and compactness of the proposed system qualify it for a wide range of potential mm-wave communication systems, such as the advanced multiple-input multiple-output (MIMO) and hybrid beamforming networks.

The last part of this thesis addresses the implementation of the proposed analog Rotman lens-based BFN using an RGW guiding structure. The fascinating characteristics of the RWG made it suitable for mm-wave applications because only air and metal are used—that is, to ensure the propagating mode is a quasi-TEM inside an air gap. This approach resolved a major problem associated with the standard guiding structures—such as microstrip (MS) technology—where the dielectric losses increase with the increase of frequency. The simulation and measurement results showed a good performance in terms of the amplitude and the phase along with 30°- 40º scanning range. The measured reflection coefficient ($|S_{11}|$) performance is better than -10 dB for the frequency range between 27.5 – 40 GHz (38% FBW). The scanning range of the propose system is ±39.5º to approximately ±30º for higher frequencies above 37 GHz because of limitations of 3 dB beamwidth (*BW*) of the single element. However, fabrication of the metallic RGW Rotman lens is remarkably complex and costly as compared to other technologies at mm-wave frequencies. Therefore, the printed ridge gap waveguide (PRGW) provides an alternative solution that is easy to fabricate and cost-effective.

Lastly, a PRGW Rotman lens-based BFN was designed and simulated as a proof of concept for a solution that combines the ease of fabrication with the microstrip technology and the advantage of the wave propagation in the air only as of the metallic RGW. The simulation results showed that the PRGW Rotman lens was capable of steering the beam within ±30º with a maximum phase error of ±6° and about 1 dB insertion loss improvement compared to MS Rotman lens. This result therefore concludes the set objectives of the thesis.

6.2 Future Work

The work in this thesis can be furthered by the integration with Microelectromechanical systems (MEMS). The monolithic fabrication of the BFN together with these tunable components reduces drastically the dielectric losses associated with the PCB version of the BFN. RF-MEMS switches could be used at both ends of Rotman lens so that attenuated signals, due to the dielectric substrate, are detected and regenerated. In other words, the Rotman lens-based BFN will function as a trigger for repeaters connected to RF-MEMS switches. Furthermore, the idea of using Rotman lens-based BFN can also be developed with the help of digital signal processing in order to cover 360º rather than the 3 dB beamwidth (BW) of a single antenna element. The required coverage area is divided into sectors; each sector has an antenna array of N elements which are connected to a switch via equal length transmission lines. The switch is connected to the array ports of the Rotman lens-based BFN. This development would improve overall system efficiency—that is, the 360º scanning could be achieved with the same number of beam ports and, consequently, the same number of RF chains.

References

[1] Cisco, Visual Networking Index. [Online]. Available: https://www.cisco.com/c/en/us/solutions/collateral/service-provider/visual-networking-index-vni/white-paper-c11-741490.html#_Toc529314172 , last access on Nov. 17, 2019.

[2] T. S. Rappaport *et al*., "Millimeter wave mobile communications for 5G cellular: It will work!," *IEEE Access*, vol. 1, 2013, pp. 335-349. doi: 10.1109/ACCESS.2013.2260813

[3] First mm-wave system, [Online]. Available: https://ethw.org/Milestone-Nomination:First_Millimeter-wave_Communication_Experiments_by_J.C._Bose,_1894-96 ,last access on Nov. 19, 2019..

[4] M. Marcus and B. Pattan, "Millimeter wave propagation: spectrum management implications," *IEEE Microwave Magazine*, vol. 6, no. 2, June 2005, pp. 54-62. doi: 10.1109/MMW.2005.1491267

[5] 5G candidate frequency bands, [Online]. Available: https://www.fcc.gov/document/fcc-proposes-steps-towards-auction-37-ghz-39-ghz-and-47-ghz-bands-0 , last access on Nov. 17, 2019

[6] 5G frequency ranges. Available [Online].: https://www.3gpp.org/ftp/Specs/archive/38_series/38.101-1/ , last access on Nov. 17, 2019.

[7] C. Jacob, K. Sabith, S. Prabhakaran, N. Bhaskaran, "Planar printed quasi Yagi antenna- a study," *International Journal of Advanced Research in Electrical, Electronics and Instrumentation Engineering*., vol. 4, Issue 7, July 2015, doi:10.15662/ijareeie.2015.0407088 6562

[8] C. Tsokos *et al*., "Analysis of a multibeam optical beamforming network based on Blass matrix architecture," in *Journal of Lightwave Technology*, vol. 36, no. 16, Aug. 2018, pp. 3354-3372. doi: 10.1109/JLT.2018.2841861

[9] A. Rahimian, "Investigation of Nolen matrix beamformer usability for capacity analysis in wireless MIMO systems," *Asia-Pacific Conference on Communications (APCC)*, Denpasar, 2013, pp. 622-623. doi: 10.1109/APCC.2013.6766023

[10] J. Lian, Y. Ban, C. Xiao and Z. Yu, "Compact substrate-integrated 4 × 8 butler matrix with sidelobe suppression for millimeter-wave multibeam application," *IEEE Antennas and Wireless Propagation Letters*, vol. 17, no. 5, May 2018, pp. 928-932. doi: 10.1109/LAWP.2018.2825367

[11] Y. Cao, K. Chin, W. Che, W. Yang and E. S. Li, "A Compact 38 GHz multibeam antenna array with multifolded Butler Matrix for 5Ga," *IEEE Antennas and Wireless Propagation Letters*, vol. 16, 2017, pp. 2996-2999. doi: 10.1109/LAWP.2017.2757045

[12] Y. J. Cho, G. Suk, B. Kim, D. K. Kim and C. Chae, " RF Lens-embedded antenna array for mmwave MIMO: design and performance," *IEEE Communications Magazine*, vol. 56, no. 7, JULY 2018, pp. 42-48. doi: 10. 1109/MCOM.2018.1701019

[13] H. N. Chu and T. Ma, "An extended 4×4 Butler matrix with enhanced beam controllability and widened spatial coverage," *IEEE Transactions on Microwave Theory and Techniques*, vol. 66, no. 3, March 2018, pp. 1301-1311. doi: 10.1109/TMTT.2017.2772815

[14] P. Kildal, E. Alfonso, A. Valero-Nogueira and E. Rajo-Iglesias, "Local metamaterial-based waveguides in gaps between parallel metal plates," *IEEE Antennas and Wireless Propagation Letters*, vol. 8, pp. 84-87, 2009. doi: 10.1109/LAWP.2008.2011147

[15] K. V. Hoel, S. Kristoffersen, N. Jastram and D. S. Filipovic, "3D printed Rotman lens," *European Microwave Conference (EuMC)*, Nuremberg, 2017, pp. 125-128. doi: 10.23919/EuMC.2017.8230815

[16] H. Li, W. Hong, T. Cui, K. Wu, Y. Zhang and L. Yan, "Propagation characteristics of substrate integrated waveguide based on LTCC," *IEEE MTT-S International Microwave Symposium Digest, 2003*, Philadelphia, PA, USA, 2003, pp. 2045-2048 vol.3. doi: 10.1109/MWSYM.2003.1210562

[17] C. Free, Z. Tian, P. Barnwell, I. Robertson and C. Aitchison, "A new LTCC fabrication technology for planar millimeter-wave circuits," *Asia Pacific Microwave Conference. APMC'99. Microwaves Enter the 21st Century. Conference Proceedings (Cat. No.99TH8473)*, Singapore, 1999, pp. 962-965. doi: 10.1109/APMC.1999.833756

[18] W. M. Abdel Wahab, D. Busuioc and S. Safavi-Naeini, "Low cost planar waveguide technology-based dielectric resonator antenna (DRA) for millimeter-wave applications: analysis, design, and fabrication ,"*IEEE Transactions on Antennas and Propagation*, vol. 58, no. 8, Aug. 2010, pp. 2499-2507.doi: 10.1109/TAP.2010.2050443

[19] I. Afifi, M. M. M. Ali and A. Sebak, "Analysis and design of a wideband coaxial transition to metal and printed ridge gap waveguide," *IEEE Access*, vol. 6, 2018, pp. 70698-70706. doi: 10.1109/ACCESS.2018.2881732

[20] C. A. Balanis, Modern Antenna Handbook, John Wiley& Sons, Inc., 2008

[21] S. Hum and J. Perruisseau-Carrier, "Reconfigurable reflect arrays and array lenses for dynamic antenna beam control: a review," *IEEE Transactions on Antennas and Propagation*, vol. 62, no. 1, Jan. 2014, pp. 183-198. doi: 10.1109/TAP.2013.2287296

[22] L. Chang, Z. Zhang, Y. Li, S. Wang and Z. Feng, "60-GHz air substrate leaky-wave antenna based on MEMS micromachining technology," *IEEE Transactions on Components, Packaging and Manufacturing Technology*, vol. 6, no. 11, Nov. 2016, pp. 1656-1662. doi: 10.1109/TCPMT.2016.2616516

[23] S. Wang, P. Liu, L. Chang and Z. Zhang, "A 60GHz slot antenna based on MEMS bulk micromaching technology," *IEEE MTT-S International Microwave Workshop Series on Advanced Materials and Processes for RF and THz Applications (IMWS-AMP)*, Chengdu, 2016, pp. 1-3. doi: 10.1109/IMWS-AMP.2016.7588351

[24] Y. Luo, K. Kikuta, Z. Han, T. Takahashi, A. Hirose and H. Toshiyoshi, "An active metamaterial antenna with mems-modulated scanning radiation beams," *IEEE Electron Device Letters*, vol. 37, no. 7, July 2016, pp. 920-923. doi: 10.1109/LED.2016.2565559

[25] J. Kovitz and K. Allen, "Recent developments toward reconfigurable mmWave apertures and components using vanadium dioxide RF switches," *IEEE Wireless and Microwave Technology Conference (WAMICON)*, Sand Key, FL, 2018, pp. 1-4. doi: 10.1109/WAMICON.2018.8363904

[26] S. Shekhar, K. J. Vinoy and G. K. Ananthasuresh, "Low-voltage high-reliability MEMS switch for millimeter wave 5G applications," *Journal of Micromechanics and Microengineering*, vol. 28, no. 7, 2018. doi: 10.1088/1361-6439/aaba3e.

[27] P. Rynkiewicz *et al*., "Tunable dual-mode ring filter based on BiCMOS embedded MEMS in V-band," *IEEE Asia Pacific Microwave Conference (APMC)*, Kuala Lumpar, 2017, pp. 124-127. doi: 10.1109/APMC.2017.8251393

[28] D. Wang, F. An and S. W. Yoon, "Advanced EWLB (embedded wafer level ball grid array) solutions for mm-wave applications," *International Wafer Level Packaging Conference (IWLPC)*, San Jose, CA, 2018, pp. 1-6. doi: 10.23919/IWLPC.2018.8573266

[29] B. Adela, P. Zeijl, U. Johannsen and A. Smolders, "On-Chip antenna integration for millimeter-wave single-chip FMCW Radar, providing high efficiency and isolation," *IEEE Transactions on Antennas and Propagation*, vol. 64, no. 8, Aug. 2016, pp. 3281-3291. doi: 10.1109/TAP.2016.2570228

[30] M. Nezhad-Ahmadi, M. Fakharzadeh, B. Biglarbegian and S. Safavi-Naeini, "High-efficiency on-chip dielectric resonator antenna for mmwave transceivers," *IEEE Transactions on Antennas and Propagation*, vol. 58, no. 10, Oct. 2010, pp. 3388-3392. doi: 10.1109/TAP.2010.2055802

[31] A. Vorobyov, J. Farserotu and J. Decotignie, "3D printed antennas for mmwave sensing applications," *International Symposium on Medical Information and Communication Technology (ISMICT)*, Lisbon, 2017, pp. 23-26. doi: 10.1109/ISMICT.2017.7891759

[32] D. C. Lugo, R. A. Ramirez, J. Castro, J. Wang and T. M. Weller, "3D printed multilayer mmWave dielectric rod antenna with enhanced gain," *IEEE International Symposium on Antennas and Propagation & USNC/URSI National Radio Science Meeting*, San Diego, CA, 2017, pp. 1247-1248. doi: 10.1109/APUSNCURSINRSM.2017.8072666

[33] J. du Preez and S. Sinha, "Millimeter-wave Antennas: Configurations and Applications," *Signals and Communication Technology, Springer International Publishing Switzerland* 2016 doi: 10.1007/978-3-319-35068-4_2

[34] W. Stutzman, G. Thiele, Antenna Theory and Design, Third edition, John Wiley& Sons, Inc., 2013.

[35] B. Jeemon, K. Shambavi and Z. Alex, "A multi-fractal planar antenna for wireless applications," *2013 International Conference on Communication and Signal Processing*, Melmaruvathur, 2013, pp. 47-50. doi: 10.1109/iccsp.2013.6577012

[36] M. Nedil, L. Talbi and T. Denidni, "Design of broadband printed slot antennas for wireless millimeter-wave applications," *IEEE Topical Conference on Wireless Communication Technology*, Honolulu, HI, USA, 2003, pp. 23-24. doi: 10.1109/WCT.2003.1321426

[37] S. Sugawara, Y. Maita, K. Adachi, K. Mori and K. Mizuno, "Characteristics of a mm-wave tapered slot antenna with corrugated edges," *IEEE MTT-S International Microwave Symposium Digest (Cat. No.98CH36192)*, Baltimore, MD, USA, 1998, pp. 533-536 vol.2. doi: 10.1109/MWSYM.1998.705049

[38] P. Gibson, "The Vivaldi aerial," *European Microwave Conference*, Brighton, UK, 1979, pp. 101-105. doi: 10.1109/EUMA.1979.332681

[39] Z. Briqech, A. Sebak and T. Denidni, "High gain 60 GHz antipodal fermi tapered slot antenna with sine corrugation." *Microwave and Optical Tech Letters*, Vol 57, Jan. 2015, pp. 6-9.doi: 10.1002/mop.28772

[40] Y. Shiau, "Dielectric rod antennas for millimeter-wave integrated circuits (short papers)," *IEEE Transactions on Microwave Theory and Techniques*, vol. 24, no. 11, Nov. 1976, pp. 869-872. doi: 10.1109/TMTT.1976.1128980

[41] A. Petosa and S. Thirakoune, "Rectangular dielectric resonator antennas with enhanced gain," *IEEE Transactions on Antennas and Propagation*, vol. 59, no. 4, April 2011, pp. 1385-1389. doi: 10.1109/TAP.2011.2109690
[42] M. Al-Hasan, T. Denidni and A. Sebak, "Millimeter-wave EBG-based aperture-coupled dielectric resonator antenna," *IEEE Transactions on Antennas and Propagation*, vol. 61, no. 8, Aug. 2013, pp. 4354-4357. doi: 10.1109/TAP.2013.2262667
[43] K. Huang and D. Edwards, Millimetre Wave Antennas for Gigabit Wireless Communication, John Wiley and Sons Inc., 2008
[44] Q. Chu, X. Li and M. Ye, "High-gain printed log-periodic dipole array antenna with parasitic cell for 5G communication," *IEEE Transactions on Antennas and Propagation*, vol. 65, no. 12, Dec. 2017, pp. 6338-6344. doi: 10.1109/TAP.2017.2723916
[45] J. Huang and A. C. Densmore, "Microstrip Yagi array antenna for mobile satellite vehicle application," *IEEE Transactions on Antennas and Propagation*, vol. 39, no. 7, July 1991, pp. 1024-1030. doi: 10.1109/8.86924
[46] R. Alhalabi and G. Rebeiz, "High-gain Yagi-Uda antennas for millimeter-wave switched-beam systems," *IEEE Transactions on Antennas and Propagation*, vol. 57, no. 11, Nov. 2009, pp. 3672-3676. doi: 10.1109/TAP.2009.2026666
[47] B. Park, M. Jeong and S. Park, "A Miniaturized microstrip-to-coplanar-strip transition loaded with artificial transmission lines and 2.4-ghz antenna application," *IEEE Antennas and Wireless Propagation Letters*, vol. 13, 2014, pp. 1486-1489. doi: 10.1109/LAWP.2014.2341552
[48] A. Hosseini and F. De Flaviis, "A CPW-fed single-layer printed quasi-Yagia antenna for 60 GHz wireless communication systems," *IEEE Antennas and Propagation Society International Symposium (APSURSI)*, Memphis, TN, 2014, pp. 103-104. doi: 10.1109/APS.2014.6904383
[49] H. Kan, R. Waterhouse, A. Abbosh and M. Bialkowski, "Simple broadband planar cpw-fed quasi-Yagi antenna," *IEEE Antennas and Wireless Propagation Letters*, vol. 6, 2007, pp. 18-20. doi: 10.1109/LAWP.2006.890751
[50] P. Wang and C. Cui, "Small-size cpw-fed quasi-Yagi antenna with round-ended bow-tie cpw-to-slotline transition," *IEEE International Symposium on Radio-Frequency Integration Technology (RFIT)*, Taipei, 2016, pp. 1-3. doi: 10.1109/RFIT.2016.7578136
[51] J. Wu, Z. Zhao, Z. Nie and Q. Liu, "Bandwidth enhancement of a planar printed quasi-Yagi antenna with size reduction," *IEEE Transactions on Antennas and Propagation*, vol. 62, no. 1, Jan. 2014, pp. 463-467. doi: 10.1109/TAP.2013.2287286
[52] S. Ta, J. Han, H. Choo and I. Park, "A wideband double dipole quasi-Yagi antenna using a microstrip-slotline transition feed," *IEEE International Workshop on Antenna Technology (iWAT)*, Tucson, AZ, 2012, pp. 84-87. doi: 10.1109/IWAT.2012.6178404
[53] H. Lu, L. Si and Y. Liu, "Compact planar microstrip-fed quasi-Yagi antenna," *Electronics Letters*, vol. 48, no. 3, February 2012, pp. 140-141. doi: 10.1049/el.2011.3458
[54] Y. Lo, S. Wu, N. Liu and J. Tarng, "A compact planar 60-GHz cpw-fed pattern reconfigurable quasi-yagi antenna," *European Conference on Antennas and Propagation (EuCAP 2018)*, London, 2018, pp. 1-3. doi: 10.1049/cp.2018.0895
[55] J. Tao, Q. Feng and T. Liu, "Dual-wideband magnetoelectric dipole antenna with director loaded," *IEEE Antennas and Wireless Propagation Letters*, vol. 17, no. 10, Oct. 2018, pp. 1885-1889,. doi: 10.1109/LAWP.2018.2869034
[56] H. Wang, S.-F. Liu, W.-T. Li, and X.-W. Shi, "Design of a wideband planar microstrip-fed quasi-yagi antenna," *Progress In Electromagnetics Research Letters*, vol. 46, 2014, pp. 19-24. doi:10.2528/PIERL14031702.
[57] M. Tang, T. Shi and R. Ziolkowski, "Flexible efficient quasi-Yagi printed uniplanar antenna," *IEEE Transactions on Antennas and Propagation*, vol. 63, no. 12, Dec. 2015, pp. 5343-5350. doi: 10.1109/TAP.2015.2486807
[58] D. Liu, W. Hong, T. Rappaport, C. Luxey and W. Hong, "What will 5G antennas and propagation be?," *IEEE Transactions on Antennas and Propagation*, vol. 65, no. 12, Dec. 2017, pp. 6205-6212. doi: 10.1109/TAP.2017.2774707
[59] L. Lu, K. Ma, F. Meng and K. Yeo, "Design of a 60GHz quasi-Yagi antenna with novel ladder-like directors for gain and bandwidth enhancements," *IEEE Antennas and Wireless Propagation Letters*, vol. 15 , 2016, pp. 682-685. doi: 10.1109/LAWP.2015.2469139.
[60] L. Xue, V. Fusco, " Patch fed planar dielectric slab extended hemi-elliptical lens antenna," *IEEE Transactions on Antennas and Propagation,* vol. 56, no. 3, March. 2008, pp. 661-666. doi:10.1109/TAP.2008.916974.
[61] L. Xue, V. Fusco, " Patch-fed planar dielectric slab waveguide Luneburg lens," *IET Microwaves, Antennas & Propagation*, vol. 2, no. 2, March. 2008, pp. 109-114. doi: 10.1049/iet-map:20070146.

[62] P. Yadav, S. Mukherjee and A. Biswas, “Design of planar substrate integrated waveguide (SIW) phase shifter using air holes,” *IEEE Applied Electromagnetics Conference (AEMC)*, Guwahati, 2015, pp. 1-2. doi: 10.1109/AEMC.2015.7509117

[63] Y. He, Z. Gao, D. Jia, W. Zhang, B. Du and Z. N. Chen, “Dielectric metamaterial-based impedance-matched elements for broadband reflect array,” *IEEE Transactions on Antennas and Propagation*, vol. 65, no. 12, Dec. 2017, pp. 7019-7028. doi: 10.1109/TAP.2017.2763176

[64] Y. Cai, Y. Zhang, Z. Qian, W. Cao and L. Wang, “Design of compact air-vias-perforated siw horn antenna with partially detached broad walls,” *IEEE Transactions on Antennas and Propagation*, vol. 64, no. 6, June 2016, pp. 2100-2107. doi: 10.1109/TAP.2016.2542841

[65] Y. Li and K. Luk, “Wideband perforated dense dielectric patch antenna array for millimeter-wave applications,” *IEEE Transactions on Antennas and Propagation*, vol. 63, no. 8, Aug. 2015, pp. 3780-3786. doi: 10.1109/TAP.2015.2441118

[66] M. Hassanien, R. Hahnel and D. Plettemeier, “A novel electronically wideband steering system using Rotman lens for 5G applications at 28 GHz,” *European Conference on Antennas and Propagation (EuCAP 2018)*, London, 2018, pp. 1-5. doi: 10.1049/cp.2018.1001

[67] T. K. Vo Dai, T. Nguyen and O. Kilic, “Compact multi-layer microstrip Rotman lens design using coupling slots to support millimetre wave devices,” *IET Microwaves, Antennas & Propagation*, vol. 12, no. 8, 4 7 2018, pp. 1260-1265. doi: 10.1049/iet-map.2017.0817

[68] J. Pourahmadazar and T. Denidni, “X-band substarte integrated rotman Lens with ±24° scanning capability,” *IEEE International Symposium on Antennas and Propagation & USNC/URSI National Radio Science Meeting*, Vancouver, BC, 2015, pp. 232-233. doi: 10.1109/APS.2015.7304502

[69] S. Hosseini, H. Firouzeh and M. Maddahali. “Design of Rotman lens antenna at Ku-band based on substrate integrated technology,” *Journal of Communication Engineering*, vol. 3, no. 1, 2014, pp. 33-44.

[70] K. Tekkouk, M. Ettorre, L. Coq and R. Sauleau, “Multibeam siw slotted waveguide antenna system fed by a compact dual-layer Rotman lens,” *IEEE Transactions on Antennas and Propagation*, vol. 64, no.2, Feb. 2016, pp. 504-514. doi: 10.1109/TAP.2015.2499752

[71] K. Tekkouk, M. Ettorre and R. Sauleau, “SIW Rotman lens antenna with ridged delay lines and reduced footprint,” *IEEE Transactions on Microwave Theory and Techniques*, vol. 66, no. 6, June 2018, pp. 3136-3144. doi: 10.1109/TMTT.2018.2825374

[72] L. Suárez, D. Méndez, M. Baquero-Escudero, B. Bernardo-Clemente and S. Giner, “Transitions between gap waveguides for use in a phased array antenna fed by a Rotman lens,” *European Conference on Antennas and Propagation (EuCAP 2014)*, The Hague, 2014, pp. 774-777. doi: 10.1109/EuCAP.2014.6901875

[73] F. Suárez, D. Méndez and M. Baquero-Escudero, “Rotman lens with ridge gap waveguide technology for millimeter wave applications,” *European Conference on Antennas and Propagation (EuCAP)*, Gothenburg, 2013, pp. 4006-4009.

[74] J. Pourahmadazar, M. Farahani and T. Denidni, “Printed ridge gap waveguide Rotman Lens for millimetre-wave applications,” *International Symposium on Antenna Technology and Applied Electromagnetics (ANTEM)*, Waterloo, ON, 2018, pp. 1-2. doi: 10.1109/ANTEM.2018.8572972

[75] A. Rahimian, A. Alomainy and Y. Alfadhl, “A flexible printed millimetre-wave beamforming network for WiGig and 5G wireless subsystems,” *Loughborough Antennas & Propagation Conference (LAPC)*, Loughborough, 2016, pp. 1-5. doi: 10.1109/LAPC.2016.7807565

[76] Available [Online].: https://www.itu.int/en/ITU-D/Documents/ITU_5G_REPORT-2018.pdf, last access on Nov. 18, 2019.

[77] R. C. Hansen, “Design trades for Rotman lenses,” *IEEE Transactions on Antennas and Propagation*, vol. 39, no. 4, April 1991, pp. 464-472. doi: 10.1109/8.81458

[78] E. Rajo-Iglesias and P. Kildal, “Cut-off bandwidth of metamaterial-based parallel plate gap waveguide with one textured metal pin surface,” *European Conference on Antennas and Propagation*, Berlin, 2009, pp. 33-36.

[79] D. M. Pozar, “Microwave Engineering”. John Wiley and Sons Inc. 4th Edition, 2011

[80] M. S. Smith, “Design considerations for Ruze and Rotman lenses,” *Radio and Electronic Engineer*, vol. 52, no. 4, April 1982, pp. 181-187. doi: 10.1049/ree.1982.0027

[81] W. Rotman and R.F. Turner, “Wide angle microwave lens for line source applications,” *IEEE Transaction on Antennas and Propagation*, vol. 11, no. 6, Nov. 1963, pp. 623-632. doi: 10.1109/TAP.1963.1138114

[82] P. Simon, “Analysis and synthesis of Rotman lenses,” in *Proceedings of the 22nd AIAA International Communications Satellite Systems Conference & Exhibit*, Monterey, Calif, USA, May 2004. doi: 10.2514/6.2004-3196.

[83] E. O. Rausch and A. F. Peterson, "Rotman lens design issues," *IEEE Antennas and Propagation Society International Symposium*, Washington, DC, 2005, pp. 35-38 vol. 2B. doi: 10.1109/APS.2005.1551928
[84] C. W. Penney, "Rotman lens design and simulation in software [Application Notes]," *IEEE Microwave Magazine*, vol. 9, no. 6, December 2008, pp. 138-149. doi: 10.1109/MMM.2008.929774
[85] E. Sbarra, L. Marcaccioli, R. V. Gatti and R. Sorrentino, "A novel Rotman lens in siw technology," *European Radar Conference*, Munich, 2007, pp. 236-239. doi: 10.1109/EURAD.2007.4404980
[86] A. Rahimian, "Design and Performance of a KU-Band Rotman lens beamforming network for satellite Systems," *Progress In Electromagnetics Research B*, vol. 28, 2013, pp. 41-55.
[87] P. Kildal, "Definition of artificially soft and hard surfaces for electromagnetic waves," *Electronics Letters*, vol. 24, no. 3, 4 Feb. 1988, pp. 168-170.
[88] P. Kildal, A. Kishk, "EM modeling of surfaces with STOP or GO Characteristics - artificial magnetic conductors and soft and hard surfaces". *Applied Computational Electromagnetics Society Journal*. vol. 18, 2003, pp. 32-40.
[89] P. Kildal, "Artificially soft and hard surfaces in electromagnetics," *IEEE Transactions on Antennas and Propagation*, vol. 38, no. 10, Oct. 1990, pp. 1537-1544. doi: 10.1109/8.59765
[90] C. A. Balanis, "Advance Engineering Electromagnetics," 2nd edition, John Wiley& Sons, Inc., 2012
[91] C. A. Balanis, "Antenna Theory Analysis and Design," Third edition, John Wiley& Sons, Inc., 2005
[92] R. Elliott, "On the theory of corrugated plane surfaces," *Transactions of the IRE Professional Group on Antennas and Propagation*, vol. 2, no.2, April 1954, pp.71-81. doi: 10.1109/T-AP.1954.27975
[93] C. Palmer, "Diffraction Gratings Handbook," Seventh edition, Newport Corporation, 2014.
[94] Erwin G. Loewen, Evgeny Popov, "Diffraction Gratings and Applications," Seventh edition, Marcel Dekker, Inc, 1997.
[95] E. Popov, "Gratings: Theory and Numeric Applications," First Edition, Presses universitaires de Provence (PUP), 2012.
[96] T. Inoue, "5G standards progress and challenges," *2017 IEEE Radio and Wireless Symposium (RWS)*, Phoenix, AZ, 2017, pp. 1-4. doi: 10.1109/RWS.2017.8048566.
[97] T. Katagi, S. Mano and S. Sato, "An improved design method of Rotman lens antennas," in *IEEE Transactions on Antennas and Propagation*, vol. 32, no. 5, May 1984, pp. 524-527. doi: 10.1109/TAP.1984.1143353
[98] M. Yunita, G. Hadi, Y. Isvara, and A. Budiyarto, "Analysis of Vivaldi rectangular bow-tie and quasi-Yagi antenna performance for S-band FMCW-SAR on UAV platform", *J. Unmanned Syst. Technol.*, vol. 5, no. 3, 2018, pp. 76-79.doi:10.21535/just.v5i3.976.
[99] A. Darvazehban, O. Manoochehri, M. A. Salari, P. Dehkhoda, and A. Tavakoli, "Ultra-wideband scanning antenna array with Rotmanl lens," *IEEE Transactions on Microwave Theory and Techniques*, vol. 65, no. 9, Sept. 2017, pp. 3435-3442. doi: 10.1109/TMTT.2017.2666810
[100] M. Sorkherizi and A. Kishk, "Self-packaged, low-loss, planar bandpass filters for millimeter-wave application based on printed gap waveguide Technology," in *IEEE Transactions on Components, Packaging and Manufacturing Technology*, vol. 7, no. 9, Sept. 2017, pp. 1419-1431. doi: 10.1109/TCPMT.2017.2702753
[101] M. Farahani, T. Denidni and M. Nedi, "Design of a Low Output-Phase Error Ridge-Gap Coupler for Antenna Arrays Applications," *2018 IEEE International Symposium on Antennas and Propagation & USNC/URSI National Radio Science Meeting*, Boston, MA, 2018, pp. 1099-1100. doi: 10.1109/APUSNCURSINRSM.2018.8608322
[102] S. I. Shams and A. A. Kishk, "Design of 3-dB hybrid coupler based on rgw technology," in *IEEE Transactions on Microwave Theory and Techniques*, vol. 65, no. 10, Oct. 2017, pp. 3849-3855. doi: 10.1109/TMTT.2017.2690298 doi: 10.1109/APUSNCURSINRSM.2018.8608322
[103] M. M. M. Ali and A. Sebak, "2-D scanning magnetoelectric dipole antenna array fed by RGW Butler Matrix," in *IEEE Transactions on Antennas and Propagation*, vol. 66, no. 11, pp. 6313-6321, Nov. 2018. doi: 10.1109/TAP.2018.2869228
[104] M. M. M. Ali and A. Sebak, "Compact printed ridge gap waveguide crossover for future 5g wireless communication system," in *IEEE Microwave and Wireless Components Letters*, vol. 28, no. 7, July 2018, pp. 549-551. doi: 10.1109/LMWC.2018.2835149
[105] E. Pucci, A. U. Zaman, E. Rajo-Iglesias, P. Kildal and A. Kishk, "Losses in ridge gap waveguide compared with rectangular waveguides and microstrip transmission lines," *Proceedings of the Fourth European Conference on Antennas and Propagation*, Barcelona, 2010, pp. 1-4.
[106] P. Kildal, A. Zaman, E. Rajo-Iglesias, E. Alfonso and A. Valero-Nogueira, "Design and experimental verification of ridge gap waveguide in bed of nails for parallel-plate mode suppression," in IET Microwaves, Antennas & Propagation, vol. 5, no. 3, pp. 262-270, 21 Feb. 2011. doi: 10.1049/iet-map.2010.0089

[107] Protolabs, [Online]. Available: https://www.protolabs.com/materials/comparison-guide/, last access on Nov. 17, 2019.

List of Publications

Journals

[J1] E. Mujammami and A. Sebak, "Wideband high gain printed quasi-yagi diffraction gratings-based antenna for 5G applications," *in IEEE Access*, vol. 7, 2019, pp. 18089-18100. doi: 10.1109/ACCESS.2019.2897092

[J2] E. Mujammami, I. Afifi and A. Sebak, "Optimum wideband high gain analog beamforming network for 5G applications," in *IEEE Access*, vol. 7, 2019, pp. 52226-52237. doi: 10.1109/ACCESS.2019.2912119

[J3] E. Mujammami and A. Sebak, " Wideband high gain low-distortion ridge gap waveguide rotman lens-based analog beamforming network for 5g applications," submitted *to IEEE Transactions on Antennas and Propagation*, September 2019.

Conferences

[C1] E. Mujammami and A. Sebak, "Design of a 30-GHz high gain quasi-Yagi antenna," *2017 XXXIInd General Assembly and Scientific Symposium of the International Union of Radio Science (URSI GASS)*, Montreal, QC, Canada, 2017, pp. 1-3. doi: 10.23919/URSIGASS.2017.8105181

[C2] E. Mujammami and A. Sebak, "Signal and system approach for designing planar wideband high gain endfire millimeter wave antennas," 2019 *13th European Conference on Antennas and Propagation (EuCAP)*, Krakow, Poland, 2019, pp. 1-5.

[C3] E. Mujammami and A. Sebak, "A High gain broadband quasi-yagi dielectric lens antenna for 5g and millimeter wave applications," *2019 IEEE International Symposium on Antennas and Propagation and USNC-URSI Radio Science Meeting*, Atlanta, GA, USA, 2019, pp. 1911-1912. doi: 10.1109/APUSNCURSINRSM.2019.8888866

[C4] E. Mujammami and A. Sebak, "Analog beamforming system using rotman lens for 5G applications at 28 GHz," *2019 IEEE International Symposium on Antennas and Propagation and USNC-URSI Radio Science Meeting*, Atlanta, GA, USA, 2019, pp. 153-154. doi: 10.1109/APUSNCURSINRSM.2019.8888493